INVESTIGATION OF THE EFFECT OF TISSUE WATER DYNAMICS ON COMPARTMENTAL MRI MEASUREMENTS USING CONTRAST ENHANCED RELAXOMETRY AND SPECT

By

Jack Thomas Skinner

Dissertation

Submitted to the Faculty of the

Graduate School of Vanderbilt University

in partial fulfillment of the requirements

for the degree of

DOCTOR OF PHILOSOPHY

in

Biomedical Engineering

May, 2012

Nashville, TN

Approved:

Professor Mark D. Does

Professor Thomas E. Yankeelov

Professor Bruce M. Damon

Professor Todd E. Peterson

Professor John C. Gore

This work is dedicated to my family:

Patrick, Patricia, Steven, Kathryn, Joe, and Stephanie

ACKNOWLEDGEMENTS

I would like to acknowledge several individuals for their assistance and support over the years, as it is without them that this work would not be possible. First I would like to thank my advisor, Mark Does, who has provided me with a breadth of knowledge in my time at Vanderbilt and has not only stressed the importance of hard work but also of holding oneself to a higher standard. I would also like to thank my committee members. First, Bruce Damon, who provided helpful critiques during the completion of my Master's thesis and informative conversation about muscle-related topics throughout my PhD research. Thanks to Tom Yankeelov, for instructing me in the ways of DCE-MRI and for maintaining my interest in imaging research during the 'Math Methods in Imaging' course in my first semester of graduate school. I thank Todd Peterson for showing me that there is more to imaging than just MRI, and that an interest in music and scientific research can go hand in hand. Thanks also to John Gore, who has provided a first rate facility and scientific community within which I was able to develop as an independent researcher.

In addition, there are many people, past and present, at the Vanderbilt University Institute of Imaging Science (VUIIS) that I would like to acknowledge. First, to Jeff Luci and Richard Baheza, for training me on the animal magnets and teaching me how to properly run an MRI experiment. Thanks to Daniel Colvin for technical assistance with experimental set-up, trouble-shooting the Varian console, and for accommodating me when I needed a few extra minutes to complete a scan. Thanks to Zoe Yue for performing all of my animal surgeries and for accommodating my sometimes complicated imaging schedule. Thanks to Clare Osborne and Noor Tantawy for help with SPECT imaging, and to Don Nolting, Ron Baldwin, Jeff Clanton, and Marni Gardner for help with radiotracer labeling. I would also

like to thank Mary Loveless and Jennifer Whisenant for help with DCE-MRI protocol development and analysis, as well as informative discussions. I would like to thank my lab group, past and present, specifically Adam Horch and Richard Dortch, who helped me with a variety of MR related issues including experimental and data analysis techniques. Thanks to Megan Johnston, a summer student, who helped in the development and application of the T_2-HASTE protocol. I would also like to thank my officemates in AA1112, for both moral and technical support. Our many conversations helped make each day of graduate school a bit more enjoyable. Thanks also to Nancy Hagans for her help with scheduling committee meetings and for all of her work around the VUIIS, particularly with the annual research retreat. In addition, I would like to thank the faculty and staff in the department of biomedical engineering.

I would also like to thank my family and friends. These are the people who provided support and helped keep me going, though they did not exactly understand what I did on a daily basis. First to my parents, Patrick and Patricia Skinner, who I am ever grateful for all they have taught me throughout the years. Thanks to my siblings, Kathryn and Joe, for helping put everything into perspective. Thanks to my grandparents, relatives, and wife's family for all of the encouragement throughout this process. Finally, to my wife Stephanie, your love, selflessness, and constant support over the past 6 years has made all the difference. Your encouraging words and reminder to "Just suck it up and get it done!" during the highs and lows of this process resonate with me on a daily basis. To all those I might have missed, I appreciate all you have done for me.

TABLE OF CONTENTS

LIST OF TABLES

LIST OF FIGURES

CHAPTER 1

INTRODUCTION

Magnetic resonance imaging (MRI) provides an excellent means of visualizing soft tissue for anatomical characterization as well as pathology and injury for diagnostic applications. The source of contrast between soft tissues is a result of variation in image intensity caused by a change in nuclear magnetic resonance (NMR) signal characteristics. Though changes in image intensity are useful in a qualitative sense, they do not reveal much about the micro-anatomical structure of a given tissue. To take full advantage of the sub-voxel information that can be probed from the tissue, quantitative measures are needed.

Tissue can be regarded as being primarily comprised of water. Water protons can exist in various states including that which resides in cells, interstitial tissue space, and vasculature. In these so-called 'compartments', water molecules traverse micro-anatomical structures while being restricted by cellular membranes. In addition to compartmentalized water, the cellular environment consists of proteins and other macromolecules that have associated water protons in the form of hydration water. The interaction of each water molecule, or water proton, with neighboring protons and the surrounding micro-environment, results in a detectable signal that is sensitive to the amount and distribution of water (^{1}H) present in the tissue.

In the simplest view, tissue can be described as having two compartments, intracellular and extracellular (interstitial) space, within which water resides. The distribution of water due to tissue compartmentalization and water proton interaction in tissue affects the NMR signal by altering the rate of water proton relaxation. Specific techniques for measuring

tissue relaxation in MRI have been previously developed. In a clinical setting many of these methods are only concerned with measuring gross changes in longitudinal (T_1) or transverse (T_2) relaxation with pathology (1-4). In these studies, the use of compartmental models is disregarded with the assumption of monoexponential relaxation. Without compartmental modeling, however, important information about tissue microstructure can be lost. Data analysis with a single pool tissue model is more often used in human imaging, where more involved relaxation-based measurements (often required for compartmental modeling) can be lengthy and unsuitable for clinical imaging. Despite these studies, a variety of pre-clinical MR measurements have incorporated two-pool or multi-pool models for tissue characterization.

Assumption of a single tissue compartment does not provide the entire picture, particularly in tissues that are heterogeneous (e.g. tumor) or those known to exhibit multi-exponential relaxation (e.g. skeletal muscle). One application of multi-compartment modeling in MRI is with multiple spin-echo (MSE) imaging for estimation of T_2. MSE experiments have been made in a variety of tissues including white matter, nerve, tumor and muscle (5-8). Though these studies provide measures of relative compartment size and relaxation rates, assumptions are often made regarding tissue water dynamics. Tissue compartmentalization and cell membrane permeability have an effect on the rate of water diffusion and inter-compartmental water exchange observed in tissue. Because the observable MR signal is influenced by the movement and number of water molecules present, one must consider how this affects resulting tissue parameter estimates when modeling MR signal intensity. This concept is often discussed in quantitative MR studies of skeletal muscle.

The observation and interpretation of non-monoexponential relaxation in muscle tissue has been studied extensively over the past several decades (9-13). The number of tissue compartments, their relative sizes, and physiological interpretation is up for discussion, though many studies have adopted a two-pool model of muscle tissue. In addition, a part of this discussion is the role of inter-compartmental water exchange and its effect on the observed tissue model parameters. The resolution of multiple signal components, particularly in injured muscle (14-16), indicate that the tissue is likely not in a state of fast water exchange, however, it is unknown how close the observed MR model parameter estimates are to their intrinsic values.

The previous scenario presents a need for validation of currently used MSE techniques and compartmental models in skeletal muscle. It also creates an opportunity for developing novel methods that may provide new information leading to improved modeling of muscle tissue in MRI. Assessing the accuracy of MR model parameter estimates may be important in injured and diseased muscle as changes in tissue micro-structure, including cell membrane permeability, may have significant effects on the observed parameters. This knowledge would be advantageous in clinical disease models such as Duchenne muscular dystrophy, characterized by progressive muscle weakness due to cell membrane instability followed by edema and fatty infiltrations (1). The use of MSE imaging with a more reliable compartmental MR model of muscle injury might also help interpret changes in T_2 with edema, as observed in studies of inflammatory myopathies (2).

When implementing two-pool tissue models, knowledge of water exchange can help create a more comprehensive physiological model from which intrinsic MR compartmental parameters may be estimated. Techniques for estimating water exchange rates are often

complex and require time consuming measurements that restrict these methods to ex vivo tissue (17-19). In recent years, water exchange rates have been estimated by introducing exogenous substances, such as contrast agents (CA), into tissue followed by the application of pharmacokinetic models to dynamically acquired data. The contrast enhanced experiment as well as subsequent pharmacokinetic modeling, however, can have limitations and inherent difficulties.

Though endogenous NMR tissue properties such as relaxation and exchange contribute to changes in MR signal intensity, CAs are also used in MRI to elicit changes in these NMR properties. The resulting change in the MR signal intensity over time is due to the effect of the CA on the water molecules themselves and can be quantified as an indirect measure of contrast distribution. One particular technique, dynamic contrast-enhanced MRI (DCE-MRI), has been used frequently over the past decade to extract rates of contrast agent extravasation as well as compartmental sizes (i.e. extracellular volume (v_e)) via pharmacokinetic modeling of cancerous tissues.

DCE-MRI has been applied in a wide variety of tissues and tumor types. Though the type of data acquired in these studies is similar, the methods for analyzing this data are numerous (20). A common pharmacokinetic model, the Tofts model, is often used in DCE-MRI to described CA distribution in two compartments representing the vasculature and the extracellular-extravascular space (21). This model can be extended to include contributions from plasma space in well vascularized tumors (22). Models have also been implemented that include transcytolemmal water exchange (23), though this continues to be a topic of discussion. In recent years, the possibility of CA diffusion in solid tumors has also been incorporated into conventional pharmacokinetic modeling (24). The selection of a vascular

input function (VIF) (e.g. individual, population, model) or reference region (RR) to drive the pharmacokinetic modeling can also dictate the specific model used, though each of these methods have their own advantages and disadvantages. The use of different models in analysis of DCE-MRI data may result in varying estimates of common pharmacokinetic parameters. As DCE-MRI is used more frequently in human imaging, validation of common DCE-MRI analysis techniques would provide insight into the accuracy of the models themselves as well as the degree to which tissue water dynamics affect the estimation of the model parameters.

In addition to compartmental T_2 measurements and DCE-MRI, other imaging techniques can provide quantitative measures of tissue micro-structure. One of these methods, diffusion weighted (DW-MRI) imaging, uses pulsed gradient spin-echo measurements to monitor the random restricted movement of water molecules in tissue. This data can then be used to compute an estimate of the rate of water diffusion or apparent diffusion coefficient (ADC) in tissue. This measure is sensitive to the tissue micro-environment as well as the pulse sequence design itself. Though diffusion imaging is a useful quantitative technique, DW-MRI alone does not normally lend itself to compartmental modeling as previously described. DW-MRI has been used most often in clinical imaging with application in stroke to help identify ischemic tissue regions (25). In cancer imaging DW-MRI can provide an indicator of tissue cellularity in tumors (26), though the technique itself does not provide a direct measure of the relative tissue volume fractions.

Many quantitative MR techniques apply tissue models to relate MR parameters to underlying physiology. This is not without difficulty, however, due to constructs of the models themselves. There is still a question of how accurate these models are and how well

they actually describe the tissue of interest. As discussed, water exchange may not always be considered in an MR experiment or aspects of CA kinetics in a given tissue may not always be accounted for. Though MRI provides robust methods for making quantitative measurements of sub-voxel tissue properties, alternate imaging strategies might provide additional information on the accuracy and reliability of these measures. For this reason, validation and re-evaluation of commonly implemented relaxation-based MR measurements would be advantageous.

It is difficult to define a true "gold standard" for which to compare compartmental measurements from MRI, however, radiotracer methods offer the advantage that the signal observed is insensitive to tissue water dynamics. This is a result of the direct nature with which the distribution of the injected radiotracer is detected. This is in contrast to the indirect measurement of CA distribution in MRI. One radionuclide imaging method, single photon emission computed tomography (SPECT), implements radiotracers that can be made compartment specific. Furthermore, multiple isotopes can be detected and measured simultaneously due to the inherent energy discrimination of emitted photons available with SPECT. Though *in vivo* quantitative measures of specific tissue compartments have not been documented with radiotracer imaging, SPECT does exhibit promise in providing tissue parameters, such as extracellular volume fraction, that are un-biased by water exchange.

The validation of the previously described MR relaxation measurements and corresponding tissue models may be one step in incorporating these techniques into clinical practice. Another possibility is to design MRI pulse sequences that accelerate the acquisition of quantitative data. Though DCE-MRI has been used in human imaging and has progressed toward clinical use, techniques such as MSE imaging are infrequently implemented in

humans. To address this issue, single-shot imaging techniques may be used to acquire data in a fraction of the time of pre-clinical MSE measurements. As with previous relaxation-based methods, accelerated MSE methods would benefit from the ability to characterize multi-exponential signal decay for the purpose of compartmental tissue modeling.

The studies presented in this work focus on the evaluation and validation of compartmental NMR tissue properties as extracted from physiological modeling of T_1 and T_2 relaxation measurements with the use of a paramagnetic contrast agent. A quantitative SPECT technique is developed to provide an *in vivo* measure of the extracellular-extravascular tissue volume for comparison with the MR measurements in animal models of muscle inflammation and glioma. In an attempt to address the clinical translation of these MR based measurements, a novel method aimed at scan time reduction in multi-slice multi-echo relaxation measurements is also presented.

CHAPTER 2

BACKGROUND

1. Relaxation in Magnetic Resonance Imaging

MRI is largely based on the observation of hydrogen proton spins, found abundantly in water-rich tissues, in the presence of an external magnetic field, B_0. ^{1}H spins will tend to align with this field, creating a net magnetization, $\vec{M}$, that precesses around B_0, according to the Larmor equation (27)

$$\omega_0 = \gamma \cdot B_0 \qquad [2.1]$$

where γ (26,751 rads/(s·G) for H^1) is referred to as the gyromagnetic ratio. Perturbation of this magnetization from equilibrium by tuned radiofrequency pulses results in a nuclear magnetic resonance (NMR) signal that can be detected and encoded by spatially varying magnetic field gradients and can ultimately be transformed to create an image. An important concept in MRI is the rate at which the detected magnetization changes after the application of an RF pulse due to spin interactions with other spins and the surrounding micro-environment. The rate of magnetization decay and/or return to equilibrium due to these interactions is referred to as the 'relaxation' properties of the observed sample.

1.1 Transverse Relaxation (T_2)

Following an RF excitation pulse, magnetization that is oriented in the transverse plane will experience both an applied field and fluctuations in a local magnetic field.

Variations in the local magnetic field as well as spin-spin interactions lead to different local precessional frequencies. This variation results in transverse magnetization decay owing to a loss of phase coherence. After excitation, spins are said to be 'dephasing', which leads to a reduction in the net transverse magnetization vector. The process of magnetization decay in the transverse plane due to spin-spin interactions is known as transverse relaxation, and is described by the time constant T_2. According to the Bloch equations (28), the transverse component of the nuclear magnetization ($M_\perp$) can be described by

$$\frac{dM_\perp}{dt} = -\frac{M_\perp}{T_2} \quad . \qquad [2.2]$$

The solution to Eq. [2.2], after a 90° excitation pulse, is

$$M_\perp(t) = M_0 \cdot e^{-t/T_2} \qquad [2.3]$$

where M_0 is the transverse magnetization (at t=0) immediately following the excitation pulse and t is the time for signal formation relative to the excitation.

Transverse relaxation can be measured in several ways, though most techniques employ some form of the basic spin-echo experiment (29). In a spin-echo experiment, longitudinal magnetization is first rotated down into the transverse plane by a 90° RF pulse. The magnetization that has been placed in the transverse plane begins to acquire phase during a period, τ. A 180° refocusing pulse is then applied, which reverses the phase acquired during τ. If the field gradients experienced by the spins are static, then the phase distribution accumulated before the 180° pulse will be refocused during a second time period, τ, and a so-

called spin echo will form (at t=2τ). The period of time from the middle of the excitation pulse to the peak of the echo is also known as the echo time, TE. The basic spin-echo pulse sequence can be seen in Fig. 2.1a.

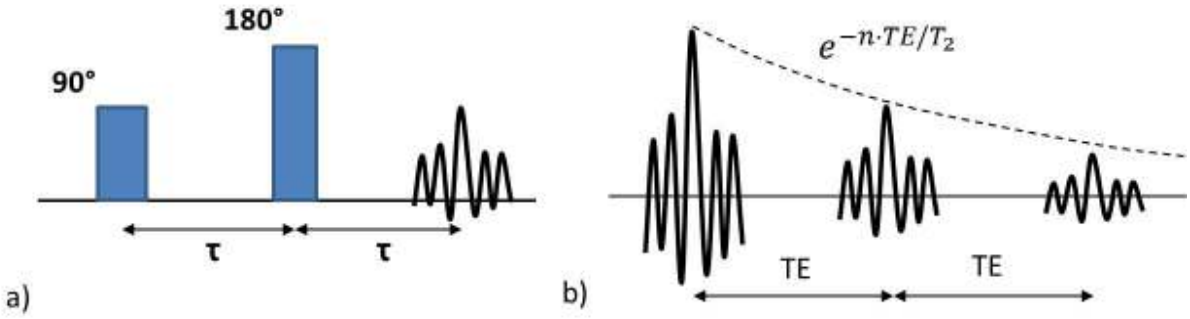

Fig. 2.1. a) Basic spin-echo pulse sequence. b) Example echo train in a multiple spin-echo experiment with corresponding T_2 decay curve.

T_2 Estimation

To quantitatively measure T_2, multiple spin-echo experiments can be performed (30,31). In a multiple spin-echo (MSE) experiment, the spin-echo sequence in Fig. 2.1a is modified by adding a series of 180° refocusing pulses to create a train of echoes separated by a time TE. The signal intensity at each echo is used to form a decay curve that can be fitted with an exponential function to extract the T_2 value of the tissue. This is represented in Fig. 2.1b. There exist challenges, however, in making quantitative measurements of T_2 in both single-slice and multiple-slice scenarios. Impeding the accuracy of these measurements are system imperfections, including inhomogeneities in the static magnetic field and imperfections in the RF refocusing pulses.

In MSE imaging, static field inhomogeneities (ΔB) serve to modify the effect of the applied RF pulses (32). In the presence of ΔB the flip angle (α) of a RF refocusing pulse will deviate from the ideal 180°. An effective field, B_{eff}, is created that includes the effects of the applied RF field (B_1) and ΔB. In this way,

$$\alpha = \gamma \cdot B_{eff} \cdot t_p \qquad [2.4]$$

where t_p is the RF pulse duration. With successive refocusing pulses that display flip angles different from 180°, the accumulated phase of the spins will not be completely refocused and therefore a reduced $M_\perp$ will be observed as well as the addition of an M_z component. The propagation of this error across the echo train will ultimately lead to incorrect estimation of T_2. One approach to reduce the effects from these unwanted signal components is to dephase the unwanted signal with a pair of spoiler gradients surrounding each RF refocusing pulse (33,34). The use of spoiler gradient pairs will help suppress ghost artifacts resulting from imperfect refocusing.

In addition to B_0, inhomogeneities associated with the applied B_1 are also of concern when making T_2 measurements. If the applied B_1 does not create an ideal 180° rotation, then phase accumulated due to ΔB is not refocused and the echo amplitudes are modified (35). As was previously described, the net magnetization after an imperfect 180° pulse consists of several components: a longitudinal component, a transverse component that refocuses, and a transverse component that continues to accumulate phase. To help improve refocusing efficiency, traditional RF refocusing pulses are often replaced by a composite pulse, which is a sequence of non-selective RF pulses created to have an analogous effect as an ideal 180°

pulse (36). A common composite pulse implemented in MSE imaging is the $90°_x180°_y90°_x$ pulse, where the subscripts 'x' and 'y' refer to the axis on which the pulse is applied.

In single-slice imaging, non-selective refocusing pulses can lead to a more uniform B_1 across the selected slice. The extension of MSE imaging to multi-slice imaging, however, precludes the use of these 'hard' refocusing pulses and introduces new sources of error created by 'shaped' RF refocusing pulses. In multi-slice imaging, the use of shaped RF refocusing pulses with an applied gradient creates transition regions near the edges of the selected slice, in which the flip angle varies from 180°- 0° with increasing distance from the center of the slice (33). The integrated signal across the slice does not experience a uniform B_1 and, therefore, with successive refocusing, unwanted signal is created that propagates through the measurement and can alter the amplitude of the spin echoes used for estimation of T_2. To compensate for the non-uniformity of B_1 across a slice (profile) excited with slice selective pulses, one suggestion is to increase the slice width of the refocusing pulses compared to that of the excitation pulse (37-39). In this manner, a larger region of the excited slice will experience an ideal 180° flip angle. It has been shown that a refocusing slice width that is ~2x or larger than the excitation slice width is optimal (38,39) . This technique does come with a cost, however, as a gap is required between slices to prevent cross-saturation as adjacent refocusing slice profiles will overlap.

Measures of monoexponential T_2 decay have been made in many tissue types, however, these tissues are often more complex than just a single pool of water. Most tissues contain additional constituents such as proteins and membrane bound molecules that can interact with water molecules, therefore affecting the local magnetic field and the observed T_2. More importantly, biological tissues are often characterized by different compartments

defined by cellular membranes. Micro-anatomical structures that limit water molecule interaction (i.e. cellular membranes) often lead to relaxation measures that cannot be described by monoexponential signal decay. For these measurements, more complex acquisition techniques and data modeling may be applied.

1.2 Longitudinal Relaxation (T_1)

In addition to transverse relaxation, another property, longitudinal relaxation, also has an effect on the measured NMR signal and can be influenced by tissue compartmentalization. Spin-lattice or longitudinal relaxation is described by the time constant, T_1, and can be defined as the post-excitation regrowth of magnetization (toward equilibrium) due to energy exchange between hydrogen nuclei and the surrounding environment. Following RF excitation, the transverse component of the magnetization decays, as previously described, while the longitudinal component returns towards equilibrium along the direction of B_0. The longitudinal component of the magnetization, M_z, follows

$$\frac{dM_z}{dt} = -\frac{M_z - M_0}{T_1} \quad . \qquad [2.5]$$

The solution to Eq. [2.5] following a 90° excitation pulse is described by

$$M_z(t) = M_0 + (M_z(0) - M_0)e^{-t/T_1} \qquad [2.6]$$

where M_0 represents the magnetization at thermal equilibrium and $M_z(0)$ is the amount of longitudinal magnetization observed at time t=0 after the RF pulse. In Eq. [2.6], t is the total

time from one excitation pulse to the next excitation pulse and is often referred to as the repetition time (TR) of the experiment. As a general rule, the observed value of T_1 will always be greater than or equal to the observed value of T_2.

There exists several techniques and pulse sequences for measuring T_1 (40-42). Common methods include inversion recovery and saturation recovery experiments. In a saturation recovery (SR) experiment, a 90° RF pulse is applied followed by the acquisition of either a gradient- or spin-echo. The echo is followed by a period of time in which the spins in the transverse plane are allowed to dephase while the longitudinal component of the magnetization returns toward equilibrium. This experiment is repeated for various repetition times, both shorter and longer than the expected T_1 of the tissue, to characterize the T_1 regrowth curve. In an inversion recovery (IR) experiment, a 180° pulse is used to completely invert the longitudinal magnetization and is often followed by a spin-echo or gradient echo experiment for readout. In this sequence, multiple inversion times (TI) are used with a single TR (where $TR>>T_1$) to characterize T_1 according to Eq. [2.6] where $M_z(0)$ is considered to be equal to $-M_0$ directly after the inversion pulse.

In addition to these methods, spoiled gradient-echo (SPGE) techniques have been used to characterize T_1 by varying the flip angle of the RF pulse during repeated measurements (43). In a typical SPGE experiment, a RF pulse is used to perturb the longitudinal magnetization with a flip angle less than 90°. This is followed by gradient echo readout. Residual transverse magnetization following echo formation can be 'spoiled' away (or completely dephased) prior to the next excitation to allow for acquisitions with a short TR. After a number of RF pulses, the longitudinal magnetization can be considered to be in a

steady state. The observed transverse magnetization for a SPGE acquisition (with TE < T_2*) under steady-state equilibrium conditions is

$$M_{\perp} = M_0 \frac{\sin\alpha \cdot (1 - e^{-TR \cdot R_1})}{(1 - \cos\alpha \cdot e^{-TR \cdot R_1})} \quad . \qquad [2.7]$$

The basic spoiled gradient-echo sequence has also been used to track changes in T_1 in experiments that introduce exogenous contrast agents (CA) into tissues for the purpose of pharmacokinetic characterization.

2. Compartmental Relaxation and Exchange: Two-Pool Model

2.1 Measuring Compartmental Relaxation

On the scale of proton NMR, biological tissue appears heterogeneous and results in an observable NMR signal that is a summation of spatially varying characteristics. The simplest view of tissue reflecting this heterogeneity is that of a two-pool model. Two-pool models have been widely used in MRI to describe both healthy and diseased tissue (9,14,44). The individual pools or compartments have been described in a variety of ways including representing intracellular and extracellular space or intravascular and extravascular compartments. On a sub-voxel level, if one thinks of tissue as being comprised of different compartments, it is possible to model the NMR data as a sum of signals from these compartments, each characterized by specific relaxation rates, R_1 (=1/T_1) and R_2 (=1/T_2), and relative volume fractions, f.

The two-pool tissue model, however, must also consider the movement of water, or exchange of magnetization, between compartments. Fig. 2.2 shows the basic two pool model with exchange. In Fig. 2.2 water exchange is depicted by the arrow between compartments and is represented by the mean water lifetimes, τ, in each compartment. In a general sense, exchange in MRI refers to the process by which nuclei (spins) move between different sites in a specific micro-environment. The term 'site' designates a local structure that can be characterized by physical or chemical conditions that are different than those in other sites (45). The nuclei in two different sites may be separated by a chemical shift or share the same resonance frequency. Nuclei that share the same resonance frequency, specifically water protons, may be distinguished from one another if their intrinsic relaxation rates are different. Hydrogen protons can take several forms in tissue including compartmentalized water delineated by cell membranes ("free water") as well as hydration water on the surface of proteins and other macromolecules ("bound water").

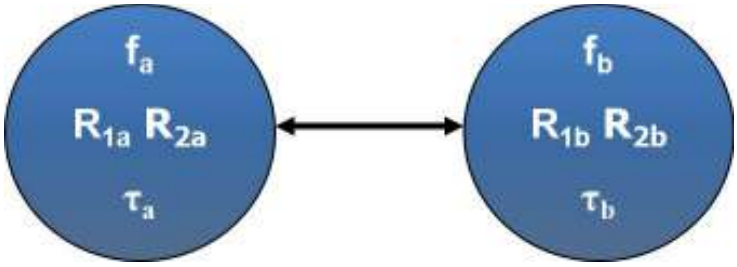

Fig. 2.2. Two pool model. Each compartment has its own relaxation rates (R_1, R_2), relative volume fractions (f_a, f_b), and mean water lifetimes (τ_a , τ_b). Note: f_a=1-f_b.

On the scale of typical tissue relaxation rates observed *in vivo*, exchange between free water and bound water is often considered to be fast. However, in certain environments the exchange of free water between cellular compartments (i.e. intracellular-extracellular

exchange) is slow enough that multiple signal components can be discerned. As a result, tissue relaxation rates have been observed to be multiexponential in nature (e.g. nerve, muscle, white matter). In the two-pool model one may observe bi-exponential signal decay described by

$$S(t) = f'_a e^{(-TE \cdot R'_a)} + f'_b e^{(-TE \cdot R'_b)} \qquad [2.8]$$

where the ' superscript distinguishes observed parameters and R_a and R_b can represent either transverse or longitudinal magnetization. The observed estimates of these tissue relaxation rates as well as relative compartment sizes are influenced, however, by the rate of inter-compartmental water exchange.

To measure the observable parameters from Eq. [2.8] for transverse relaxation, MSE measurements can be implemented (30,31). In particular, a Carr-Purcell-Meiboom-Gill (CPMG) based sequence can be employed. The CPMG acquisition is similar to a basic multiple spin-echo sequence, with the exception that the 90° excitation pulse is applied with a 90° phase shift relative to the 180° pulse, thereby reducing errors from imperfect refocusing. For T_2 quantification, the CPMG acquisition is commonly modified with spoiler gradient pairs surrounding the refocusing pulses to help eliminate signal from unwanted coherence pathways (33,34). A basic single-slice multiple spin-echo pulse sequence used for quantifying multiexponential T_2 (MET_2) can be seen in Fig. 2.3. As previously discussed, non-slice selective composite refocusing pulses are implemented in this sequence to improve refocusing efficiency (36). As illustrated in Fig. 2.3, the acquisition of so-called ‘late’ echoes

is also be incorporated into the basic singe-slice MSE sequence to sample any long-lived T_2 signal that might be present (46).

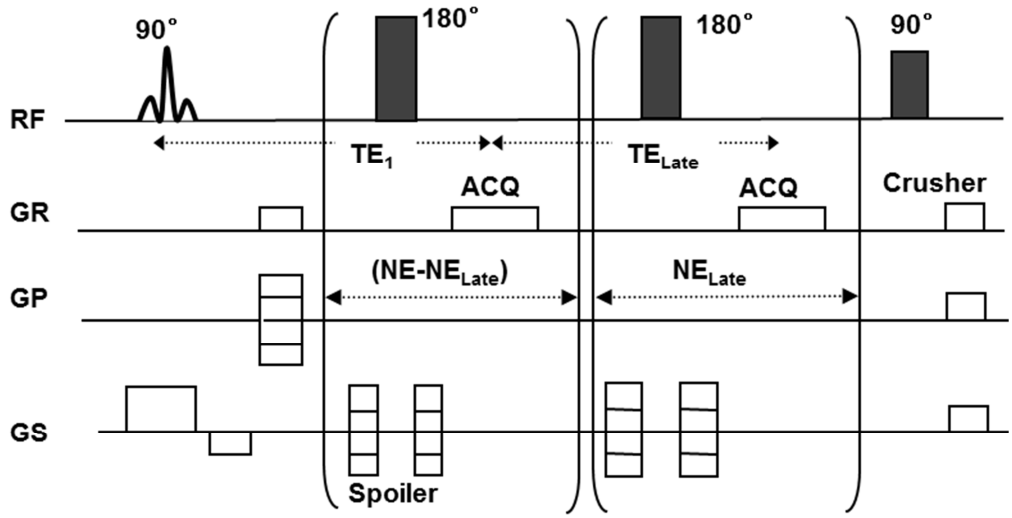

Fig. 2.3. Single-slice multiple spin-echo pulse sequence. Note the spoiler gradient pairs and the hard refocusing pulses. NE: number of echoes, NE_{late} : number of late echoes, TE: echo time, TE_{late}: TE of late echoes, GR: readout gradient, GP: phase encode gradient, GS: slice select gradient.

Common methods for extracting T_2 values from MSE data often include fitting the data in a non-linear least squares manner to either a monoexponential or bi-exponential function (Eq. [2.8]). In a multi-compartment tissue, however, an effective way of visualizing the distribution of T_2s and relative compartment sizes is to create a so called T_2 spectrum. In this type of analysis, the multi-echo data is fit in a non-negative least squares (NNLS) manner to a sum of decaying exponentials

$$S_i = \sum_{j=1}^{M} S_{0j} \cdot e^{-TE_i / T_{2j}} \text{ , i = 1,2,…,N} \qquad [2.9]$$

where S_{0j} are the M amplitudes for each T_{2j} in the distribution and S_i represents the N measured decay points at times TE_i. Eq. [2.9] can be re-written in a general form with the variable A_{ij} replacing the exponential terms and y_i replacing S_i such that

$$y_i = \sum_{j=1}^{M} A_{ij} s_j \text{ , i=1,2,…N.} \qquad [2.10]$$

The NNLS fitting can then be used to minimize

$$\sum_{i=1}^{N} \left[\sum_{j=1}^{M} A_{ij} s_j - y_i \right]^2 + \mu \sum_{k=1}^{K} \left[\sum_{j=1}^{M} H_{kj} s_j \right]^2 \quad , \qquad [2.11]$$

where H_{kj} is a matrix containing K additional constraints that represent the smoothing model being used (i.e. energy, derivative, curvature etc.) and μ is the regularization parameter used to tradeoff between the minimum misfit and the solution smoothness (47). A T_2 spectrum can then be constructed from which T_2s and relative volume fractions for each observed compartment can be extracted. Example T_2 decay data and the resulting T_2 spectrum can be seen in Fig. 2.4.

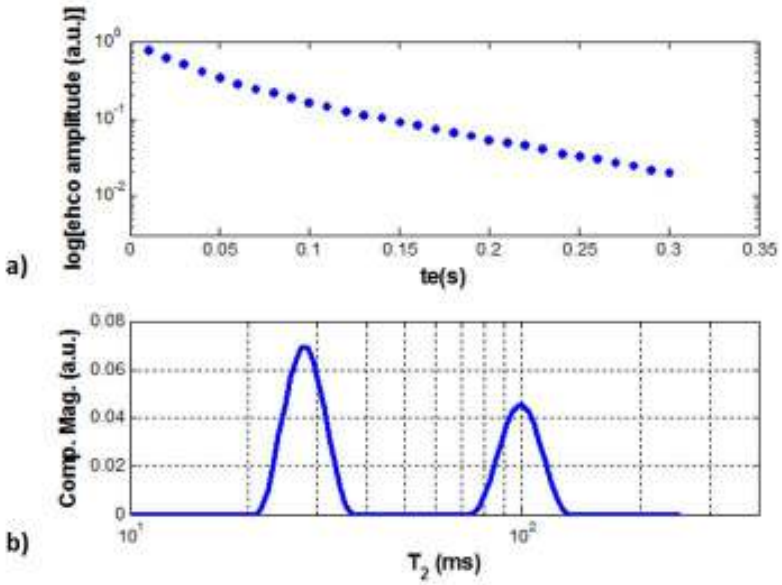

Fig. 2.4. a) Example T_2 decay curve and b) corresponding T_2 spectrum showing multi-exponential T_2.

2.2 Measuring Water Exchange

When modeling tissue as a multi-compartment system, consideration should be given to the effect of the rate of water exchange on the observed parameter values. In addition to measures of exchange, the relative size of the cellular spaces in a given tissue is also important, as these spaces can change with pathology and injury. Quantitative MRI analysis of physiological processes such as inflammation, cell proliferation, and necrosis can result in measured volume fractions that may reflect a specific injury or disease, though the measures, themselves, may be biased by exchange.

Measures of water exchange can be incorporated into the analysis of relaxation data to aid in obtaining a more reliable model of tissue. The mathematical description (a modification to the original Bloch equations (28)) can be seen in Eq. [2.12a] and [2.12b]:

$$\frac{dM_a(t)}{dt} = R_a[M_{0a} - M_a(t)] - \frac{M_a}{\tau_a} + \frac{M_b}{\tau_b} \qquad [2.12a]$$

$$\frac{dM_b(t)}{dt} = R_b[M_{0b} - M_b(t)] - \frac{M_b}{\tau_b} + \frac{M_a}{\tau_a} \qquad [2.12b]$$

where R_a and R_b are relaxation rates that can refer to transverse or longitudinal relaxation and M_0 is the magnetization at equilibrium.

Algebraic solutions to the two-pool model with exchange were formulated by Zimmerman and Brittin with subsequent work by McConnell and Woessner (45,48,49). The observed relaxation rates have been shown to be related to the intrinsic rates and mean water lifetimes by

$$R_a' = \frac{1}{2}\left[R_a + R_b + \frac{1}{\tau_a} + \frac{1}{\tau_b}\right] + \frac{1}{2}\sqrt{\left(R_b - R_a + \frac{1}{\tau_b} - \frac{1}{\tau_a}\right)^2 + \frac{4}{\tau_a\tau_b}} \qquad [2.13]$$

$$R_b' = \frac{1}{2}\left[R_a + R_b + \frac{1}{\tau_a} + \frac{1}{\tau_b}\right] - \frac{1}{2}\sqrt{\left(R_b - R_a + \frac{1}{\tau_b} - \frac{1}{\tau_a}\right)^2 + \frac{4}{\tau_a\tau_b}} \qquad [2.14]$$

Additionally the observed relative volume fractions are described by

$$f_a' = \frac{1}{2} - \frac{1}{4}\left[(f_a - f_b)(R_b - R_a) + \frac{1}{\tau_a} + \frac{1}{\tau_b}\right] \Bigg/ \left[\frac{1}{2}\sqrt{\left(R_b - R_a + \frac{1}{\tau_b} - \frac{1}{\tau_a}\right)^2 + \frac{4}{\tau_a\tau_b}}\right] \qquad [2.15]$$

$$f_b' = 1 - f_a' \qquad [2.16]$$

In certain limiting cases, such as when exchange is very slow such that

$$\frac{1}{\tau_a} + \frac{1}{\tau_b} << \left| R_b - R_a \right| \quad , \qquad [2.17]$$

the observed relative volume fractions are close to their intrinsic values and the observed relaxation rates are calculated as

$$R_a' = R_a + 1/\tau_a \qquad [2.18a]$$

$$R_b' = R_b + 1/\tau_b \qquad [2.18b]$$

If the exchange between compartments is very fast such that

$$\frac{1}{\tau_a} + \frac{1}{\tau_b} >> \left| R_b - R_a \right| \qquad [2.19]$$

then a single average relaxation rate is observed. In this case the observed signal decay will likely appear monoexponential in nature. A difficulty arises, however, in attempting to measure water exchange rates when the rate of compartmental exchange is in the intermediate regime.

Measures of water exchange rates were first investigated *in vitro* in the study of red blood cell (RBC) permeability (50-53). In several of these studies, a paramagnetic contrast agent (Mn^{2+}) was added, in various concentrations, to alter the intrinsic relaxation rate of the extracellular compartment (plasma). Two different signal components could then be observed in blood, an otherwise fast-exchanging system. Subsequent mathematical modeling led to the extraction of mean water lifetimes. Analytical evaluations of changes in relaxation rates with and without contrast have led to assumptions about the range of compartmental lifetimes and exchange rates in various excised and/or perfused tissues (54-56).

Additional methods of measuring water exchange have focused on closing the two-site exchange equations with an independent measure of one of the model parameters. A study by Mulkern *et al.* used two or more concentrations of contrast agent to obtain several observations of compartmental relaxation rates from bi-exponential fits to T_2 decay curves (19). The volume fractions and exchange rates were assumed unchanged with paramagnetic doping and the intrinsic model parameters were calculated from the observed parameters through solutions to the two-pool exchange equations. The analysis provided reasonable exchange rates with samples of whole blood, but physically irrelevant values of exchange with perfused rat heart data. In addition to this type of experiment, 2D NMR correlation studies have been proposed as a means of studying exchange in porous media (57-59). A recent study by Dortch *et al.* focused on the development and validation (via a urea phantom) of a relatively fast method, IR-REXSY, for measuring exchange in a 2D NMR experiment (18). Though these measurements are being evaluated in biological tissue samples, they are currently limited to non-imaging *ex vivo* application.

In other studies, the effect of proton exchange has been investigated in contrast enhanced imaging of biological tissues. In a study of perfused rat heart, Donahue *et al.* measured tissue T_1 with various concentrations of Gd-DTPA and found monoexponential signal decay in T_1 and bi-exponential decay in T_2 relaxation times (54). Based on the difference in compartmental relaxation times on a T_1 and T_2 timescale, it was concluded that the range of intracellular-extracellular exchange rates in cardiac tissue was between $8s^{-1}$ and $27s^{-1}$. Yet another study by Donahue *et al.* looked at the effect of vascular-interstitial exchange and vascular size on the estimation of the extracellular volume fraction *in vivo* (60). It was reaffirmed that the exchange regime of a biological system depended on the relative value of the exchange rate compared to the difference between compartmental relaxation rates, which are dependent on contrast agent concentration (61). Recently, the use of CAs has been extended to dynamic MRI acquisitions that attempt to extract values of compartmental mean water lifetimes *in vivo* via pharmacokinetic modeling.

3. Compartmental Relaxation with Contrast Agents

3.1 Contrast Agent Based Relaxation Effects

Exogenous contrast agents have been used in MRI to alter NMR tissue properties and, therefore, the MR signal for the purpose of highlighting a particular pathology or anomaly in a tissue. The resulting change in MR signal with contrast introduction can be attributed to changes in the relaxation properties of the tissue as the CA interacts with the water molecules. The CA-water interaction often serves to shorten relaxation times T_1 and T_2 depending on the type of agent and concentration. Many MRI CAs are based on paramagnetic Gd(III) chelates

that reduce the observable T_1 (and T_2 at higher concentrations) in tissue. A common Gd(III) chelate, gadopentetate dimeglumine (Gd-DTPA), has been used in many clinical applications including blood vessel and tumor imaging (62-64).

In contrast enhanced MRI experiments, the distribution of the CA is typically based on the size and chemical composition of the contrast and its' chelate. CAs can remain intravascular after injection, leak out of the vasculature into the interstitium, or may accumulate in a specific region targeted by the CA. For a single well-mixed compartment in biological samples, the measured relaxation rate, R, in the presence of contrast can be described by (27)

$$R = R_0 + r \cdot [CA] \qquad [2.20]$$

where R_0 is the intrinsic relaxation rate in the absence of contrast, r is the relaxivity of the contrast agent, and [CA] is the contrast agent concentration. In biological tissue, however, distribution of CA is often not limited to just a single compartment and therefore two-pool models of CA distribution can be created for the purpose of pharmacokinetic modeling.

3.2 Contrast Agent Distribution: Two Pool Model

Pharmacokinetic analysis of contrast agent distribution is based on several assumptions. First, the tissue is considered to be represented by one or more compartments through which contrast agent is able to flow. Second, the compartments are considered to be "well mixed" in the sense that the contrast agent is uniformly distributed throughout the compartment. A pharmacokinetic model for contrast agent kinetics in tissue is shown below in Fig. 2.5.

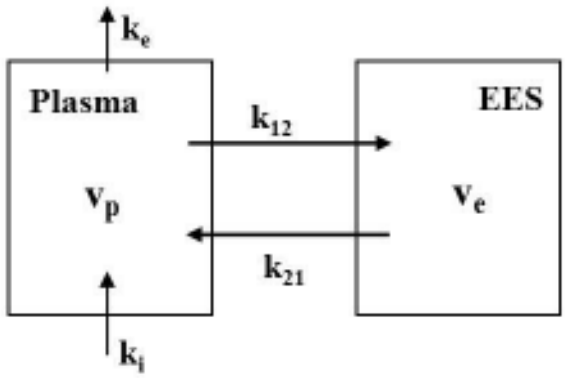

Fig. 2.5. Two-pool pharmacokinetic model for CA distribution. The compartments considered are the blood plasma space and the extravascular-extracellular tissue space, represented by the volumes v_p and v_e. k_{12} is the volume transfer constant between plasma and EES. k_{21} is the rate constant between EES and plasma, where $k_{21}=k_{12}/v_e$.

The two-compartment pharmacokinetic model depicts the in-flow of the contrast agent into the plasma space, represented by the plasma volume fraction v_p, with rate constant k_i. The contrast agent also diffuses, in a reversible process, into the extravascular-extracellular space (EES), represented by v_e, with the volume transfer constant k_{12} (i.e. K^{trans} in DCE-MRI). The agent can then diffuse back into the plasma space with a rate constant, k_{21}. The contrast agent is then eliminated with a rate constant k_e. Based on the model in Fig. 2.5 (65), the change in concentration of the CA agent in the tissue after injection can be described by the differential equation

$$\frac{dC_t(t)}{dt} = k_{12} \cdot C_p(t) - k_{21} \cdot C_t(t) \quad , \qquad [2.21]$$

where $C_p(t)$ and $C_t(t)$ are the CA concentrations in the plasma and tissue at time, t. Solving Eq. [2.21] (using an integrating factor) for $C_t(t)$ provides a common mathematical model for analysis of dynamic contrast-enhanced MRI data (21).

3.3 DCE-MRI

Tumor viability and composition as well as the integrity of tissue vasculature can be assessed by monitoring the changes in MR signal intensity with contrast agent distribution using T_1 relaxometry. The technique for making these measurements is referred to as dynamic contrast enhanced MRI (DCE-MRI). Kinetic modeling of DCE-MRI data can provide quantitative measures relating to perfusion and permeability (K^{trans}), and the extracellular-extravascular volume fraction (v_e) (22). The signal intensity in DCE-MRI measurements is indirectly affected by the contrast agent as it alters the relaxation properties of exchanging water in the tissues. To track the wash in and wash out of the contrast agent in the tissue, a SPGE experiment can be implemented. In this experiment, the signal intensity time courses in tissue and blood are related to R_1 by

$$R_1(t) = \frac{1}{TR} \ln\left[\frac{S_0 \cdot \sin\alpha - S(t) \cdot \cos\alpha}{S_0 \cdot \sin\alpha - S(t)} \right] \qquad [2.22]$$

where α is the flip angle, S_0 is the initial signal intensity, pre-contrast, based on the SPGE acquisition (Eq. [2.7]), and $S(t)$ is the measured signal intensity at a time t after contrast injection.

In most cases, modeling of DCE-MRI data requires a measure of the concentration of contrast agent in the plasma with time. This measure is known as the arterial input function (AIF) or vascular input function (VIF) and is often obtained from a region of interest in a large artery within close proximity to the tissue of interest (66,67). Considering the two-pool

model in Fig. 2.5, it is assumed that the distribution of the CA in the blood is restricted to the plasma and, therefore, in the context of a DCE-MRI experiment, $C_p(t)$ can be computed

$$C_p(t) = \frac{R_{1b}(t) - R_{10b}}{r_1(1-h)} \quad [2.23]$$

where R_{1b} is the relaxation rate in the blood after contrast injection, R_{10b} is the intrinsic relaxation rate before contrast, h is the hematocrit, and r_1 is the relaxivity of the CA in the plasma.

If the intracellular and extracellular compartments in the tissue of interest are assumed to be in fast water exchange, the relaxation rate in the tissue at a time t after contrast injection, $R_{1t}(t)$, can be computed (23)

$$R_{1t}(t) = R_{1to} + r_1 \cdot v_e \cdot C_t(t) \quad [2.24]$$

where $C_t(t)$ is,

$$C_t(t) = K^{trans} \cdot \int_0^t C_p(T) \cdot (-(K^{trans} / v_e) \cdot (t-T))dt\,. \quad [2.25]$$

K^{trans} and v_e can then be estimated by fitting $C_p(t)$ and $R_{1t}(t)$ with Eq. [2.24] and Eq. [2.25]. Eq. [2.25] is often referred to as the Tofts model and is the solution to the differential equation in Eq. [2.21] (21). In the case of heavily vascularized tissues such as tumor, the Tofts model can also be extended (21) to include contributions from the plasma space, v_p.

Though the previous analysis is valid in many tissues, a few studies have shown that water exchange is not sufficiently fast at all values of C_t to assume monoexponential relaxation at all times during a contrast enhanced experiment (17,23). Under these conditions, the mean water lifetime can be included in the dynamic modeling and extracted from fitting of the DCE data with equations similar to Eq. [2.13] and [2.14]. The inclusion of water exchange in the modeling of DCE-MRI data and interpretation of the resulting fit parameters, however, is still a matter of debate. In addition to the effects of exchange, the value of the pharmacokinetic parameters (i.e. v_e) have been shown to vary depending on the model selected for analysis as well as the level of perfusion and vascularization in the tissue of interest (68). Aside from model selection, the DCE-MRI experiment itself provides challenges in obtaining physiologically relevant measures of the model parameters due to errors in the VIF caused by flow effects and temporal sampling requirements (69,70). For these reasons, methods for validating DCE-MRI measurements need to be explored.

4. SPECT Imaging

The use of CAs with relaxation-based measurements in MRI provide quantitative measures of compartmental tissue characteristics, however, these measures are only indirect indicators of CA distribution. Furthermore, tissue water dynamics such as compartmental exchange and diffusion may contribute to altering the observed values of compartmental tissue properties, including relaxation rates and compartmental volume fractions. In contrast, nuclear imaging offers the advantage that the observed signal from an injected radiotracer is measured directly and is independent of tissue water dynamics. One nuclear imaging modality, single

photon emission computed tomography (SPECT), can potentially be useful (in a pre-clinical setting) as compartment specific radiotracers can be synthesized and imaged *in vivo*.

SPECT is a tomographic nuclear medicine imaging technique that detects gamma ray emission from a previously injected radionuclide (71). Gamma cameras and their associated detectors are used with a geometry-specific lead collimator array to help reduce scatter and detect emissions from a specific source in the tissue (71). Images are created by acquiring multiple 2D projections at various angles. Iterative reconstruction of the projection data is often carried out using a modified back-projection method to create a 3D data set representative of the radionuclide distribution. Among other parameters, the resulting image quality in SPECT is largely based on collimation efficiency, the type of detectors used, and the number of counts recorded. The number of projections and time spent counting at each projection is often a tradeoff between the desired experimental time and the attainable SNR, as the SNR scales with the square root of the number of photons per unit area. Ultimately, optimizing these aforementioned parameters and processes can provide image data sets that can be analyzed in a quantitative manner.

Unique to SPECT is its ability to discriminate radionuclides based on the energy of the gamma rays emitted. This property is in contrast to imaging modalities such as positron emission tomography (PET) where all photons detected are at the same energy (511 keV). In typical SPECT experiments energy windows are set about a photopeak representing the energy of a particular radionuclide. The energy windows are used to select photons from a given source while reducing the contribution from scattered photons. The more narrow the energy window the fewer scattered photons are counted, and the sharper the image appears. In this case, however, the sensitivity is reduced, due to ‘good’ counts that are discarded,

resulting in a noisier image. The converse is true with a wider energy window. For most experiments the optimal energy window is set between 10% and 20% depending on the detector and the location of the radiotracer photopeak. The illustration in Fig. 2.6 shows an example energy spectrum and 20% energy windows for two commonly used SPECT radionuclides, ^{99m}Tc and ^{111}In.

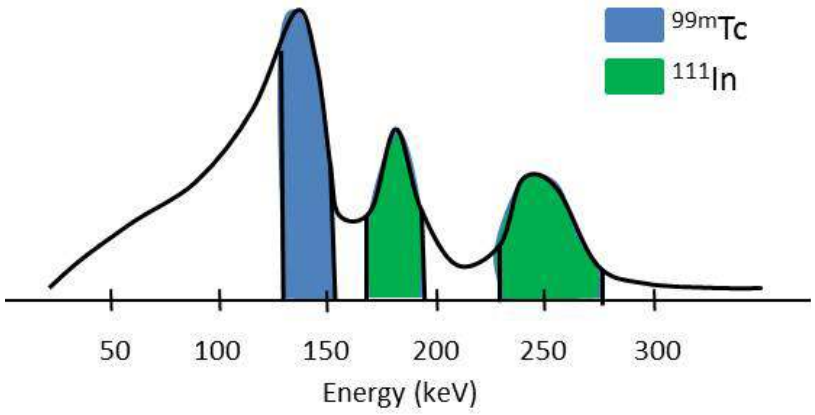

Fig. 2.6. Energy spectrum and energy windows for ^{99m}Tc (photopeak:140 keV) and ^{111}In (photopeak: 171 keV, 245 keV). The non-shaded regions represent areas of scatter and cross-talk. Note the two peaks of the ^{111}In radionuclide.

In pre-clinical (and clinical) SPECT studies, radionuclides are often attached to or chelated with biochemical substances to create radio-ligands and radio-pharmaceuticals that target specific regions of the micro-anatomy or specific bio-chemical processes. Examples of common radio-pharmaceuticals are ^{99m}Tc-Sestamibi for myocardial perfusion imaging (72), ^{99m}Tc-HMPAO for brain imaging (73), and ^{123}I-MIBG for tumor imaging (74). Similar to CA in MRI, SPECT radiotracers can also be created to identify specific tissue compartments. Radionuclides such as ^{99m}Tc and ^{111}In can be labeled with DTPA to create an extracellular tracer, with CA distribution characteristics similar to Gd-DTPA. Radiotracers that are restricted to the vasculature can also be created, as red blood cells (RBCs) can be labeled

with ^{99m}Tc (75). Taking advantage of the energy discrimination inherent with SPECT, multiple radiopharmaceuticals have also been injected and imaged simultaneously (76,77).

4.1 Dual-Isotope Imaging

Dual-isotope imaging provides a novel method for targeting two different processes or tissue types using different radionuclides. Provided the photopeaks of the desired radionuclides have sufficient separation, individual images for each radionuclide can be created in a single scan. Selection of radionuclides for dual-isotope imaging depends not only on photopeak separation but also the half-life ($\tau_{1/2}$). Radionuclides used in clinical applications include ^{99m}Tc (140 keV, $\tau_{1/2}$ = 6h), ^{201}Tl (135kev/167 keV, $\tau_{1/2}$ = 73h), ^{123}I (159 keV, $\tau_{1/2}$ = 13.3 hr), and ^{111}In (171keV/245keV, $\tau_{1/2}$ = 67 hr). Example applications of dual-isotope SPECT include ^{201}Tl /^{99m}Tc-MIBI for same day rest/stress tests (78) and ^{99m}Tc-ECD/^{123}I-FP-CIT for detection of Parkinson's disease and multiple system atrophy (79). Dual-isotope imaging can also be used for distinguishing different tissue compartments. An example of this type of application can be seen in Fig. 2.7 (methods for these acquisitions can be seen in Chapter 4). Fig. 2.7a shows the distribution of ^{99m}Tc labeled red blood cells in the rat vasculature. Fig. 2.7b shows signal from ^{111}In-DTPA inside the brain where the blood brain barrier has been disrupted due to tumor growth while signal from ^{99m}Tc-RBCs is primarily contained in the vessels. The distribution of ^{111}In-DTPA in this case is analogous to that of Gd-DTPA in rat brain tumors imaged with MRI.

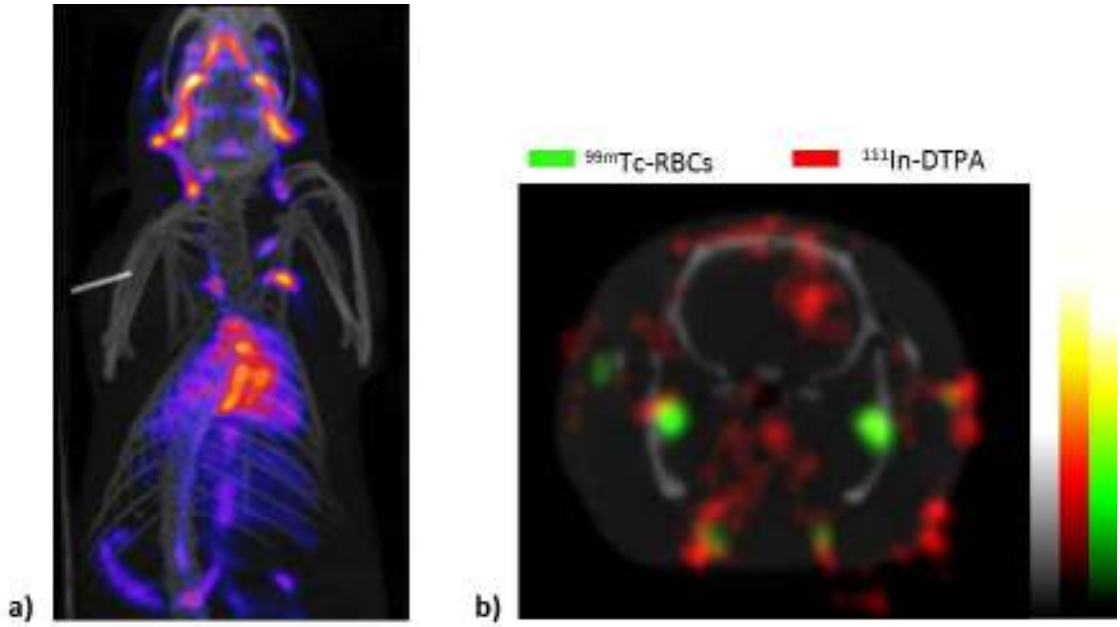

Fig. 2.7. a) Maximum intensity projection image of a rat injected with ^{99m}Tc-RBCs. b) Axial image of a C6 glioma in rat using ^{99m}Tc-RBCs and ^{111}In-DTPA. Note the ^{111}In-DTPA signal in brain and ^{99m}Tc-RBC signal in the vessels .

4.2 Quantitative SPECT Analysis

SPECT data is often analyzed in a semi-quantitative manner, based on the information gleaned from the images themselves. Individual SPECT images contain information about the amount and distribution of radiotracer activity in a given tissue and, therefore, quantification of activity in a region of interest is common in SPECT (76). Activity measures can be made in a dynamic manner to calculate area under the curve (AUC) metrics or washout rates, though these measures may require special hardware as well as an arterial input function (as used in PET and MRI). The accuracy of these measurements, however, can also be affected by attenuation and scatter. Gamma rays traverse much shorter paths and therefore experience significantly less attenuation and scatter in rodents than in humans. Attenuation can pose a problem, however, with lower energy photons (e.g. ^{125}I), though it is less significant with higher energy photons (e.g. ^{99m}Tc and ^{111}In as used in these studies).

There is a question of whether scatter or attenuation correction is necessary in small animal SPECT or whether the corrections themselves are apt to introduce additional noise into the images (80). In general, overestimation errors typically resulting from scatter are offset by underestimation errors caused by photon attenuation and partial-volume effects in small animal SPECT (80,81).

It is to be noted, that common SPECT analysis techniques alone do not necessarily provide quantitative information about the underlying tissue compartment sizes. Alternatively, the concentration of a radiotracer in tissue or a blood sample may be calculated and used to compute a blood-to-brain transfer constant (K_i) or volume of distribution (82-84). These types of quantitative measurements have been made in *ex vivo* animal models using autoradiography (AR) techniques, but have yet to be incorporated into *in vivo* imaging due to radiotracer and experimental design limitations. The importance of quantitative SPECT measurements and their role in characterizing vascular and interstitial tissue spaces has been noted in several review articles (85,86). Of added value, is recognizing that the signal recorded in a SPECT experiment is independent of tissue water dynamics, a factor that often affects accurate quantification of MRI measurements.

Considering the previously described capabilities of small animal SPECT imaging, obtaining *in vivo* estimates of tissue compartment sizes with SPECT is possible. To perform these measurements, however, an appropriate radiotracer must be selected and imaging protocol designed. First, a radiotracer should be selected that distributes in the tissue space that one wants to measure. As Gd-DTPA is used to probe the extracellular tissue space in DCE-MRI, a radiotracer can be synthesized that exhibits the same CA distribution characteristics. For example, DTPA can be labeled with ^{111}In to create ^{111}In-DTPA. To obtain

the sought after tissue volume fractions, one needs to start with tissue activity measurements. To begin, the SPECT system image intensity is calibrated to measures of activity. A sample solution of the given radiotracer (e.g. ^{111}In), with a known activity (measured from a well counter) and volume, is scanned with the appropriate imaging protocol. The image signal intensity is integrated over the sample and compared to the known activity to create a calibration factor for quantification. This is repeated for any radiotracer that is to be imaged.

Upon injection into an animal, a radiotracer such as ^{111}In-DTPA will distribute throughout the plasma space and the extracellular extravascular tissue space. Prior to radiotracer injection, however, a nephrectomy procedure can be performed, to ensure that the radiotracer reaches a state of equilibrium between the extracellular space (EC) and plasma creating a condition where

$$\left[{}^{111}In\right]_{EC} = \left[{}^{111}In\right]_{plasma}. \qquad [2.26]$$

Similar procedures have been previously performed in *ex vivo* radiotracer studies to help calculate tissue volume fractions via the relationship in Eq. [2.26]. With the concentration defined as the activity per volume (MBq/mL), the extracellular volume is

$$V_{EC} = \frac{A_{EC}}{A_{plasma}} \cdot V_{plasma}\ , \qquad [2.27]$$

where measures of extracellular tissue activity (A_{EC}) are recorded from the tissue of interest. A plasma sample with known volume (V_{plasma}) is also acquired to measure A_{plasma}. The

SPECT derived estimate of the extracellular volume fraction from a given region of interest (ROI) is thus estimated as:

$$v_{e,SP} = \frac{V_{EC}}{V_{tissue}} = \frac{A_{EC}V_{plasma}}{A_{plasma}V_{tissue}}, \quad [2.28]$$

where V_{tissue} is the known volume of a ROI in the SPECT experiment. This model is appropriate for tissues in which the vasculature is not a significant fraction of the total tissue space or ROI (i.e. <1%). In tissues that have the potential for being highly vascularized (e.g. tumors), this model can be extended.

To account for the contribution of the vasculature in a tissue of interest (TOI), a second radiotracer can be used. In this instance, RBCs can be labeled with ^{99m}Tc to create a blood vessel specific radiotracer, ^{99m}Tc-RBC. A dual-isotope approach can then be used to acquire simultaneous images of both ^{111}In-DTPA and ^{99m}Tc-RBCs distribution in the TOI. Following a similar procedure as the single tracer case, a nephrectomy can be performed to allow the extracellular radiotracer to reach equilibrium between the vascular (blood) space and the extracellular-extravascular (ECEV) space such that

$$C_{^{111}In,blood} \approx C_{^{111}In,ECEV}. \quad [2.29]$$

The concentration, C, of tracers in a blood sample can be determined from the SPECT image of the blood sample itself

$$C_{99mTc,blood} = A_{99mTc,blood} / V_{blood} \quad \text{, and} \qquad [2.30]$$

$$C_{111In,blood} = A_{111In,blood} / V_{blood} \text{ ,} \qquad [2.31]$$

where V_{blood} is the known volume of the blood sample and A is the specified radiotracer activity (in MBq) from the entire sample in the SPECT image of the blood. Similarly, the activity in the TOI is described by

$$A_{99mTc,tissue} = C_{99mTc,blood} \cdot V_{IV} \text{ , and} \qquad [2.32]$$

$$A_{111In,tissue} = C_{111In,blood} \cdot V_{IV} + C_{111In,ECEV} \cdot V_{ECEV} \text{ ,} \qquad [2.33]$$

where V_{IV} and V_{ECEV} are the volumes of the intravascular space and extracellular extravascular space, respectively, in the tissue. Given the measured activities in a ROI and tracer concentrations in the blood from Eqs. [2.30] and [2.31], Eqs [2.29], [2.32] and [2.33] can be solved to calculate V_{IV} and V_{ECEV}. From here, v_e can be estimated as

$$v_{e,SP} = V_{ECEV} / V_{tissue} \text{ .} \qquad [2.34]$$

where V_{tissue} was the known volume of the ROI in the SPECT images. In this way, estimates of the extracellular volume fraction in tissue can be computed with *in vivo* SPECT imaging, for comparison with estimates obtained from MRI.

5. Application of Relaxation-Based MRI Measurements

5.1 Experimental Tissue Models

The previously described techniques aim to characterize tissue microstructure on a compartmental basis. These compartments can range from intra- and extracellular tissue spaces to intra- and extravascular spaces. Various tissues have been analyzed in this manner using MRI including nerve, white matter, muscle, bone, and solid tumors (5,7,8,17,87,88). Of particular interest to the work presented in this dissertation is muscle tissue compartmentalization.

As early as 1969, there was experimental evidence that two phases of water existed in skeletal muscle and the phenomena that explained these signals involved the restriction of the motional freedom of the water molecules (11). In a later study, Hazlewood *et al*. suggested that there were three different fractions of exchanging water in rat skeletal muscle, corresponding to three distinct T_2 times (12). The three components were designated as hydration water molecules of protein and macromolecules (7% of muscle water, T_2<1ms), myoplasm or intracellular water (83% of muscle water, T_2~44ms), and extracellular space (10% of muscle water, T_2~155ms). Support for the physical compartment model was strengthened when Cole *et al*. found that maceration of skeletal muscle resulted in a loss of biexponential T_2 decay, specifically a loss of the long T_2 component (9). This result affirmed the idea that the observed biexponential signal could be attributed to intracellular and extracellular tissue compartments. Though healthy muscle tissue has been shown to exhibit multiexponential relaxation in humans, there is still some debate as to the number and assignment of the individual tissue compartments (10,89).

In recent years, studies have measured T_2 decay in a variety of models that explore injury and inflammation in skeletal muscle. A common non-pathologic model, due to its utility in human imaging, looks at exercise-induced changes in T_2 and volume fractions (90-92). As metabolic expense and perfusion increase with exercise, net water transfer occurs between vascular and extravascular compartments and total muscle water content increases (91). This increase often results in a change in T_2 and, therefore, image contrast. In particular, the increase in T_2 with exercise may be partly attributed to intracellular fluid accumulation associated with metabolites and intracellular acidification (90). In small animals, electroporation injury is sometimes used to model edematous muscle and to observe changes in muscle tissue after membrane trauma (93). Another small animal model, compression-induced deep tissue injury focuses on how damage to the muscle fibers results in edema and inflammation, as well as necrosis (94). A femoral artery ligation model can be used to evaluate perfusion recovery from peripheral vascular disease or critical limb ischemia (95). This model, often induced in rat hindlimb, has been the focus of several studies using DCE-MRI and diffusion-weighted imaging to assess muscle perfusion, angiogenesis, inflammation, and tissue regeneration (88,95-97).

Aside from physically inducing injury and inflammation, edema can also be induced via injection of a chemical compound. Gambarota *et al*. used injections of saline of various tonicities to produce MET_2 in rat skeletal muscle (6). As a result, both fast and slow decaying T_2 components were observed in the muscle. The osmotic manipulation of the compartment sizes extracted from edematous muscle allowed the assignment of the fast and slow T_2 components to intra-cellular and extra-cellular water, respectively. The injection of a chemical agent, such as λ-carrageenan, is another common method of inducing edema in

muscle. Carrageenan-induced edema is mediated in a temporal manner by serotonin and histamine at first, then kinins, and finally prostaglandins about 3 hours after injection (98,99). Known for its use in the development of non-steroidal anti-inflammatory drugs, the carrageenan-induced edema model is often used in rat paw and hindlimb as a way to simulate an inflammatory response (100,101).

Recent studies by Ababneh *et al*. and Fan and Does have implemented this particular model to study MET_2 and diffusion in muscle inflammation (14,15). In addition, a two-dimensional T_1-T_2 study, similar to that of Saab *et al*. (102), was performed, prior to the work presented here, to characterize compartmental relaxation in graded muscle edema using the λ-carrageenan injury model (16). A SR-MSE experiment was implemented to investigate the possibility of both multiexponential T_1 and T_2 in injured muscle. An example of the resulting T_1-T_2 spectrum for both normal and edematous muscle can be seen in Fig. 2.8.

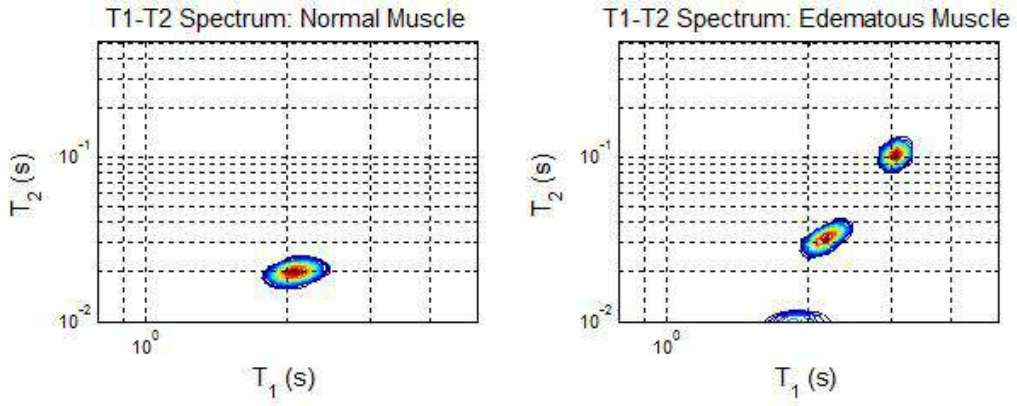

Fig. 2.8. T_1-T_2 spectra of healthy muscle (left) and edematous muscle (right).

The presence of both multi-compartment T_1 and T_2 with injured muscle demonstrates that water in this particular tissue is likely in an intermediate or slow exchange regime. Based on this observation, the λ-carrageenan injury model provides a basis for further research aimed

at extracting estimates of intrinsic compartmental parameters for the purpose of assessing the effect of exchange on these parameters.

5.2 Translation of Quantitative T_2 Measurements

Though relaxation measurements are often implemented in pre-clinical animal models, as previously described, these techniques, particularly MSE experiments, are used infrequently in the clinic. Characterization of MET_2 is traditionally achieved by MSE measurements acquired in a single slice or in a single voxel. These experiments tend to have long acquisition times, are sensitive to motion, and preclude multi-slice imaging. In traditional MSE imaging a single line of k-space is acquired at each echo time during a TR. Fast spin-echo (FSE) methods can been used to decrease acquisition time for the purpose of multi-slice monoexponential T_2 characterization. The basic differences between spin-echo and fast spin-echo sequences can be seen in Fig. 2.9. Rapid T_2-weighted imaging sequences (RARE, GRASE, etc.) have been implemented in clinical applications to reduce scan time while exploiting T_2 contrast. These multi-shot methods, however, do not provide a large time advantage for the acquisition of data at a number of echo times sufficient for multi-exponential signal decay.

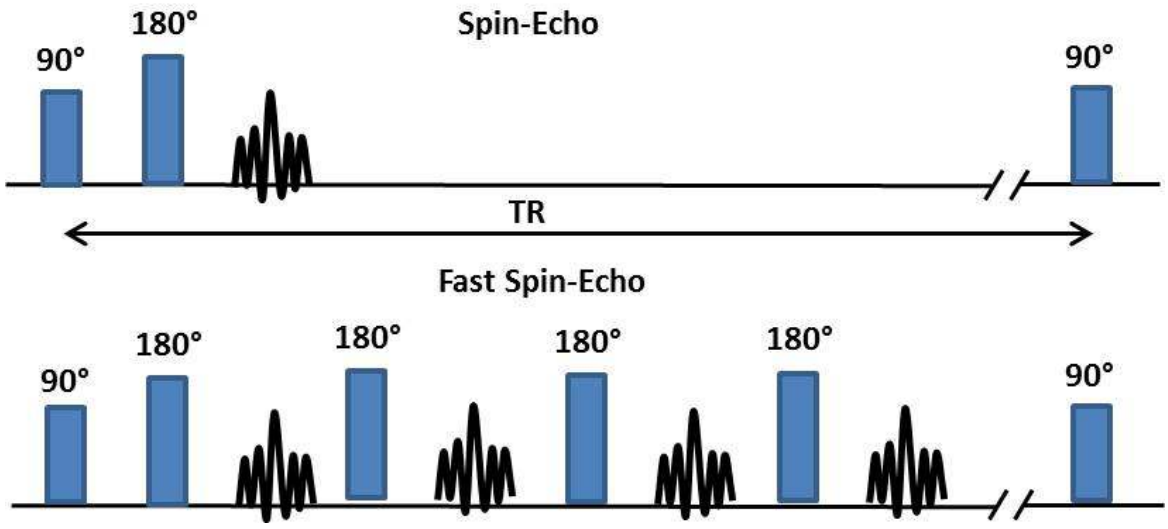

Fig. 2.9. Characteristics of conventional spin-echo and fast spin-echo (FSE) imaging sequences.

To decrease acquisition time, an entire image can be collected with an effective TE in a single TR. This is known as single-shot spin-echo imaging. To further increase speed of acquisition, one can take advantage of partial Fourier methods (103). In partial Fourier acquisitions, data are collected asymmetrically around the center of k-space. Typically, one half of k-space is completely acquired (in the phase encoding direction) as well as a fraction of the other half of k-space. Though Hermitian symmetry dictates that only half of k-space is needed to reconstruct a real object, unwanted phase shifts cause the reconstructed object to be complex, and therefore, the additional k-space data (overscan data) can be used to overcome this problem. In practice, homodyne processing is used for partial Fourier image reconstruction. This processing technique uses low-spatial-frequency data from an image or reference scan (profile) to correct for phase errors produced by reconstruction of incomplete k-space data. Homodyne processing can also be performed in an iterative manner to account for rapidly varying phase.

One single-shot spin-echo technique that employs the partial Fourier imaging strategy is HASTE (half-Fourier single-shot turbo spin-echo) (104). As a means of acquiring reliable measures of compartmental relaxation in human imaging, development of a method for fast MSE imaging (using HASTE) would be beneficial. The extension to multi-slice imaging is important for clinical application, however, a rigorous evaluation of B_1 effects on T_2 estimation would first need to be performed. Furthermore, an accelerated method for accurate T_2 characterization would possibly allow for the translation of pre-clinical measurements, as implemented in the λ-carrageenan injury model, to practical clinical models of muscle disease.

CHAPTER 3

SPECIFIC AIMS

1. Validate DCE-MRI Measures in a Rat Glioma Model with Quantitative Dual-Isotope SPECT

Dynamic contrast enhanced MRI (DCE-MRI) can be used to assess tumor viability and vascular permeability. Physiologic measures of perfusion and extra-cellular volume can be obtained through quantitative analysis of DCE-MRI data. Tissue water and CA dynamics may influence these measures, and therefore affect estimates of these observable parameters. The range of extracellular volume fractions observed in tumor tissue, combined with the variety of available methods for modeling DCE data, presents a need for validation of these measures. A quantitative radiotracer imaging technique, in the form of dual-isotope SPECT imaging, may serve to validate the estimates of the extracellular volume fractions observed in DCE-MRI experiments in tumor tissue. This information may be helpful in refining current models or investigating new pharmacokinetic models with the goal of extracting relevant and accurate measures of compartmental characteristics in tumors.

2. Test a Contrast Enhanced T_2 Method for Measuring Compartmental Volume Fractions and Exchange in vivo

Two-pool models are often implemented in MR data analysis for the purpose of extracting compartmental tissue characteristics. Making accurate measures of these model parameters, however, can be difficult. In this study, the ability to measure water exchange *in vivo* and its effects on observed relaxation parameters will be evaluated in a graded muscle edema model

using a novel contrast enhanced technique. To measure compartmental exchange *in vivo* via model inversion, an estimate of at least one of the intrinsic parameters from the two-pool model must be known. In this work, the intrinsic extracellular volume fraction will be obtained by contrast enhanced T_2 measurements and subsequent modeling. This estimate will be compared to similar measures made with quantitative SPECT imaging, a method unbiased by compartmental water exchange. With these estimates, the two-pool exchange model will be inverted to extract intrinsic model parameters, including mean water lifetimes. These measures may be used to infer information about micro-anatomical changes that occur during muscle injury.

3. Test and Validate an Accelerated Method for Measuring Compartmental Relaxation

Robust methods of measuring compartmental relaxation have been implemented in single-slice imaging in small animal models. Translation of these methods to the clinic requires the addition of multi-slice coverage and reducing acquisition time. A modified partial Fourier single-shot spin-echo sequence will be implemented to obtain single and multi-slice measures of T_2 relaxation in phantoms and to evaluate the methods' sensitivity to variation in B_1. Validation of this method (T_2-HASTE) against a single-slice MSE sequence will be performed in a pre-clinical model of muscle edema, to evaluate characterization of multi-exponential T_2 with both linear and non-linear echo sampling. This method will also be explored as an alternate technique for fast and accurate multi-slice T_2 mapping.

CHAPTER 4

COMPARISON OF DYNAMIC CONTRAST ENHANCED MRI AND QUANTITATIVE SPECT IN A RAT GLIOMA MODEL

1. Abstract

Pharmacokinetic modeling of dynamic contrast enhanced (DCE)-MRI data provides measures of the extracellular volume fraction (v_e) and the volume transfer constant (K^{trans}) in a given tissue. These parameter estimates may be biased, however, by confounding issues such as contrast agent and tissue water dynamics, or assumptions of vascularization and perfusion made by the commonly used model. In contrast to MRI, radiotracer imaging with SPECT is insensitive to water dynamics. A quantitative dual-isotope SPECT technique was developed to obtain an estimate of v_e in a rat glioma model for comparison to the corresponding estimates obtained using DCE-MRI with a vascular input function (VIF) and reference region model (RR). Both DCE-MRI methods produced consistently larger estimates of v_e in comparison to the SPECT estimates, and several experimental sources were postulated to contribute to these differences.

2. Introduction

Dynamic contrast enhanced magnetic resonance imaging (DCE-MRI) is a technique often employed to characterize the microvascular environment in tumor tissues (63,105). This quantitative imaging technique provides a measure of the volume transfer constant (K^{trans}) and the volume fraction of extracellular-extravascular tissue space (v_e) via tracer kinetic modeling of MRI contrast agents (CA), typically Gd-DTPA. The most commonly used DCE

metric is K^{trans}, which reports on perfusion, but accurate measure of v_e may also be of clinical importance in assessing tumor type and response to treatment. For example, it has been shown that the relative size of v_e can help distinguish between gliomas, meningiomas, and metastases in brain tumors (63). The pharmacokinetic modeling necessary for DCE-MRI reduces a complex tissue micro-environment into a relatively simple compartmental model (21), which has known limitations (23,24,68,106). Also, parameter estimation is sensitive to the sometimes difficult to acquire vascular input function (VIF) (69,107,108) or the more easily acquired reference region (RR) signal (109,110). Given the array of potential sources of error in DCE-MRI, the interpretation of fitted model parameters as physical characteristics of tissue remains a question.

Conversion of signal intensity to CA concentration in a given tissue often assumes fast water exchange between the extracellular-extravascular space and the intracellular tissue space, however, there do exist models that account for compartmental water exchange (23,106). In certain tissues, increased levels of CA concentration may create an environment where ignoring water exchange across cell membranes leads to errors in the estimates of the model parameters. Also affecting the measure of the CA concentration is the extent to which the tissue is vascularized and perfused. For example, heterogeneous tumor tissue may be characterized by a well perfused proliferating rim and a poorly vascularized (possibly necrotic) core. The pattern of delayed enhancement observed in the core of these types of tumors may indicate CA diffusion from the periphery of the tumor. As with compartmental water exchange, tracer diffusion in tumor tissue has been found to be a source of error in the estimates of pharmacokinetic parameters, particularly in v_e, when using the Tofts model (24).

The previously described characteristics of DCE-MRI measurements and modeling reveal a need for further investigation and evaluation of the resulting pharmacokinetic parameters. One of the parameters, v_e, can be measured directly with single photon emission computed tomography (SPECT). To this end, a dual-isotope SPECT approach was developed and implemented on rats to obtain estimates of v_e that did not require dynamic tracer modeling, assumptions about water dynamics, or a VIF or RR signals. In an orthotopic rat glioma tumor model, these SPECT estimates of v_e were compared with estimates derived from DCE-MRI using both the VIF and RR approaches, with the objective of elucidating some of the sources of error in the DCE-MRI.

3. Methods

Female Sprague-Dawley rats (n=8, 234-270g) were anesthetized and inoculated with C6 glioma cells ($1x10^5$ cells) approximately two weeks prior to imaging. Two jugular catheters were placed in each rat, up to 24 hours before imaging. One catheter was used for CA injection while the other was used for blood sampling. Each rat was anesthetized using ≈ 2% isoflurane in oxygen for all surgical and imaging procedures. For MR imaging procedures body temperature was maintained near 37° C by a flow of warm air directed over the animal. Respiration was monitored using a pneumatic pillow placed on the side of the animal near the abdomen. Rats were imaged using a DCE-MRI protocol and were allowed to recover after the scan. Dual-isotope SPECT measurements were performed the following day, within 24 hours of the completion of the DCE-MRI measurements. Prior to SPECT, a bi-lateral nephrectomy was performed to prevent washout of the radiotracer, as was required for analysis of the SPECT data. The animal was anesthetized before the nephrectomy and

remained anesthetized throughout the duration of SPECT imaging. Upon completion of radionuclide imaging, the animals were sacrificed via an overdose of isoflurane. All procedures were approved by Vanderbilt University's institutional animal care and use committee.

3.1 DCE-MRI

MRI was performed on a 9.4T horizontal-bore magnet (Agilent, Santa Clara, CA). The animal's head was positioned in a 38 mm diameter Litz quadrature coil (Doty Scientific, Columbia, SC) and was secured by a bite bar apparatus that also served to deliver the anesthetic gas. Scout images were collected to identify a 2mm thick imaging slice through the center of the brain tumor and a second slice in the neck containing the major vessels feeding the brain.

Prior to DCE-MRI, an inversion-recovery snapshot experiment—TR = 12s, TI (inversion time) = 0.250-11s, NEX (number of excitations) = 2, 128 x 128 samples, 32 mm x 32 mm FOV—was used to generate data to produce a pre-contrast R_1 (longitudinal relaxation rate = $1/T_1$) map, R_{10}. A three parameter fit to these data was used to estimate R_1 in the presence of imperfect inversion. The DCE-MRI protocol employed a standard spoiled gradient-echo (SPGE) sequence—TR = 10ms, TE = 2.1ms, flip angle (α) = 15°, 96 x 96 samples, and NEX = 2—over the prescribed slices. Approximately 40 images were collected before a 200 μl bolus of Gd-DTPA (0.05 mmol/kg) was delivered over 5s via the jugular catheter. After injection of the contrast agent, dynamic images were collected for 20 minutes (~2s per image) and were reconstructed to 128 x 128 samples to match the spatial resolution of the R_{10} map. Following the completion of the DCE-MRI experiment, a 3D SPGE—TR =

20ms, TE = 2.1ms, α = 20°, 128 x 128 x 64 samples, 32 x 32 x 32 mm^3 slab—was acquired to provide a reference for image registration between MRI and SPECT images.

3.2 Bi-lateral Nephrectomy

Under anesthesia, two parallel incisions, one on each side, were made on the lower back of the rat. Using a swab, the kidneys were exposed and 3-0 silk sutures were slipped around each kidney and tightened around the renal pedicles, preventing clearance through the kidney. The kidneys were returned to their original position and the incisions were sutured shut. The total time for the procedure was approximately 20 minutes.

3.3 SPECT

Radionuclide imaging was performed on a NanoSPECT/CT (Bioscan, Washington DC, USA) with image reconstruction carried out using HiSPECT in the corresponding InVivoScope software. Under anesthesia, an extracellular radiotracer, ^{111}In-DTPA (~19 MBq), was injected first, followed by a saline flush, and allowed to equilibrate for approximately 30 minutes (longer than the known wash-in time for Gd-DTPA). An intravascular tracer, ^{99m}Tc-RBCs (Ultratag®) (~130 MBq), was then injected. After injection of the second tracer, images were collected (48 projections (helical SPECT), 40s per projection, reconstructed volume = 67 x 67 x 35 mm^3). Three energy windows (width=18%) were set about the ^{99m}Tc and ^{111}In photopeaks (140 keV and 171/245 keV, respectively), and projection data were recorded independently for each energy window using a 9-pinhole aperture collimator (pinhole diameter = 2.0 mm) on each of four detector heads. After collecting the brain images a blood sample (~500 μL) was obtained from the unused jugular

catheter and imaged with the previously described dual-isotope protocol. An X-ray CT scan was also collected for registration purposes (imaging dimensions same as SPECT). All SPECT images were reconstructed with 0.4 x 0.4 x 0.4 mm^3 voxels to match the CT image. To provide support for the use of the novel SPECT method *in vivo*, 5 different mixed isotope phantoms (500 µL each) were made with varying concentrations of ^{99m}Tc and ^{111}In corresponding to activity ratios (i.e. A_{99mTc} / A_{111In}) similar to those found in the blood samples. The phantoms were then imaged with the dual-isotope protocol and the activities were compared to those independently measured in a well counter. The resulting measurements can be seen in Figure 4.1.

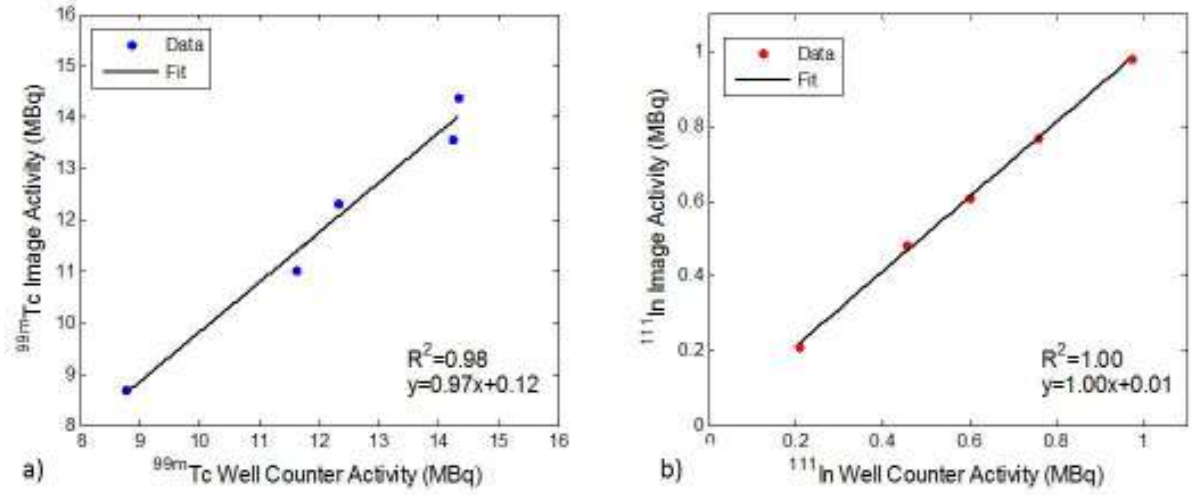

Fig. 4.1. Mixed isotope phantom validation for activity measurement with the dual-isotope protocol. a) ^{99m}Tc activity measures from the SPECT image and well counter. b) ^{111}In activity measures from the SPECT image and well counter. Linear regression analysis also shown.

4. Data Analysis

4.1 SPECT-MRI Registration

All MR and SPECT/CT imaging data were imported into MATLAB (Mathworks, Natick, MA) for processing. Prior to any quantitative analysis, the CT data were registered to the 3D SPGE data set using a rigid registration algorithm. All SPECT data were subsequently registered to the MR space as the SPECT images were implicitly co-registered to the CT scan. This process allowed co-registration of the single slice dynamic data (from the brain tumor) to the SPECT images.

4.2 DCE-MRI

The R_{10} map was used to identify a tumor region of interest (111) within which, R_1 tissue time course, $R_{1t}(t)$, was determined for each voxel using:

$$R_1(t) = \frac{1}{TR}\ln\left[\frac{S_0 \cdot \sin\alpha - S(t)\cdot\cos\alpha}{S_0 \cdot \sin\alpha - S(t)}\right], \qquad [4.1]$$

where S_0 was defined as

$$S_0 = S_{-} \cdot \left[\frac{1 - e^{-TR\cdot R_{10}} \cdot \cos\alpha}{(1 - e^{-TR\cdot R_{10}})\cdot \sin\alpha}\right]. \qquad [4.2]$$

S_{-} was the measured signal intensity, from the SPGE experiment, prior to contrast agent injection and $S(t)$ was the measured signal intensity at a time t after contrast injection. In addition to the tissue of interest (TOI), an ROI was also selected in the linguofacial artery in the neck of the rat to provide an image derived VIF. The VIF ROI contained signal from

approximately 5-10 voxels. Using the R_1 time course of the VIF, the concentration of CA in the plasma space (C_p) was determined using an assumption of fast water exchange across red blood cell membranes, therefore

$$C_p(t) = (R_{1b}(t) - R_{10b}) / r_1 \cdot (1 - h) \quad [4.3]$$

where the hematocrit (h) was 0.46, r_1 (the relaxivity of Gd-DTPA at 9.4T) was assumed to be 3.8 $mM^{-1}s^{-1}$ (111,112), and the pre-contrast R_1 of blood was assumed to be R_{10b} =0.435 s^{-1} (113-115).

K^{trans}, v_e, and v_p (plasma volume fraction) were estimated by fitting $C_p(t)$ and the dynamic R_1 time course from the tumor ROI, $R_{1t}(t)$, with Eqs. [4.4] and [4.5] (106):

$$R_{1t}(t) = R_{10t} + r_1 \cdot v_e \cdot C_t(t) \quad [4.4]$$

where

$$C_t(t) = K^{trans} \cdot \int_0^t C_p(T) \cdot \exp(-(K^{trans} / v_e) \cdot (t - T))dt + v_p C_p(t) \quad . \quad [4.5]$$

In these equations, $C_t(t)$ is the concentration of the CA in tumor tissue represented by the extended Tofts model (21). Subsequently, K^{trans} and v_e estimates from this VIF-based analysis are defined as K_{VIF}^{trans} and $v_{e,VIF}$, respectively. Non-linear fitting, here and below, used the default settings of the *lsqcurvefit* function in MATLAB R2011a (Natick, MA) with fitted parameters (K^{trans}, v_e and v_p) constrained to non-negative values.

In addition to the extended Tofts model analysis, the dynamic data were also analyzed on a voxel-by-voxel basis using a RR model (110). In the RR analysis, the reference tissue ROI was selected in the temporal muscle surrounding the skull. Two parameters, $K^{trans,t}$ and $v_{e,t}$, were then estimated by fitting the R_1 dynamic time course from each tumor voxel and the RR with

$$R_{1,t}(t) = R \times (R_{1,ref}(t) - R_{10,ref}) + R[(K^{trans,ref} / v_{e,ref}) - (K^{trans,t} / v_{e,t})] \times \int_0^t (R_{1,ref}(T) - R_{10,ref}) \cdot \exp((-K^{trans,t} / v_{e,t}) \times (t - T))dt + R_{10,t} \quad [4.6]$$

Where subscripts t and ref indicate tumor and reference regions, $R=K^{trans,t}/K^{trans,ref}$ and assumed $K^{trans,ref}$ = 0.05 min^{-1} and $v_{e,ref}$ = 0.11 were used for the reference tissue (69,110). Subsequently, in this paper, $K^{trans,t}$ and $v_{e,t}$ estimates from this RR-based analysis are defined as K_{RR}^{trans} and $v_{e,RR}$, respectively.

4.3 SPECT

Based on the dual-isotope SPECT protocol applied in this study of rat glioma, the resulting SPECT data was analyzed according to Eqs. [2.29]-[2.34] (as described in the background of this dissertation). The subscript 'tissue' in these equations refers to the individual voxels from a given tumor ROI in the present study. $v_{e,SP}$ was estimated voxel by voxel (where V_{tissue} in Eq. [2.34] was the known SPECT voxel volume) to create a parametric map for comparison to the DCE-MRI v_e estimates.

5. Results

Fig. 4.2a shows an example of the imaging slice used to visualize and select an ROI for the vascular input function. An example of a VIF from a single rat can be seen in Fig. 4.2b.

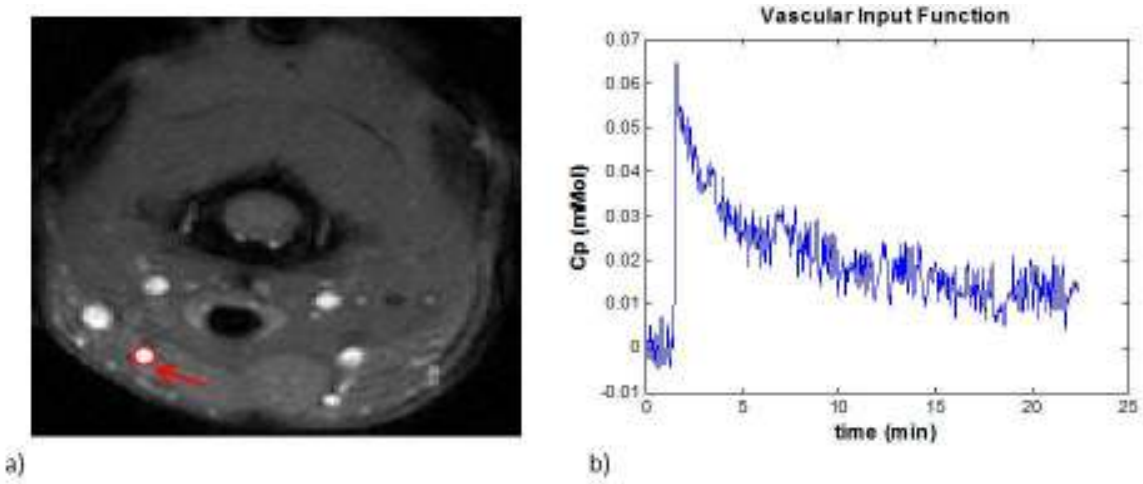

Fig. 4.2. a) Example of ROI placement for the VIF in the linguofacial artery. ROIs contained between 5 - 10 voxels. b) Example VIF time-course (in [CA]) recorded over an approximately 20 minute time period. Note the rapid rise and washout of the CA.

A tumor ROI was manually selected based on a pre-contrast T_1 map (Fig. 4.3a). An example dynamic R_1 time course from the tumor ROI along with the fit to the RR model are shown in Fig. 4.3b. The inset in Fig. 4.3b shows the R_1 time course for the reference tissue (skeletal muscle) used in the RR model fitting. All DCE-MRI fitting showed qualitatively good fits and quantitative estimates of parameter uncertainties that were much less than the spatial and inter-animal variations in model parameters. The slow rise of the tumor tissue R_1 time course indicates the need to collect data for at least 15 minutes post-injection to ensure a plateau has been reached.

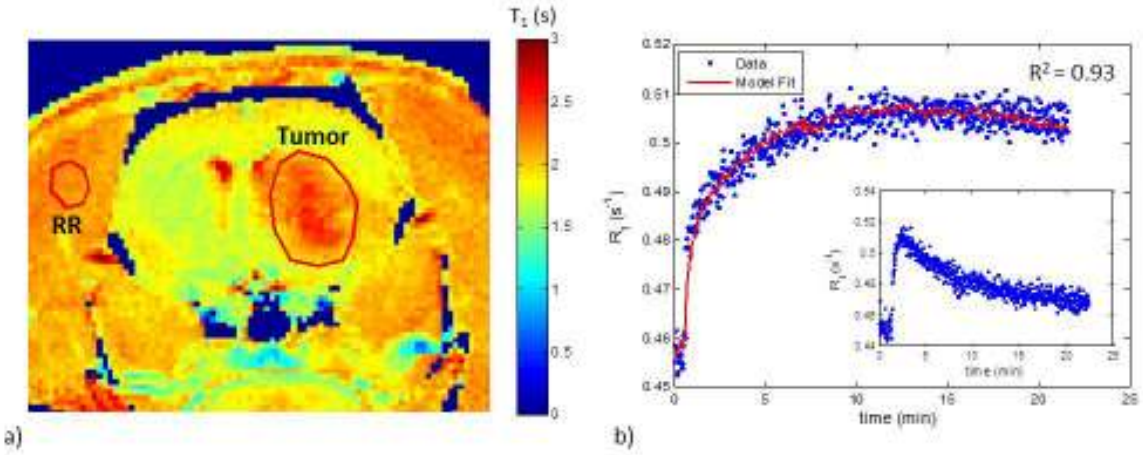

Fig. 4.3. a) An example T_{10} map showing the location of the manually defined brain tumor ROI and reference tissue ROI in the temporal muscle. Note the elevated T_1 times in the tumor region. b) Corresponding R_1 time course including RR model fit. The RR model shows a good fit to the dynamic data. The inset displays the dynamic time course of the reference tissue used for RR modeling.

Fig. 4.4 shows two examples (left and right) of the parametric maps from the RR model fitting and the dual-isotope SPECT analysis. On the left, the tumor appears more homogenously perfused (Fig. 4.4a) with moderate estimates of v_e (Fig. 4.4c, Fig. 4.4e). In contrast, the tumor in the right column exhibits a well perfused (K^{trans} > 0.06 min^{-1}) proliferating rim and a poorly perfused (K^{trans} < 0.02 min^{-1}) core, with more heterogeneous maps of v_e (Fig. 4.4d, Fig. 4.4f). In this case, although the color bar indicates a maximum $v_{e,RR}$ = 1, in the tumor core some voxels exhibited v_e > 1 (sometimes >> 1), indicating a breakdown of the model for accurately describing the DCE data. In order to avoid extreme outliers, only voxels exhibiting v_e < 2 and K^{trans} < 0.5 min^{-1} were included in subsequent analysis. This restriction resulted in discarding 2 - 30% (range, across animals) of tumor voxels from VIF analysis and 0.5 – 8% of tumor voxels from RR analysis.

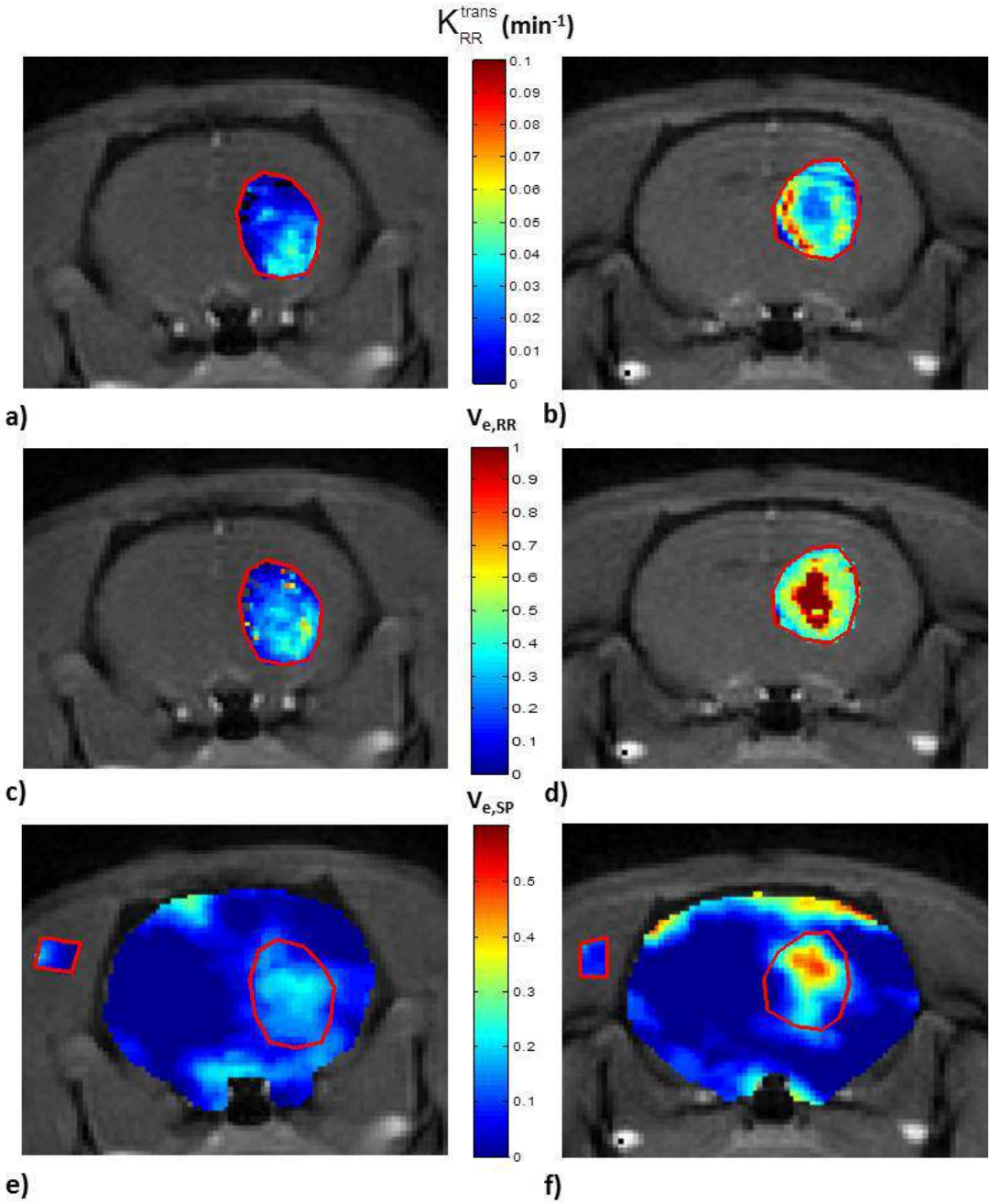

Fig. 4.4. Parametric maps from RR model fitting and co-registered SPECT/MR images for two different rats (one per column). (a,b) K_{RR}^{trans} maps, (c,d) $v_{e,RR}$ maps, and (e,f) $v_{e,SP}$ maps. Note the voxels in the center of the tumor (b,d) where K_{RR}^{trans} is low (< 0.02 min^{-1}) and $v_{e,RR}$ has been excluded due to non-physiological values (v_e > 1). The SPECT maps in e) and f) display the tumor ROI as well as a ROI in the muscle.

Figure 4.5 shows the tumor ROI mean (± SD) of estimates of v_e (top) and K^{trans} (bottom) from both DCE-MRI methods and SPECT (v_e only) for all eight animals. In general, the v_e values from the VIF analysis exceeded those of the RR analysis and both DCE-MRI analyses of v_e were higher than those found in the dual-isotope SPECT analysis (Fig. 4.5a). Computed voxel-by-voxel from the tumor ROIs in all eight animals, $v_{e,VIF} > v_{e,SP}$ (mean difference ± standard error = 0.57±0.01), and the difference was significant (t-test, $p<0.0001$) in all eight animals. Similarly, across all tumor ROI voxels, $v_{e,RR} > v_{e,SP}$ (0.14±0.005), and the difference was significant (t-test, $p<0.01$) in 7 of 8 animals. Comparing the DCE-MRI analysis techniques, $v_{e,VIF} > v_{e,RR}$ (0.43±0.008) in all eight animals, and again, the difference was significant (t-test, $p<0.0001$) in all eight animals.

Though there was no comparable measure for K^{trans} for the SPECT data, Fig. 4.5b shows a consistent overestimation across all eight animals where $K^{trans}_{VIF} > K^{trans}_{RR}$ (0.055±0.001). Also, although not shown in Fig. 4.5, a similar overestimation of blood volume fraction by VIF analysis of DCE-MRI (range across animals of mean = 0.04-0.18 and of SD = 0.03-0.15) compared with SPECT measures (range across animals of mean = 0.019-0.036 and of SD = 0.005-0.011) was found. Note, however, that constraining v_p to *a priori* values similar to those found by SPECT had little effect on the fitted values of v_e by DCE-MRI.

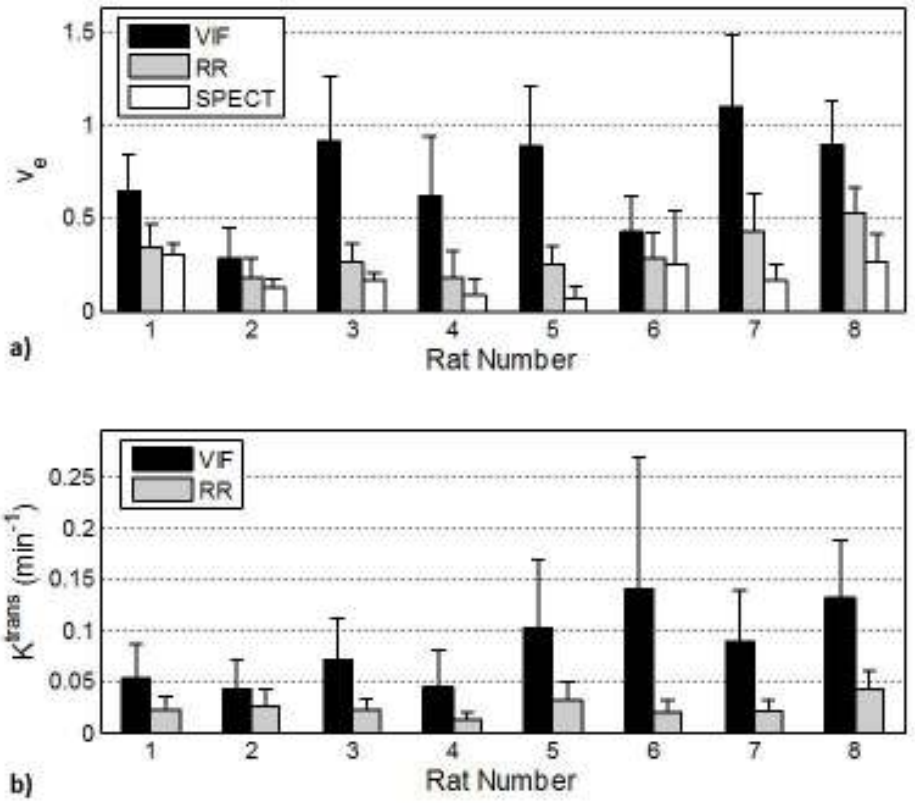

Fig. 4.5. a) Comparison of v_e for VIF, RR, and SPECT analysis for each animal studied. b) Comparison of K^{trans} for VIF and RR analysis. Solid bars represent mean values while error bars represent the standard deviations. Note that error bars are somewhat underestimated because outlier voxels exhibiting $v_e > 2$ or $K^{trans} > 0.5$ min^{-1} were not included in analysis.

6. Discussion

DCE-MRI measurements were made in an orthotopic rat glioma model that represents a more clinically relevant tumor location compared to xenograft studies. The results of this study revealed a consistent overestimation in the estimate of v_e from commonly used DCE-MRI analysis techniques when compared to v_e estimates from a novel quantitative SPECT technique. To our knowledge, this is the first account of an *in vivo* radionuclide measure of the extracellular-extravascular volume fraction. Previous measures of the extracellular tissue space using radionuclide techniques have been documented, however these measurements

were often made *ex vivo* via whole tissue gamma counting or autoradiography (17,82). While the radionuclide imaging used in this study is not practical for routine pre-clinical use because it involves surgical intervention to allow tracer equilibration, it is insensitive to water dynamics and does not require a vascular input function. Regarding surgical effects on parameter estimates, previous studies have shown no significant changes in plasma space and tissue water content of normal rat brain in the time, post-nephrectomy, in which the current measurements were recorded (116,117)

Phantom tests (see Figure 4.1) demonstrated the accuracy of this dual-energy SPECT method for measuring concentrations of ^{99m}Tc-RBCs and ^{111}In-DTPA. In addition, $v_{e,SP}$ in muscle was found to be 0.10±0.04 (mean ± standard deviation (SD)) over the animals studied, which is in agreement with v_e of muscle observed in previous MR measurements (82,118). Furthermore, the blood volume fraction (v_b) from the SPECT measurements in tumor (0.03 ± 0.01) was found to be within the range of values observed in a recent study of rat glioma by Li *et al* (119) as well as a study examining various grades of human gliomas (63). Thus, although no independent validation of the *in vivo* SPECT measurements from tumor have been made, we interpret the observed differences in SPECT and MRI measures of v_e (Fig. 4.4) to predominantly reflect an overestimation of v_e from DCE-MRI.

The explanation for why DCE-MRI overestimated v_e is not entirely clear, but it is apparent that DCE-MRI analysis using a VIF resulted in a much greater overestimation than did the RR analysis. Estimates of v_e in rat tumor using VIF analyses have been found to span a large range with individual voxel values sometimes exceeding 1(119-121). For example, McIntyre et al found that, depending on the use of a measured or literature-based VIF, up to 48% of voxels in rat tumor exhibited v_e >1(120). Averaging of the vascular signal over space

with non-vascular signal or over time during the peak of the VIF will result in a diminished VIF and, in turn, an increased estimate of v_e (69,70). However, in this study, the VIF was acquired at relatively high spatial and temporal resolutions, so these factors are unlikely to explain the differences between $v_{e,VIF}$ and $v_{e,RR}$. The VIF amplitude may also be reduced by T_2^* effects, however a relatively low concentration of Gd-DTPA (0.05 mmol/kg) was administered to mitigate T_2^* dropout expected at high B_0. In addition, calculations show < 1 % signal reduction due to T_2^* with the imaging parameters used in this study. A third potential source of error in the VIF is due to the inflow effect on the T_1-weighting image contrast, which has been studied in detail recently (122,123).

Inflowing blood which did not experience the previous RF excitation pulses is not T_1-weighted and results in an overestimation of S_0 (Eq. [4.2]) and an underestimation of the change in $S(t)$ (Eq. [4.1]). Both of these factors diminish the VIF and, in turn, result in an overestimation of v_e. In the context of the present study, an arterial blood velocity of 5 cm/s (124) dictates that ≈¼ of the blood in a 2 mm imaging slice is replaced with inflowing blood every TR (10 ms). Crudely then, one can consider the blood signal to be 75% from magnetization at steady state and 25% from magnetization at equilibrium. Then, given $R_{10b} = 0.435\ s^{-1}$ and $\alpha = 15°$, Eq. [4.2] will overestimate $S_{0,blood}$ by ≈3× and, for a peak C_p ~0.2 mM, the net effect is to overestimate v_e by ≈2×. This model of inflow agrees well with the observations (not shown) that $S_{0,blood} \approx 3 \times S_{0,muscle}$ and roughly with the observations of $v_{e,VIF}$ compared with $v_{e,RR}$ (Fig. 4.5), thereby suggesting that inflow is the dominant source of discrepancy between the VIF and RR results in this study.

To minimize inflow effects, previous studies using VIF-based analyses have employed saturation pulses (121) and amplitude correction of the VIF based on reference

tissues (119,125). A similar method may be applied using an inflow-insensitive estimate of $S_{0,blood}$ (such as one based on $S_{0,muscle}$) in Eq. [4.1] to partially correct the previously described problem. The use of selectively-spoiled composite RF pulses (126) or 3D DCE methods might also be helpful. Relatively few quantitative 3D DCE-MRI tumor studies have been made in rodents (127-129) and, though this method might provide an alternative for minimizing flow effects, temporal sampling requirements would need to be met as to not further bias estimates of K^{trans} and v_e (130). Alternatively, the reference region method can be used to avoid the VIF altogether.

This work reveals some of the confounding issues in performing small-animal DCE-MRI studies in brain tumors while attempting to obtain an image-derived input function in the same scan. A few studies have demonstrated the ability to obtain an input function while imaging the rat brain, though they require a multi-coil setup or automated input function extraction from a small number of pixels in the sagittal sinus (119,121). For this reason, methods such as RR analysis have become popular in the analysis of DCE data. The reference region analysis provided values of $v_{e,RR}$ that were closer to but still consistently larger than $v_{e,SP}$ (Fig. 4.5). The DCE model used in this study assumed fast exchange of water between intra- and extra-cellular tissue spaces, which may not be a valid assumption, particularly with the introduction of extra-cellular contrast agent (23). The relatively low dose of CA administered in this study, however, serves to decrease the effects of water exchange due to CA distribution. In the case where fast exchange is not valid, however, the effect on the DCE analysis is to underestimate not overestimate v_e, so while water exchange may be affecting the DCE analysis it does not explain the observations here.

In addition to water dynamics, CA dynamics may also affect parameter accuracy. In a recent study by Pellerin *et al*., it was postulated that, in tumors CA diffuses from well-vascularized regions to adjacent poorly perfused regions over the time-course of a DCE experiment (24). To account for the amount of CA that reaches the necrotic or poorly perfused tissues and the slow uptake of those voxels, the Tofts model has to assign very low (non-zero) K^{trans} values and overestimates of v_e (24,131). Pellerin observed values of v_e, in a mouse tumor xenograft, that were up to two times greater than those values recorded with a pharmacokinetic model incorporating diffusion. Based on this observation, this diffusion effect could be contributing to overestimates of $v_{e,RR}$, as seen in this study (Fig. 4.4 and Fig. 4.6).

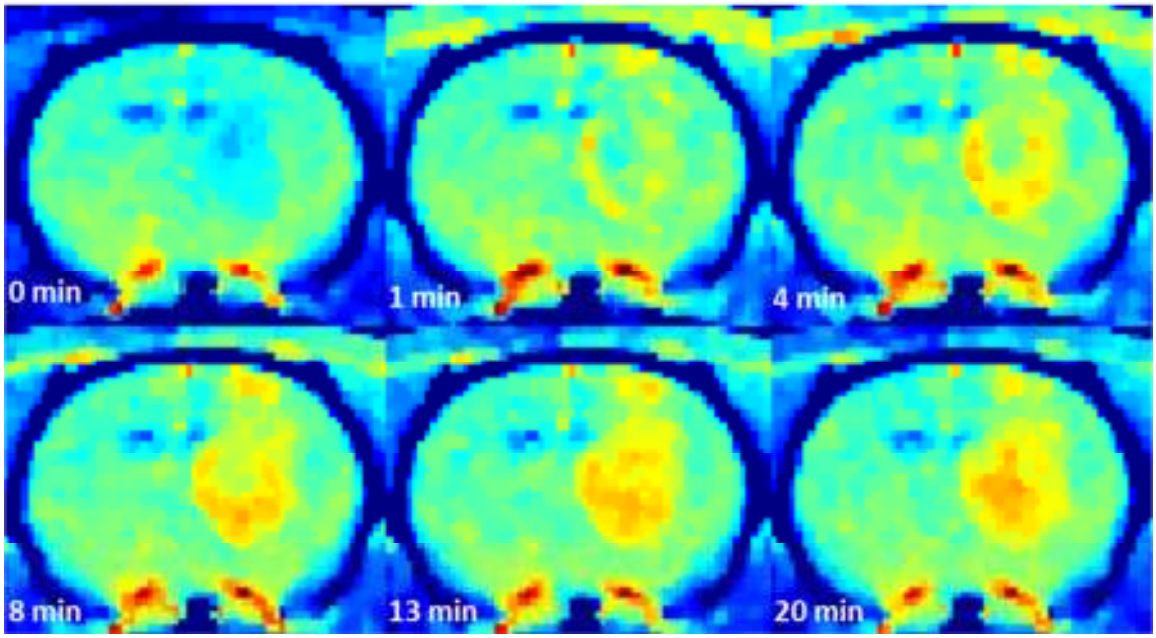

Fig. 4.6. Example DCE-MRI (signal intensity) images showing suspected CA diffusion in rat glioma. Note the fast enhancing regions near the rim of the tumor and the slow enhancing core. At the end of the dynamic acquisition (20 min) the CA accumulation in the core has become elevated compared to the rim.

The central tumor voxels of rats 7 and 8 exhibited a large $v_{e,SP}$ (e.g., Fig 4.4f) perhaps indicating a necrotic core, and the DCE analysis showed low K^{trans} and $v_{e,RR} > 1$ from the same voxels. (Of course, slow arrival of ^{111}In-DTPA to necrotic regions could also result in a reduced value of $v_{e,SP}$, although more time was allowed for tracer distribution in the SPECT studies.) In an earlier study by Donahue *et al*. it was stated that in cases of necrosis where the value of v_e becomes quite large, the time required for interstitial CA diffusion and uniform distribution may become significant (82). In these cases, measurement of the cell volume fractions may not be possible because a peak in the dynamic time course may not be discernible. Also, Sourbron and Buckley recently demonstrated that DCE analysis with the Tofts model is sensitive to variations in vascularization and perfusion, independent of CA diffusion between voxels (68). Impulse response functions were generated based on a two-compartment exchange model under a number of boundary conditions dealing with perfusion, vascularization, and rate of tracer exchange. The general form of the impulse response functions from the Tofts model and extended Tofts model were then used to determine under what conditions they were valid. Their analysis shows that in intermediate-to-highly vascularized tissues or tissues that are poorly perfused, v_e may be overestimated by DCE-MRI, which may explain the observations here of $v_{e,RR} > v_{e,SP}$ in non-necrotic tumor regions.

Obtaining an accurate measure of v_e may ultimately be of clinical importance in assessing tumor type and response to treatment. The interpretation that DCE-MRI is often overestimating v_e might also explain previous studies that have found, surprisingly, only weak to moderate correlations between v_e and the apparent diffusion coefficient (ADC) of water (132-134). While DCE-MRI measures of v_e in tumors has been found to shrink in response to treatment (135,136), water ADC has been shown to *increase* in response to

treatment (136). Perhaps this apparent inconsistency reflects a change in the state of tumor vascularization or perfusion with treatment that results in a more accurate measure of v_e. In this case, the observed v_e from DCE-MRI may go down in response to treatment simply because it is less overestimated, while in fact the extracellular volume fraction goes up, resulting in an increased water ADC. Though this is just one scenario, it does suggest that some of the commonly implemented pharmacokinetic models do not provide the entire picture.

As both pre-clinical and human DCE-MRI studies become more prevalent, and the technique is further incorporated into the clinic, the need arises to re-evaluate the accuracy and interpretation of the commonly reported model parameters. This is particularly important in tumor studies where the level of tissue heterogeneity and microcirculation varies between subjects. In this case a voxel-by-voxel analysis may be more appropriate than an ROI approach, as the tumor may contain regions where the Tofts model reports inaccurate estimates of model parameters. Regardless of the exact source of error in measures of v_e, the wide range of v_e values observed in this study indicates that one should be cautious about an absolute quantitative, physical interpretation of v_e.

7. Conclusion

This study showed an overestimation in v_e from DCE-MRI tumor data when compared to a measure of v_e from *in vivo* quantitative radionuclide imaging. A quantitative dual-isotope SPECT technique provided an independent measure of the extracellular-extravascular space unbiased by water exchange or errors in the VIF. It was postulated that the overestimation of $v_{e,RR}$ could be due in part to contrast agent diffusion effects from necrotic or poorly perfused

tumor tissue or to inappropriate application of the Tofts models. This study provides evidence that commonly used DCE-MRI analysis techniques might not be applicable in certain tissue types and the physical interpretation of the parameters, specifically v_e, are up for discussion.

CHAPTER 5

EXCHANGE-RESOLVED COMPARTMENTAL NMR MEASUREMENTS IN A GRADED MUSCLE EDEMA MODEL

1. Abstract

Two compartment models are widely used to describe NMR relaxation in tissue and typically involve an assumption of either fast or slow inter-compartmental water exchange rates. In many cases, however, inter-compartmental water exchange is intermediate and significantly alters the observed ^{1}H relaxation. For example, previous studies of injured muscle have shown two T_2 relaxation components, which have been attributed to intra- and extra-cellular water under the assumption of slow water exchange. Without this assumption, inverting the two-pool model of relaxation requires at least one of the intrinsic model parameters. In this work a simple method was developed wherein compartmental measures of T_2 were obtained, in injured rat skeletal muscle, with and without a compartment-specific contrast agent to provide knowledge of the intrinsic measure of the extracellular volume fraction. A similar unbiased estimate from quantitative SPECT imaging was compared to the intrinsic value from MRI and was found to have a higher correlation than with the observed MR estimates. Subsequent model inversion on a voxel-by-voxel basis allowed the calculation of parametric maps, including the intracellular water lifetime, which may reveal important information about muscle cell permeability during states of injury.

2. Introduction

Compartmental models are widely used to describe MRI contrast in tissue and quantitative measurements of transverse or longitudinal water proton relaxation are often used to experimentally characterize such models. Most compartmental analyses of ^{1}H NMR relaxation require an assumption about the rate of inter-compartmental water exchange in comparison to the relaxation rates. That is, most studies assume either the fast exchange limit (FXL) (the rate of water exchange is fast enough to result in a single observable relaxation rate) or the slow exchange limit (SXL) (the rate of water exchange is slow enough that the total signal can be treated as the sum of signals from independent compartments). However, in many cases, neither assumption is valid and the effect of inter-compartmental water exchange on the observed signal significantly alters the compartmental interpretation.

Previous approaches to measure the rate of inter-compartmental water exchange have largely been limited to *ex vivo* or non-biological samples where acquisition time is not a limiting factor (19,51,52). Landis et al. estimated transcytolemmal water exchange rates *in vivo* in normal rat skeletal muscle using a series of T_1 measurements of muscle and blood samples, acquired during steady state conditions of Gd-DTPA intravenous infusion over a range of stepped contrast agent concentrations (17). Though this was a careful and detailed study the approach used precludes translation to clinical or even routine pre-clinical imaging. Subsequently, an experimentally simpler approach demonstrated that dynamic T_1 weighted MRI following a single injection of contrast agent can provide estimates of compartmental pharmacokinetic parameters, including transcytolemmal water exchange rates (106). Both of these methods, however, are predicated on the assumption of fast water exchange prior to contrast agent injection, and only small deviations from the FXL following contrast injection. In some tissues, such as injured skeletal muscle, where both transverse and longitudinal

relaxation have been observed to be bi-exponential in the absence of contrast (14-16), another strategy is needed.

In previous studies of both normal and injured muscle, multi-exponential relaxation has been observed *in vivo* (9,13-15,92,102) and the volume fraction of the long-lived signal component has been shown to increase with injury and inflammation (14,15,92). These studies made the assignment of a long-lived and short-lived signal component to extracellular and intracellular water, respectively, based on the assumption of slow inter-compartmental water exchange. Such quantitative studies offer promise for greater specificity in the evaluation of muscle injury and disease progression, but a more comprehensive model of the MR signal in such tissues requires an understanding of compartmental water dynamics. A complete two-pool model of muscle injury would ultimately provide quantitative measures of edema and myofiber volume fractions, relaxation rates, and myofiber-specific measures of the apparent diffusion coefficient (ADC) of water. The water exchange rate itself may be useful in probing changes in myofiber caliber and/or sarcolemma permeability.

Presented here is a simple experimental method for acquiring exchange-resolved measures of the extracellular volume fraction for the purpose of inverting a two-pool model with water exchange. This method is applicable to tissues that exhibit bi-exponential relaxation where relaxation in one tissue compartment can be altered using a contrast agent. Note that this method requires neither a measure of a vascular input function nor calibration of contrast agent concentration or relaxivity. This method is demonstrated in a rat model of skeletal muscle edema and is evaluated in comparison to extracellular volume fractions obtained from radionuclide imaging.

3. Theory

Consider a two-compartment model of water protons, similar to Fig. 2.2. Each compartment is characterized by fractional proton content (f_a and f_b), relaxation rates (R_a and R_b), and water residence time constants (τ_a and τ_b). At equilibrium, detailed balance dictates that $\tau_a/f_a = \tau_b/f_b$ and $f_a = 1\text{-}f_b$, resulting in four independent model parameters: τ_a, f_b, R_a, and R_b. In general, the relaxation rates can represent longitudinal or transverse relaxation rates, but in the context of this study they are transverse relaxation rates. Likewise, in the context of skeletal muscle, we can arbitrarily assign compartment *b* to the extracellular tissue space and assume that $R_a > R_b$. The choice of using relaxation rates or time constants is arbitrary: relaxation rates can be equivalently expressed as time constants ($T_a = 1/R_a$ and $T_b = 1/R_b$) and the residence time constants can be expressed as exchange rate constants ($k_{ab} = 1/\tau_a$ and $k_{ba} = 1/\tau_b$).

The transverse magnetization signal, *S(t)*, from this model is described by a bi-exponential function,

$$S(t) = S_0((1 - f_b')e^{(-t \cdot R'_a)} + f_b'e^{(-t \cdot R'_b)}) \qquad [5.1]$$

where the ' superscript distinguishes the apparent signal fractions and rate constants from the intrinsic model parameters defined above. In the SXL the apparent and intrinsic parameters are equal. When the effect of water exchange is included, the apparent relaxation rates and signal fractions are related to the intrinsic rates and residence times by Eqs. [2.13]-[2.16] (49). However, the mean relaxation rate, R_m, is independent of water exchange, so

$$R_m = (1 - f_b') \cdot R_a' + f_b' R_b' = (1 - f_b) \cdot R_a + f_b R_b \quad [5.2]$$

If a CA is introduced into compartment *b*, then R_b becomes a function of CA concentration ([CA]),

$$R_{b+} = R_b + r_b[CA] \quad , \quad [5.3]$$

where r_b is the relaxivity of the CA in compartment *b*, and $_+$ indicates a measurement with CA. Given two measurements, before and after the introduction of CA, and Eq. [5.2] and [5.3], the following equations can be derived

$$\begin{aligned} \Delta R_m &= R_{m+} - R_m = (1 - f_{b+}') \cdot R_{a+}' + f_{b+}' R_{b+}' - (1 - f_b') \cdot R_a' - f_b' R_b' \\ &= (1 - f_{b+}) \cdot R_{a+} + f_{b+} R_{b+} - (1 - f_b) \cdot R_a - f_b R_b \\ &= f_b (R_b + r_b[CA]) - f_b R_b \\ &= f_b r_b[CA] \end{aligned} \quad [5.4]$$

and, similarly

$$\Delta R_s = R_{a+}' + R_{b+}' - R_a' - R_b' = r_b[CA], \quad [5.5]$$

where ΔR_m is the difference in the mean relaxation rate resulting from CA introduction, and ΔR_s is the difference in the sum of observed relaxation rates. In Eq. [5.5] the observed rates are equal to Eq. [2.13] and [2.14], where R_b is replaced with R_{b+} from Eq. [5.3] for the post-contrast measurements. Combining Eq. [5.4] and Eq. [5.5] yields the intrinsic volume fractions of compartment *b* as

$$f_b = \Delta R_m / \Delta R_s \quad . \qquad [5.6]$$

If the signal, *S(t)*, can be measured with sufficient precision and accuracy, then it can be fit to the right side of Eq. [5.1] to estimate S_0, f_b', R_a', and R_b'; likewise for $S_+(t)$ and the corresponding post-contrast parameters. These 6 values can then be used in Eq. [5.4]-[5.6] to estimate f_b, the intrinsic proton fraction of compartment *b*. The three remaining intrinsic model parameters τ_a, R_a, and R_b, may be numerically determined from Eqs [2.13]-[2.15].

4. Methods

4. 1 Animal Preparation

Female Sprague-Dawley rats (n=8,mean=235g) were used for the outlined experiments per animal protocols approved by the Institutional Animal Care and Use Committee (IACUC) at Vanderbilt University. The day prior to imaging, rats were anesthetized with isoflurane (Forane, Baxter Healthcare Corporation) and two jugular catheters were placed, one for contrast injections and one for blood sampling. The next morning, edema was induced under anesthesia using a 0.1 mL subcutaneous injection of λ-carrageenan (Sigma Aldrich) saline solution (0.125%, 0.25%, 0.5%, or 1.0% w/v) in the right hindlimb below the knee. Post-injection, the animals were allowed to recover for 6-8 hours to allow intra-muscular edema to form and reach a plateau state (98). Rats were then re-anesthetized for imaging. First, MRI studies were undertaken, during which body temperature was maintained near 37° C by warm air flow and respiration was monitored using a pneumatic pillow. Following MRI

studies, while still anesthetized, a bi-lateral nephrectomy was performed, and then the animal was immediately studied with single photon emission computed tomography (SPECT).

4.2 MRI

Imaging was performed on a 9.4T horizontal-bore magnet (Agilent Inc, Santa Clara, CA). Both of the rats' legs were secured together and positioned into a 38 mm diameter Litz quadrature coil (Doty Scientific, Columbia, SC) for RF transmission and reception. A T_2-weighted multi-slice fast spin-echo (FSE) sequence was used to locate regions of edematous muscle and plan a 2 mm thick axial slice. Single-slice multiple spin-echo (MSE) measurements were made prior to and approximately 20 minutes following an i.v. injection of Gd-DTPA (200μL, 0.4 mmol/kg). Between MSE measurements, the wash-in and gradual wash-out of the contrast agent was monitored by repeated T_1-weighted spoiled gradient-echo (SPGE) images. Following the second MSE measurement, a 3D SPGE image set ($35mm^3$, 128 x 128 x 64 samples) was collected for registration purposes.

The MSE imaging sequence (similar to Fig. 2.3) included a total of 36 spin echoes with TE = 10ms for the first 30 echoes and TE_{late} = 50ms for the remaining 6 echoes. Radiofrequency refocusing was achieved with a 300μs $90°_x$-$180°_y$-$90°_x$ composite pulse surrounded by a pair of amplitude-modulated crusher gradients to remove unwanted magnetization (34). Images were encoded with 64 x 64 samples over a 35 x 35 mm^2 field of view (FOV) and were reconstructed to 128 x 128 samples. A long repetition time (TR = 15s) was used to avoid bias of signal amplitudes from T_1-weighting. Two excitations were averaged (NEX=2) resulting in a time of approximately 80 minutes for the entire contrast enhanced experiment.

4.3 Bi-lateral Nephrectomy

With the rat still anesthetized, two parallel incisions, one on each side, were made on the lower back of the rat. Using a swab, the kidneys were exposed and 3-0 silk sutures were slipped around each kidney and tied around the renal pedicles, thereby preventing clearance through the kidney. The kidneys were returned to their original position and the incisions were sutured shut. The total time for the procedure was approximately 20 minutes.

4.4 SPECT

Radionuclide imaging was performed on a NanoSPECT/CT console (Bioscan, Washington DC, USA) with image reconstruction carried out using the corresponding InVivoScope software. Prior to imaging, the system image intensity was calibrated to measures of activity as described in Chapter 2 of this dissertation. For *in vivo* imaging, an extracellular radiotracer, ^{111}In-DTPA (≈37 MBq, 200 μL), was injected into the rat's first jugular catheter, followed by a saline flush, and then allowed to equilibrate for approximately 25 minutes. Images of the hindlimb were then collected (24 projections, 40s per projection, 67 x 67 x 35 mm^3). A CT scan was also collected for registration purposes (imaging dimensions same as SPECT). All CT/SPECT images were reconstructed to 0.4^3 mm^3 voxel size. After imaging, a blood sample (≈500 μL) was drawn from the second jugular catheter, centrifuged to produce a plasma sample of volume V_{plasma}, and placed in a well counter to measure activity, A_{plasma}.

5. Data Analysis

5.1 MRI

For each animal, the MSE data, pre- and post-contrast, were analyzed on a voxel-by-voxel basis. For a given voxel, the MSE signal decay was fit to a sum of decaying exponentials in a NNLS manner (see Chapter 2 Eq. [2.9]-[2.11]), resulting in a T_2 spectrum (47). The T_2 spectra were then used to distinguish voxels that were characterized by multi-exponential T_2 relaxation. All voxels displaying more than one signal component were used in subsequent analysis. The signal data from these corresponding voxels were then fit, unconstrained, to Eq. [5.1] using *lsqnonlin* in MATLAB. The resulting observed parameter values, pre- and post-contrast, were used to calculate f_b via Eq. [5.4]-[5.6]. Voxels that exhibited $0 < f_b < 1$, were then included in the inversion of the two pool model with exchange. For model inversion, the calculated value of f_b and the observed parameter values (f_b', R_{2a}', R_{2b}') for each voxel were fit to Eq. [2.10]-[2.12] with detailed balance using *lsqnonlin*, where $0 < T_{2a} < 50$ms, $0 < T_{2b} < 500$ms, and $\tau_a > 0$ were set as constraints. The intrinsic model parameters (f_b, R_{2a}, R_{2b}, τ_a) for each applicable voxel were extracted such that parametric maps could be constructed. For the purpose of this study, f_b (and f_b') was defined as v_e (and v_e') to emphasize the physiological assignment to the extracellular-extravascular space.

In addition, an ROI analysis was performed in regions manually selected in edematous muscle based on the v_e' and v_e parametric maps. Areas of subcutaneous fat and inter-muscle edema were avoided. For each ROI, the median and variance of v_e' and v_e were extracted from the parametric maps (where $v_e > 0$). ROI based values of v_e' and v_e were also calculated via fitting of the cumulative signal from an ROI in the MSE data to Eq. [5.1], with subsequent computation of v_e via Eq. [5.4]-[5.6].

5.2 SPECT

All MRI and SPECT/CT imaging data were imported into MATLAB (Natick, MA) for processing. Prior to any quantitative analysis, the CT data were registered to the 3D SPGE data set using a rigid registration algorithm. The SPECT data, which were implicitly co-registered to the CT data, were then mapped to MRI space using the same transformation. This process allowed co-registration of the single slice data (from the hindlimb) to the SPECT images. The resulting SPECT data was analyzed according to Eqs. [2.26]-[2.28] (as described in Chapter 2). The subscript 'EC' in these equations refers to the extracellular space of individual voxels in muscle. $v_{e,SP}$ was estimated on a voxel-by-voxel basis, where V_{tissue} (in Eq. [2.28]) was the known volume of a reconstructed voxel in the SPECT experiment. As a result, a parametric map was created for comparison (via ROI analysis) to the MR estimates of v_e and v_e'.

6. Results

Fig. 5.1 shows a co-registered SPECT-MR image (Fig. 5.1a) and example contrast enhancement curves (Fig. 5.1b) created from dynamic SPGE measurements in an ROI in normal and edematous muscle. Areas of edema on the MSE image correspond well with the overlaying areas of increased activity on the SPECT image. The contrast enhancement curve for edematous muscle reached a peak at ~15 minutes post-injection, indicating a point of equilibrium where the CA had distributed throughout the extracellular volume. In comparison to the contrast enhancement curve for normal muscle, which reached a plateau in ~2 min, this delayed and increased enhancement in the edematous muscle is consistent with

observations from DCE-MRI studies of tissues with larger extracellular volume fractions (106,110).

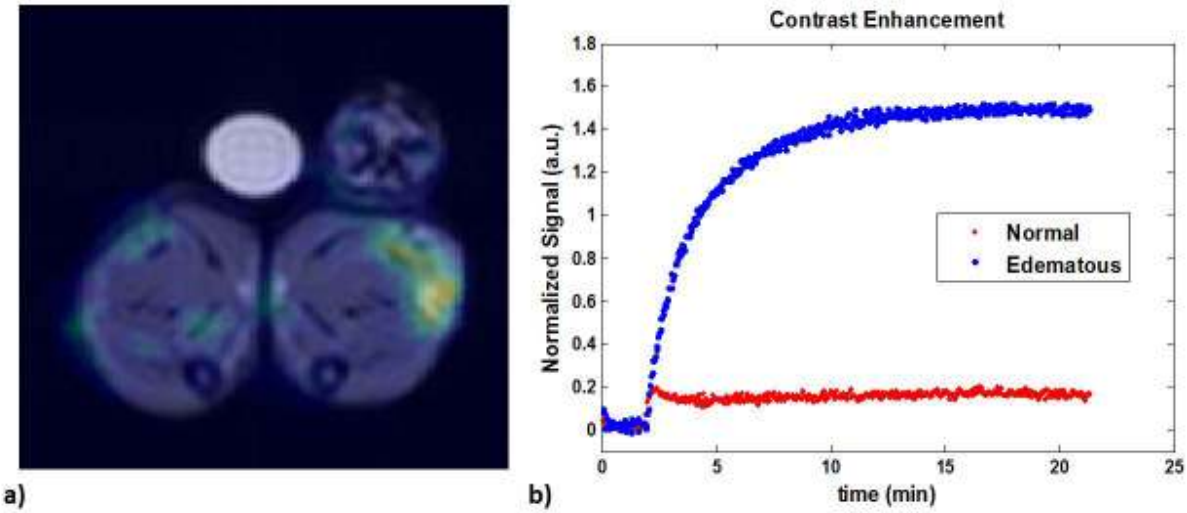

Fig. 5.1. a) Example co-registered SPECT-MR image. b) Normalized contrast enhanced curves for normal and edematous muscle after Gd-DTPA administration.

Fig. 5.2 shows example signal decay curves and corresponding T_2 spectra, both before and after contrast enhancement, from voxels containing normal (Fig. 5.2a,b) and edematous muscle (Fig. 5.2c,d). On the whole, most voxels from normal muscle tissue regions exhibited mono-exponential T_2 with little or no change in T_2 after contrast enhancement, as indicated in Fig. 5.2a and 5.2b. Voxels from edematous muscle regions, however, exhibited predominantly bi-exponential relaxation with a shift in the long-lived signal component towards a shorter T_2 with the addition of CA. Bi-exponential fits to the edematous muscle decay data (Fig. 5.2c) showed good agreement at the voxel level with reduced χ^2 values near 1. Correspondingly, the typical SNR in a given voxel from these measurements ranged from 550-1050.

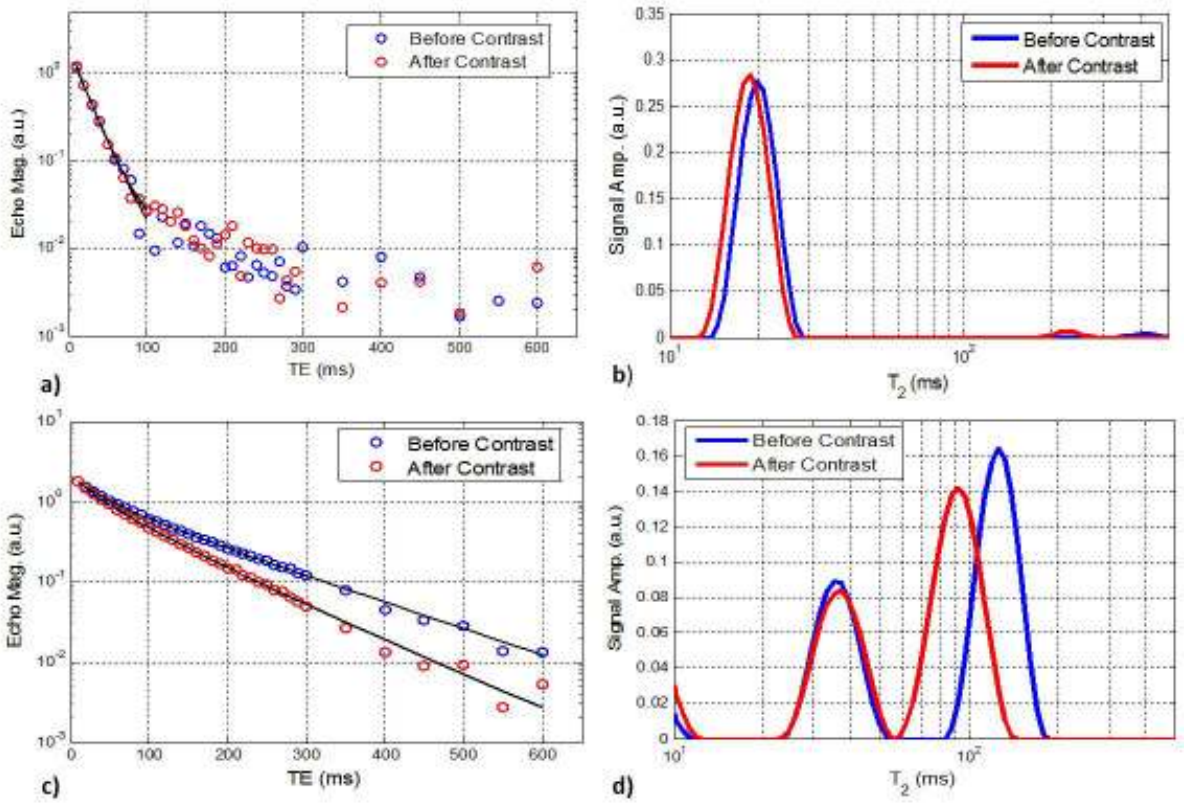

Fig. 5.2. a) T_2 decay curves and associated fits for a voxel containing normal muscle both pre- and post-contrast and b) the corresponding T_2 spectra. c) T_2 decay curves and associated bi-exponential fits for a voxel containing edematous muscle both pre- and post-contrast and d) the corresponding T_2 spectra.

Examples of the parametric maps from the voxel-by-voxel analysis and subsequent two-pool model inversion can be seen in Fig. 5.3 and Fig. 5.4. Fig. 5.3 shows an example where the present method does a good job of characterizing the edematous tissue. All voxels included in the maps in Fig. 5.3a and 5.3c exhibited multi-exponential T_2, with no exclusion due to non-physiological values of v_e (i.e. some voxels displayed in Fig. 5.3a and 5.3c exhibit $v_e > 1$). Alternately, the parametric maps in Fig. 5.3b, 5.3d, and 5.3f were threshold to only include voxels with physiologically relevant parameter values: $0 < v_e < 1$ and $0 < \tau_a < 2$s. The corresponding $v_{e,SP}$ map can be seen in Fig. 5.3e.

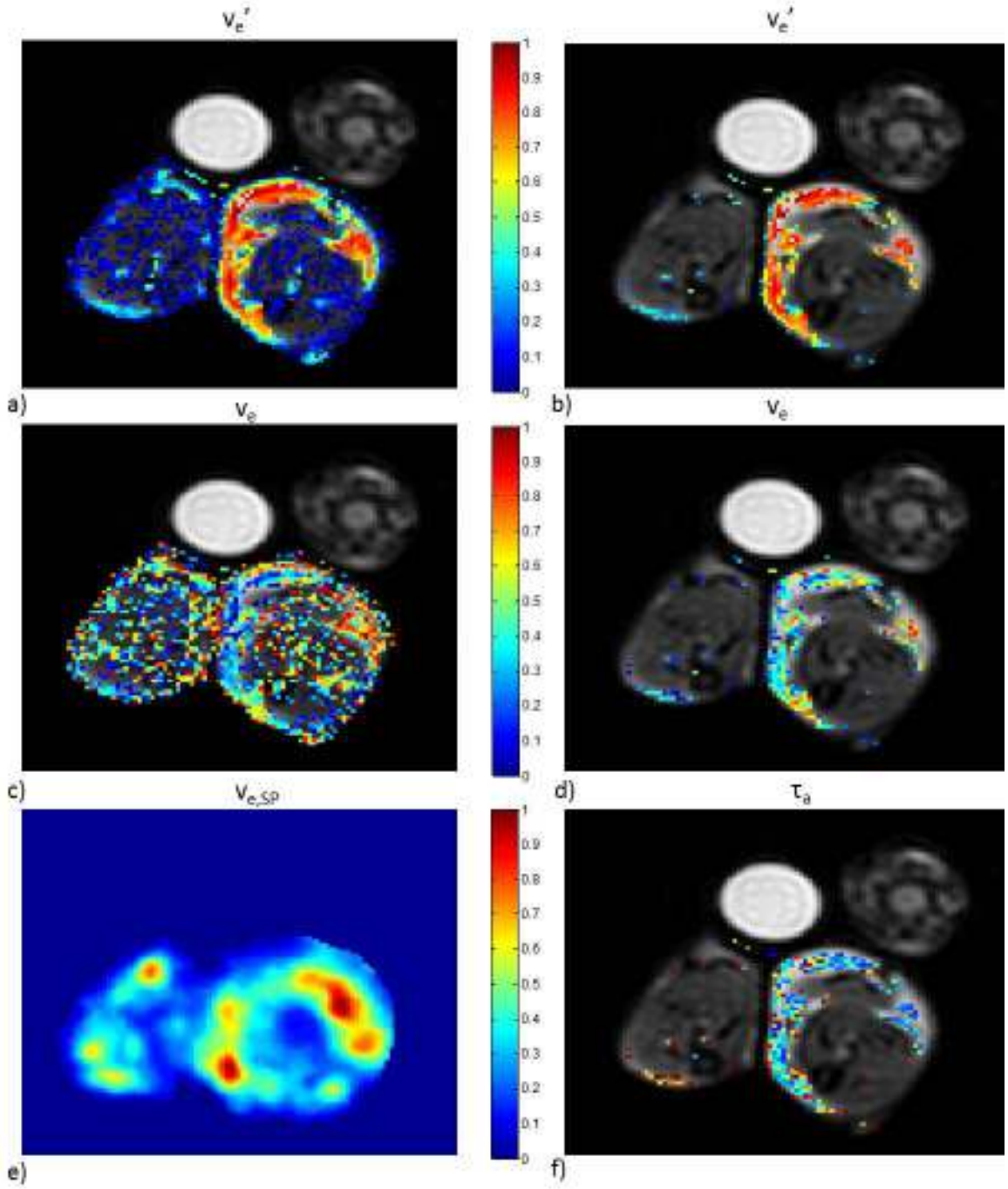

Fig. 5.3. Example parametric maps of apparent and intrinsic model parameters. a) v_e' and c) v_e maps containing all voxels exhibiting two or more signal components. b) v_e' , d) v_e , and f) τ_a maps with voxels exhibiting two or more signal components where $0 < v_e < 1$ and $0 < \tau_a <$ 2s. e) $v_{e,SP}$ parametric map.

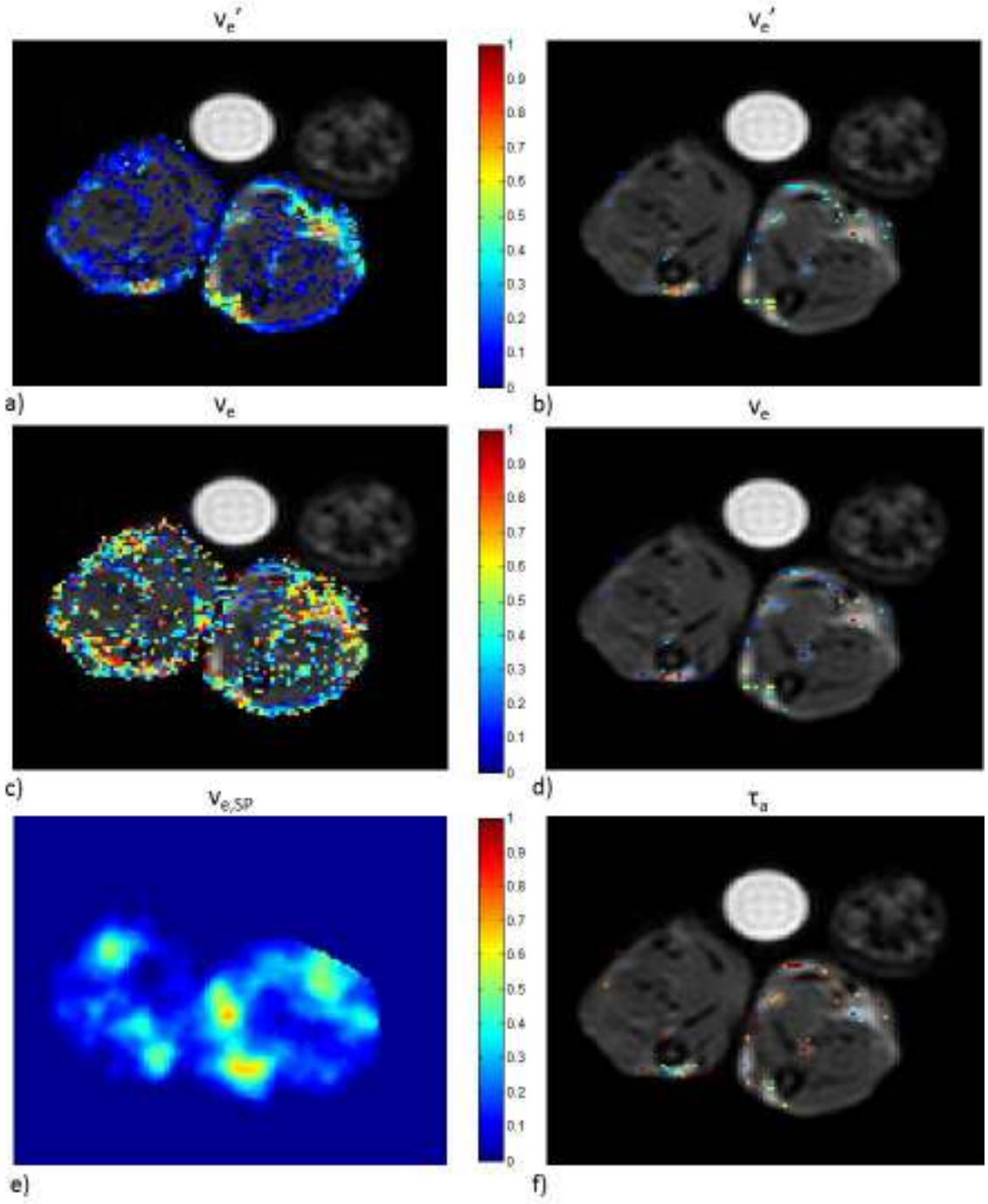

Fig. 5.4. Example parametric maps of apparent and intrinsic model parameters. a) v_e' and c) v_e maps containing all voxels exhibiting two or more signal components. b) v_e' , d) v_e , and f) τ_a maps with voxels exhibiting two or more signal components where $0 < v_e < 1$ and $0 < \tau_a <$ 2s. e) $v_{e,SP}$ parametric map.

In contrast to Fig. 5.3, Fig. 5.4 shows the parametric maps for an example where model inversion resulted in a small number of voxels with physiologically relevant estimates of the model parameters. Fig. 5.4a and 5.4c show reasonable characterization of edematous muscle in the v_e' and v_e maps, however, when the parameters were constrained to physiologically relevant values as in Fig. 5.3, the resulting maps in Fig. 5.4b, 5.4d, and 5.4f show only a sparse number of voxels meeting these criteria. Many of the voxels characterized in Fig. 5.4c exhibited large values of τ_a (>10s), possibly indicating a breakdown of the model. This appears to be the case in many voxels in regions of normal appearing tissue.

Results from the ROI analysis based on the values in the parametric maps (i.e. Fig. 5.4a and 5.4c) revealed median values of v_e' with a range = 0.30-0.72, while median values of v_e had a range = 0.30-0.64. The mean variance in v_e' across animals in an ROI was 0.02, while the mean variance in v_e across animals in an ROI was 0.87. The larger mean variance in v_e indicates the increased heterogeneity with the v_e maps as well as the inclusion of voxels exhibiting $v_e > 1$. Fig. 5.5 shows the comparison of v_e' and v_e vs. $v_{e,SP}$ from the ROI analysis using the total signal in the ROI as a basis for parameter estimation. The estimates of v_e and $v_{e,SP}$ were found to exhibit a significantly higher correlation (R^2=0.443) with each other when compared to v_e' and $v_{e,SP}$ (R^2=0.001).

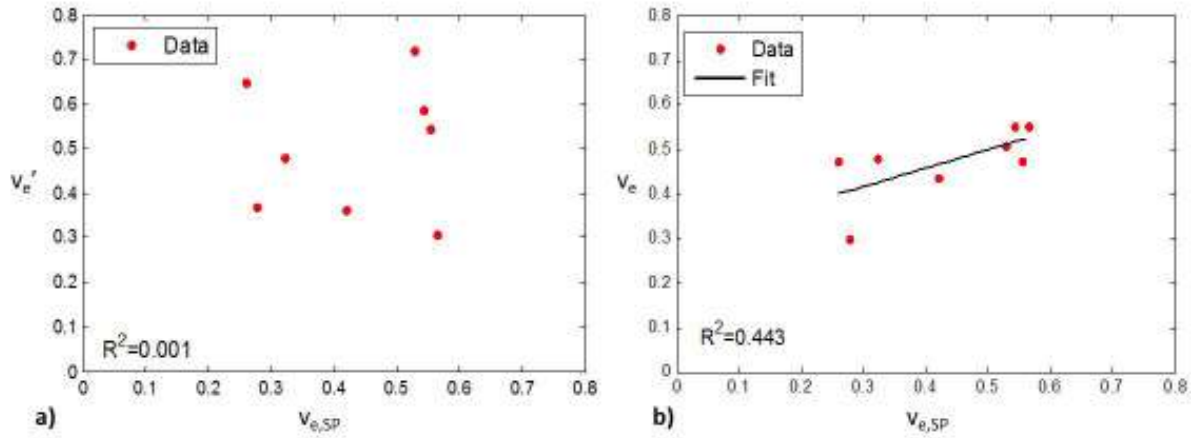

Fig. 5.5. Plot of ROI measures of a) v_e' and b) v_e vs. $v_{e,SP}$ ROI estimates from the quantitative SPECT method. Regression line and associated R^2 values also shown.

Table 5.1 shows the corresponding intrinsic parameter values (mean ± std. deviation (SD)) from inversion of the two-pool model for all eight animals. Voxels that exhibited physiologically relevant values of $0 < v_e < 1$ and $0 < \tau_a < 2$s were included in this analysis. In general, v_e' was found to overestimate v_e in every case.

Table 5.1. Intrinsic model parameter values from voxel-by-voxel analysis.

Animal	v_e'	v_e	T_{2a} (ms)	T_{2b} (ms)	τ_a (s)
1	0.57±0.15	0.46±0.13	29.9±8.4	196.1±89.6	0.551±0.369
2	0.52±0.14	0.43±0.14	28.0±4.1	208.5±92.7	0.629±0.426
3	0.39±0.17	0.31±0.14	26.2±4.5	222.5±80.1	0.878±0.585
4	0.62±0.16	0.50±0.14	31.3±5.9	254.1±90.9	0.447±0.328
5	0.39±0.17	0.31±0.14	26.7±4.7	214.2±118.1	0.885±0.512
6	0.57±0.15	0.45±0.16	28.9±4.1	216.6±94.2	0.623±0.470
7	0.41±0.20	0.33±0.15	26.3±2.7	231.7±89.4	0.894±0.672
8	0.34±0.10	0.26±0.12	23.8±1.9	186.2±67.2	0.822±0.403

Values are mean ± SD.

Further analysis of the values in Table 5.1 shows a high negative correlation (R^2=0.873) between the mean values of v_e and τ_a from the voxel-by-voxel analysis (Fig. 5.6), possibly indicating a relationship between the severity of inflammation/damage and integrity of the muscle cell membrane. In addition, a monotonic increase was observed in the mean value of v_e (from the voxel analysis) with an increase in the λ-carrageenan injection concentration while exhibiting a moderate correlation (R^2=0.458).

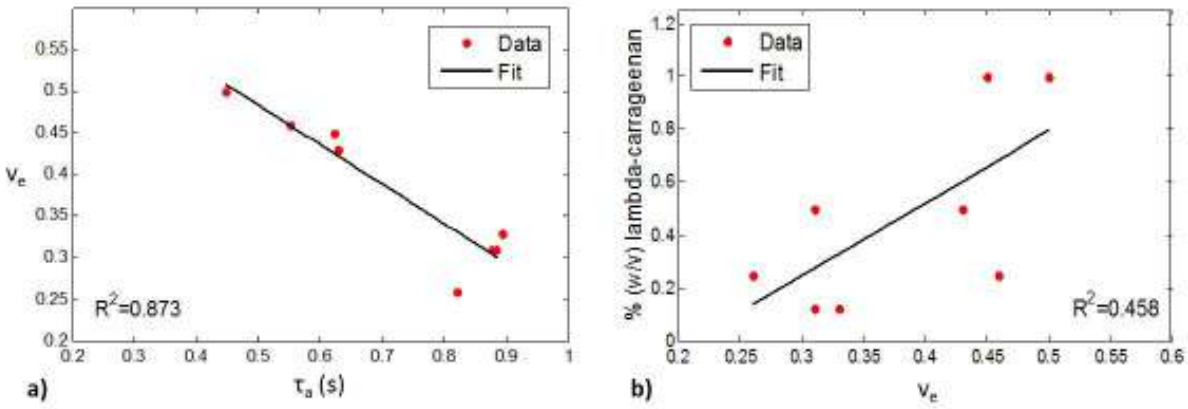

Fig. 5.6. a) Plot of mean v_e vs. mean τ_a from all voxels exhibiting $0 < v_e < 1$ and $0 < \tau_a < 2$s across all eight animals. b) Plot of λ-carrageenan injection concentration (% w/v) vs. mean v_e from all voxels exhibiting $0 < v_e < 1$ and $0 < \tau_a < 2$s across all eight animals. Regression lines and R^2 values also provided.

7. Discussion

As noted in previous studies (14,15,92), muscle inflammation can result in the observation of multi-exponential T_2 (MET_2), predominately with long- and short-lived signal fractions. The accuracy of the resulting estimates of compartmental volume fractions and T_2 times is questionable, however, due to the unknown effect of compartmental water exchange. In this study, a relatively simple technique was presented for measuring exchange-resolved volume fractions for the purpose of inverting a two-pool model of relaxation.

T_2 spectra were used to select voxels exhibiting multi-exponential T_2 decay, as the application of the present technique was predicated on an observed signal well characterized by bi-exponential relaxation. Though most of the selected voxels were from edematous muscle regions, it should be noted that voxels in regions considered to represent normal muscle also exhibited bi-exponential relaxation on occasion. These normal muscle voxels, however, often resulted in v_e values that were larger than the corresponding v_e' value and therefore led to non-sense values of τ_a upon model inversion. This observation, therefore, may show a limitation of the current method on analyzing healthy muscle as well as other tissue types presenting with predominantly monoexponential signal decay.

The calculation of v_e in this study was sensitive to the quality of the fit to a bi-exponential signal both before and after the introduction of the CA. As previously indicated, a long TR was used to avoid bias from T_1 differences in the pre- and post-contrast measurements. The increase in this imaging parameter ultimately lengthened the acquisition time, but also served to increase the image SNR, which was essential to performing the calculation of v_e and the subsequent model inversion. The overall sensitivity of the current method is demonstrated in portions of the v_e parametric maps where a more heterogeneous region may be resultant of voxels either exhibiting low SNR and/or partial volume effects. The lower SNR observed in normal muscle when compared to edematous muscle might also provide an explanation for failure to invert the two-pool exchange model inversion in healthy muscle. To help validate measures of v_e computed with the current method, radionuclide imaging was implemented to provide a comparable estimate of the extracellular volume fraction.

Prior to *in vivo* imaging, the SPECT imaging protocol was tested on an ^{111}In-DTPA phantom and validated with radiotracer activity independently measured in a well counter. Quantification of the radiotracer phantom from the SPECT method (as described in Chapter 2) provided measures of activity that were accurate to within 3%. In addition, the *in vivo* results in an ROI containing normal muscle resulted in $v_{e,SP} = 0.12 \pm 0.03$ (mean±SD across animals), which corresponded well with values of v_e' typically found in normal muscle (82,118). It should be noted that some regions in the unaffected hindlimb of a few animals presented with elevated values (above the mean value described above) of $v_{e,SP}$, however, these regions often appeared to correspond with areas of increased signal intensity in the corresponding MSE images (e.g. Fig. 5.3a and 5.3e).

The quantitative SPECT method allowed for the creation of parametric $v_{e,SP}$ maps which were evaluated on a ROI basis in this study. In a given ROI, the value of v_e was found to have a higher correlation with $v_{e,SP}$ than did the value of v_e', indicating that the estimates of v_e may be more similar to measures of the intrinsic extracellular volume fraction, as represented by the SPECT measures. This observation served to help validate the present method and provided a basis for further investigation into the voxel-by-voxel inversion of the two-pool model for the purpose of extracting measures of inter-compartmental water exchange.

The primary advantage of the contrast enhanced T_2 method presented here is that the measurements and subsequent analysis were performed without the need for a VIF and with little concern for CA concentration. This differs from DCE-MRI, a commonly used method for *in vivo* compartment specific measures of perfusion, volume fractions, and water exchange. In general, the accuracy of the resulting parameter estimates from modeling of

DCE-MRI data are predicated on a well-defined VIF, sufficient temporal sampling, and selection of an appropriate kinetic model (see Chapter 4). Several DCE-MRI studies have investigated transcytolemmal water exchange in tissue pathology (23,108,137,138) and have included τ_a (τ_i in DCE-MRI studies) as a fitted parameter in the pharmacokinetic model, with K^{trans} (volume transfer constant) and v_e as additional model parameters. Results from these studies showed a wide range of τ_a estimates depending on the tissue type, however, other studies suggest that data obtained using clinically relevant DCE-MRI methods may be exchange insensitive and therefore unsuitable for assessing compartmental water exchange (139).

Muscle-specific measures of both the extracellular volume fraction and the intracellular water lifetime have been made *in vivo* in a very limited number of studies (17,139). Landis *et al*. used a precise stepped-infusion method to estimate τ_a in normal rat skeletal muscle (τ_a = 1.1s), however, the method itself precludes its use in routine pre-clinical imaging. In addition, Buckley *et al*. reported measures of τ_a in human obturator muscle using two different pharmacokinetic models. Depending on the model selected, the resulting mean value of τ_a across subjects spanned a wide range (~0s – 4.2s) with SD equivalent to or larger than the mean values in several cases. Similar measures have been made in a variety of tissues, including tumor, however, no such measure in injured/damaged muscle has been reported.

Though data from individual voxels included in the two-pool model inversion were fit with no upper constraint on the value of τ_a, only voxels that exhibited physically relevant measures, $0 < \tau_a < 2$s, were included in the final analysis. This range of intracellular water lifetimes was set to include the mean value of τ_a recorded in normal muscle by Landis et al.

and to exclude unrealistically large values of τ_a that may bias the measurements. It is postulated that the observation of unrealistically high values of τ_a may be due in part to voxels experiencing the slow exchange limit. In assessing the parametric maps for τ_a, many of the voxels in edematous regions exhibited τ_a < 1s. With the previously described constraints, the mean values of τ_a fell within a modest range (0.447-0.894) and were found to be less than that previously observed for normal muscle.

As demonstrated in Fig. 5.6b, a strong negative correlation (R^2=0.873) was observed between the mean value of v_e and the mean value of τ_a. This is to say that as v_e increased due to inflammation and injury there was a resulting decrease in the intracellular mean water lifetime. In the context of this study, it is possible that an increase in cell membrane permeability occurred as a result of the implemented injury model. To explain this observation, one can consider the relationship, $\tau_a = \left(\frac{1}{P}\right)\cdot\left(\frac{V}{A}\right)$, where P is the permeability coefficient of the cell wall, A is its surface area, and V is the volume of the intracellular compartment. Though it is possible that the ratio V/A may increase slightly with edema due to cell swelling, a more drastic increase in cell permeability may occur concurrently to help drive down the intracellular water lifetime and therefore increase the rate of water exchange. This observation is consistent with the hallmarks of animal models of muscular dystrophy, which show increased edema and structural weakness of the sarcolemma with muscle damage (140).

Overall, the technique presented in this study provides a novel means for extracting estimates of intrinsic model parameters from a two-pool tissue model with exchange. Provided enough time for complete CA clearance, this contrast enhanced method may be applied in a repeat fashion to track changes in tissue microstructure with injury or pathology.

As a way to extend this method to human imaging, it is possible that acquisition times for the pre- and post-contrast measurements may be reduced using accelerated MSE techniques, however, SNR may be a limiting factor. At any rate, this method serves as a non-VIF based alternative to the few published techniques for *in vivo* measurements of compartmental water exchange.

8. Conclusion

A method was presented for measuring exchange-resolved extracellular volume fractions for the purpose of inversion of a two-pool tissue model. Quantitative SPECT imaging was used to provide a complimentary measure of the extracellular volume fraction for validation. The contrast enhanced T_2 method was performed in a muscle edema model that was known to exhibit bi-exponential T_2 relaxation. Results showed that, in general, the intrinsic value of the extracellular volume fraction was smaller than the corresponding observed value in a given voxel. Subsequent model inversion provided reasonable estimates of the intracellular water lifetime in injured muscle that were less than those previously observed in normal muscle.

CHAPTER 6

COMPARTMENTAL T_2 RELAXOMETRY WITH A FAST MULTI-ECHO MULTI-SLICE ACQUISITION

1. Abstract

Quantitative measures of T_2 have been made in a variety of tissues, however, robust measures of compartmental relaxation have often been limited to single slice imaging in pre-clinical animal models. Commonly used multiple spin-echo (MSE) experiments require long scan times and are often sensitive to motion, making them non-ideal for human imaging. Translation of these methods to the clinic requires the addition of multi-slice coverage as well as shorter scan times. Because relaxation times and compartmental volume fractions have been shown to change with injury and disease (as demonstrated in Chapter 5), a fast method for *in vivo* evaluation of these NMR tissue parameters would be beneficial. To this end, a modified half-Fourier single-shot spin-echo method for measuring T_2 relaxation (T_2-HASTE) is presented. This technique is evaluated in both doped water and agar gel phantoms with a wide range of T_2 values, and is validated against a single-slice MSE measurement in a muscle edema model exhibiting multi-exponential T_2 relaxation. Due to the overall scan time reduction, this method offers a clinically translatable method for reliable characterization of T_2 in a variety of tissues.

2. Introduction

Quantification of transverse relaxation has been employed in a broad range of MRI applications, with measures of T_2 made in a variety of tissues to describe microanatomy and disease states. These measures are often made via spin-echo techniques (30,31). Specifically, MSE methods are employed to acquire images at various echo times. The resulting data is then fitted to a decaying exponential function to extract the relaxation times. Though these types of measurements are used in pre-clinical applications, they are often only made in a single-slice and, based on acquisition time, are limited in their use in humans.

T_2 estimation with traditional MSE measurements can be affected by both B_0 and B_1 inhomogeneities (as previously described). To mitigate these effects, MSE measurements have implemented non slice-selective composite refocusing pulses as well as custom spoiler gradient arrangements to help minimize signal from non spin-echo pathways (34,36). Though composite pulses may improve accuracy in T_2 estimation, their use precludes multi-slice imaging. It is possible to extend MSE imaging to multi-slice coverage with shaped refocusing pulses, however, spatially varying B_1 across slice profiles and imaging volumes can lead to incomplete refocusing, known to produce unwanted stimulated echoes (33,141). It has also been shown that off-resonance effects created by slice-selective refocusing pulses from different slices may introduce magnetization transfer contrast into an image (141). In addition to problems associated with multi-slice MSE imaging, other limiting factors in translation of MSE imaging are the lengthy acquisition times and resulting sensitivity to motion.

Current pre-clinical methods of measuring T_2 typically acquire a single line of k-space at several TEs within a given TR. Alternate approaches to traditional MSE techniques have been explored as a means to decrease scan time when making T_2 measurements. One

approach for reducing scan time is to acquire an entire image in a given TR (single-shot imaging). Several of these strategies make use of a T_2 preparation period prior to readout (142,143). Foltz *et al* used an involved pulse sequence with magnetization storage and spiral readout to acquire monoexponential T_2 images of the heart. Using a similar sequence, Oh *et al* acquired images with non-linearly spaced TEs using 12 different T_2 preparations and multi-slice spiral acquisition to characterize MET_2 in white matter. These approaches, while valid, may be prone to errors due to non-cartesian data acquisition and reconstruction. More recent studies on T_2 estimation have focused on improving measurement accuracy by implementing post-processing techniques based on the extended phase graph (EPG) algorithm (144,145). These methods, however, are not necessarily aimed at reducing scan time.

To address the previously described shortcomings of translating standard MSE to human imaging, a new single-shot approach for quick and accurate T_2 characterization is presented. The acquisition strategy, referred to as T_2-HASTE, is introduced as a technique for rapid MET_2 characterization as well as T_2 mapping. Specifically, modifications to the HASTE (104) (half-Fourier single-shot turbo spin-echo) pulse sequence are made to allow collection of multi-slice multi-echo data. The T_2-HASTE pulse sequence is assessed on its ability to provide robust multi-slice measures of T_2 with reduced scan time when compared to conventional MSE acquisitions. Experiments focus on validation against a single-slice MSE method in doped water and agar gel phantoms as well as evaluating the sensitivity of the current method to changes in B_1. A pre-clinical model of muscle edema is also implemented to assess the ability of T_2-HASTE in accurately measuring MET_2 *in vivo*. In

addition, the use of non-linear echo sampling with T_2-HASTE, is evaluated experimentally as well as analytically with Cramer-Rao lower bound (CRLB) analysis (146).

3. Methods

3.1 T_2-HASTE

Imaging with a typical HASTE pulse sequence reduces scan time and increases the possible number of imaging slices by acquiring a fraction of k-space in a given TR. Modifications to the conventional HASTE sequence allow modulation of effective echo times (TE_{eff}) and the extension to multiple spin-echo imaging (38,147). T_2-HASTE modulates TE_{eff} with a variable number of spin-echoes (preparation echoes) that are identical to those in the imaging portion of the sequence. The preparation echoes are created by slice-selective refocusing pulses without readout. This modification maintains the gradients and radiofrequency pulses used in the imaging portion of the sequence, and helps minimize unwanted interruptions in the steady-state magnetization. In addition, contribution from unwanted coherence pathways at the refocusing bandwidth edges are reduced by increasing the relative slice thickness of the refocusing pulses to the excitation pulse (38,39). A 1000 μs sinc excitation pulse was used with 125 μs gauss refocusing pulses to produce a refocusing slice thickness of approximately twice the excitation slice thickness when the excitation and refocusing slice select gradients were held equal. The pulse sequence for the T_2-HASTE approach can be seen in Fig. 6.1.

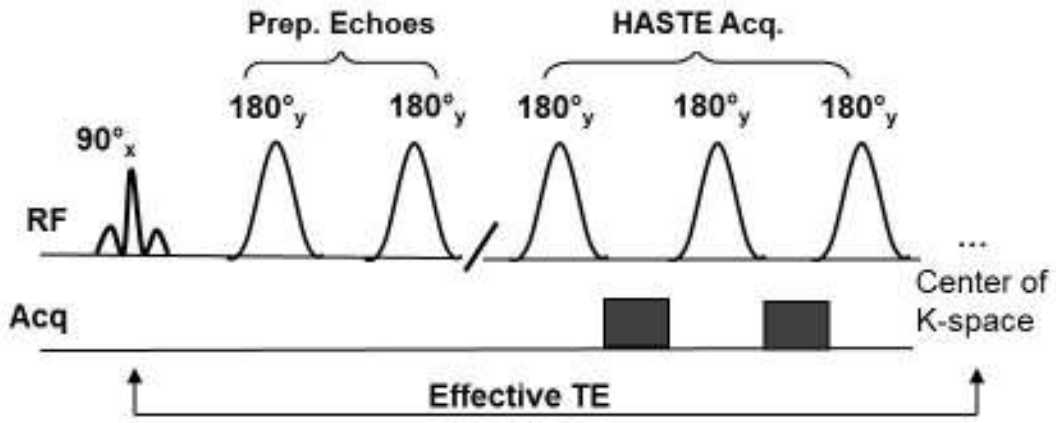

Fig. 6.1. Simplified T_2-HASTE pulse sequence diagram. Note the 180° preparation pulses without readout.

3.2 Experimental

All experiments were performed on a 4.7T horizontal-bore magnet (Agilent, Santa Clara, CA) using a 38 mm diameter Litz quadrature coil (Doty Scientific, Columbia, SC). For the T_2-HASTE acquisition, 36 phase encoding lines (32 lines on the full side of k-space and 4 lines on the conjugate side) were acquired with ESP_{min} (minimum echo spacing) = 3.75 ms for a minimum TE_{eff} = 18.75ms. In addition to T_2-HASTE, a single-slice MSE (MESS) acquisition was used to collect robust T_2 decay data for validation of the present technique. The MESS sequence implemented in this study is similar to that described in Fig. 2.3 with the exception of late echo collection.

3.3 Phantom Experiments

$MnCl_2$ and $CuSO_4$ doped water phantoms were created with varying concentrations corresponding to T_2s ranging from 20ms to 150ms. Phantoms with different chemical dopings (i.e. $MnCl_2$ and $CuSO_4$) were used to test the effect of T_1 on resulting T_2 measurements. T_2-HASTE was performed with TR = 4s, $TE_{eff,1}$(TE_{eff} of first echo) =

18.75ms, subsequent TE_{eff} = 11.25ms, nTE_{eff}(number of TE_{eff}) = 35, and NEX (number of averages) = 2. The images were reconstructed to a 64 x 64 matrix with a field of view (FOV) of 32 x 32 mm^2. To evaluate the effect of B_1 variation on T_2 estimation with T_2-HASTE, the flip angle of the refocusing pulse was varied between 180° and 30° in a single-slice containing the $MnCl_2$ and $CuSO_4$ phantoms. The performance of T_2-HASTE was also evaluated in agar gel phantoms with concentrations of 1%, 2%, 3%, and 4%. Experiments were carried out with the same imaging parameters as with the doped water experiments. Both single-slice and multi-slice (slices = 7, TH (slice thickness) = 2mm) data were acquired. A gap equal to the excitation slice thickness (gap = 2mm) was used between imaging slices. In addition, non-linear TE_{eff} spacing was also implemented to evaluate this sampling scheme in characterizing T_2 with a reduced scan time. Twenty-two logarithmically spaced TE_{eff} (based on ESP_{min}=3.75ms) were acquired within a range of 18.75ms to 401.25ms. Validation of the phantom experiments described above was carried out via comparison to the MESS acquisition performed with TR = 4s, TE_1 = 18.75ms, TE = 11.25ms, nTE (number of TE) = 35, NEX = 2, slice thickness = 2mm, and FOV= 32 x 32 mm^2.

3.4 In-vivo Experiments: Muscle Edema Model

Edema was created in rat hindlimb using a previously described protocol (see Chapter 5) with a 1.0% w/v injection of λ-carrageenan. T_2-HASTE measurements were made with TR = 4s, $TE_{eff,1}$ = 18.75ms, subsequent TE_{eff} = 11.25ms, nTE_{eff} = 35, NEX=2, 128 x 64 samples, and FOV= 32 x 32 mm^2. Fourteen slices (TH = 2mm, gap = 2mm) were collected over 2 acquisitions to encompass the region of edematous muscle. Similar to the agar phantom experiment, non-linear TE_{eff} sampling with a range of 18.75ms to 401.25ms was also

employed. Again, MESS measurements were acquired with imaging parameters identical to those described above for validation.

4. Data Analysis

The T_2-HASTE images were reconstructed offline in MATLAB, using partial Fourier reconstruction techniques as described in Chapter 2 (103). To evaluate possible blurring in the T_2-HASTE phantom images, a point spread function (PSF) was deconvolved from a profile through the center of each $CuSO_4$ and $MnCl_2$ cylindrical phantom. For T_2 characterization, the echo magnitude data from ROIs in both phantom and *in vivo* experiments were used to create a T_2 spectrum with Eq. [2.9]-[2.11] and the technique described in Chapter 2. Compartmental T_2s and volume fractions were extracted from the resulting T_2 spectra for comparison between the T_2-HASTE measures and the gold-standard MESS measures. To assess the value of T_2-HASTE in fast T_2 mapping, multi-slice T_2 maps were created for the agar gel phantoms by performing a voxel-by-voxel fit of M_0 and T_2 in Eq. [2.3], using *lsqnonlin* in MATLAB.

4.1 Cramer-Rao Lower Bound (CRLB) Analysis

The Cramer-Rao lower bound provides a lower limit on the variance of an estimator for a particular parameter determined from experimental data. In the context of this study, the observed MR signal from edematous muscle tissue can be primarily described by bi-exponential relaxation,

$$S(TE_{eff,n}) = f_a \cdot \exp\left(\frac{TE_{eff,n}}{T_{2a}}\right) + f_b \cdot \exp\left(\frac{TE_{eff,n}}{T_{2b}}\right) \qquad [6.1]$$

where n = [1,2,….,nTE$_{eff}$]. Unbiased estimates of the model parameters in Eq. [6.1], f_a, f_b, T_{2a}, and T_{2b}, result from a non-linear least-squares fitting of the model to a series of observations, $S(TE_{eff,n})$. For any parameter, θ_k, the CRLB of its standard deviation (SD), $s(\theta_k)$, is defined by

$$s(\theta_k) = \sqrt{(F^{-1})_{kk}} \qquad [6.2]$$

where F is the Fisher information matrix given by

$$F_{jk} = \frac{1}{\sigma^2} \sum_n \left(\frac{\partial S(TE_{eff,n})}{\partial \theta_j} \frac{\partial S(TE_{eff,n})}{\partial \theta_k} \right) \quad . \qquad [6.3]$$

where σ is the standard deviation of the image noise. The unbiased estimate of parameter, θ_k, therefore, has a variance that is no less than $s^2(\theta_k)$. To further evaluate the advantage of non-linear echo sampling with the T_2-HASTE method, the CRLB for each of the model parameters in Eq. [6.1] was computed and compared to the CRLB of the same parameters from the standard MSE approach. The model parameters in Eq. [6.1] were set to f_a = 0.60, T_{2a} = 25ms, f_b = 0.40, and T_{2b} = 100ms to represent typical values found in edematous skeletal muscle (see Chapter 5). For the MSE case TE = 10 ms with NE = 40 linearly spaced echoes. For T_2-HASTE, TE$_{eff,1}$ = 18.75=ms with NE = 64 logarithmically spaced samples (ESP$_{min}$ = 3.75ms) up to TE$_{eff}$ = 401.25ms. In this analysis, the non-linear echo sampling afforded by

T_2-HASTE allowed for the acquisition of an increased nTE_{eff} while maintaining the same scan time as the MSE acquisition (assuming 64 phase encoding steps).

5. Results

Fig. 6.2a shows a typical T_2-HASTE image (center slice) containing eight cylindrical $CuSO_4$ and $MnCl_2$ doped water phantoms with varying concentrations and T_2s. Fig. 6.2b shows the PSF for each of the doped water phantoms. The PSF was found to be significantly broader in the solutions with shorter T_2 values, in particular the 52.6 mM $CuSO_4$ ($T_{2,MESS} \approx$ 22ms) and 0.34mM $MnCl_2$ ($T_{2,MESS} \approx$ 19ms) doped phantoms. This broadening is a result of excessive signal decay over the lines of k-space in the T_2-HASTE acquisition.

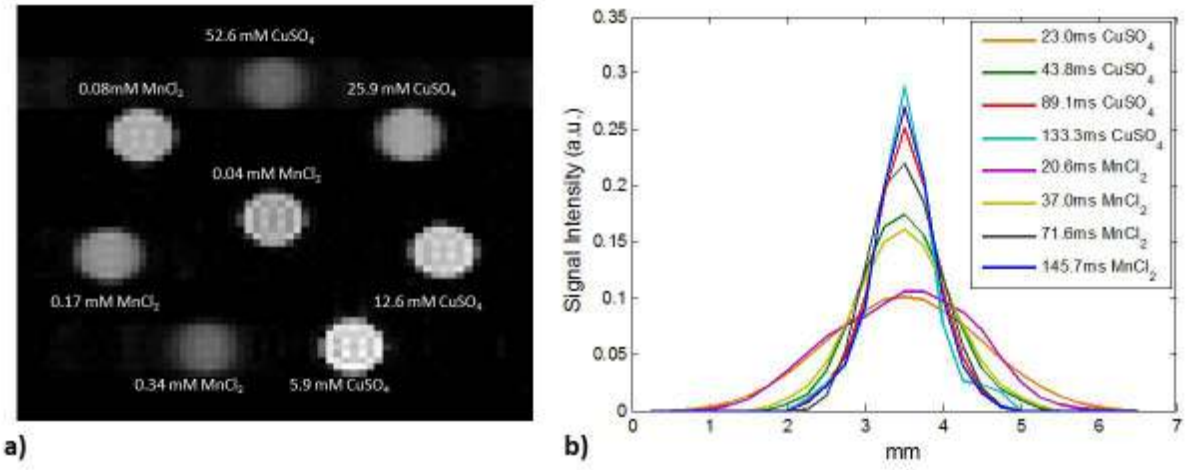

Fig. 6.2. a) T2-HASTE image (TE_{eff} = 18.75ms) of $CuSO_4$ and $MnCl_2$ doped water phantoms. b) Point spread function (PSF) of each doped water phantom from T_2-HASTE image.

Fig. 6.3 shows the response of T_2-HASTE in accurately measuring T_2 in the presence of varying B_1. Fig. 6.3a shows the measured decay curves for a $MnCl_2$ phantom ($T_{2,MESS}$ = 69.2ms) with refocusing flip angles varied between 30°-180°. The decay curves show an

insensitivity to flip angle variation between 150° and 180° where the estimate of T_2 was < 3% larger than the corresponding estimate of $T_{2,MESS}$. Beyond 150°, the estimates of T_2 were more than 10% larger than $T_{2,MESS}$ and in extreme cases the decay curves became non-monoexponential. Fig. 6.3b shows the T_2 decay curves in a $CuSO_4$ phantom where T_1 is on the order of T_2. Aside from differences in the maximum signal intensity, the T_2 estimates were within 3% of $T_{2,MESS}$(=89.0ms) with refocusing flip angles down to 90°.

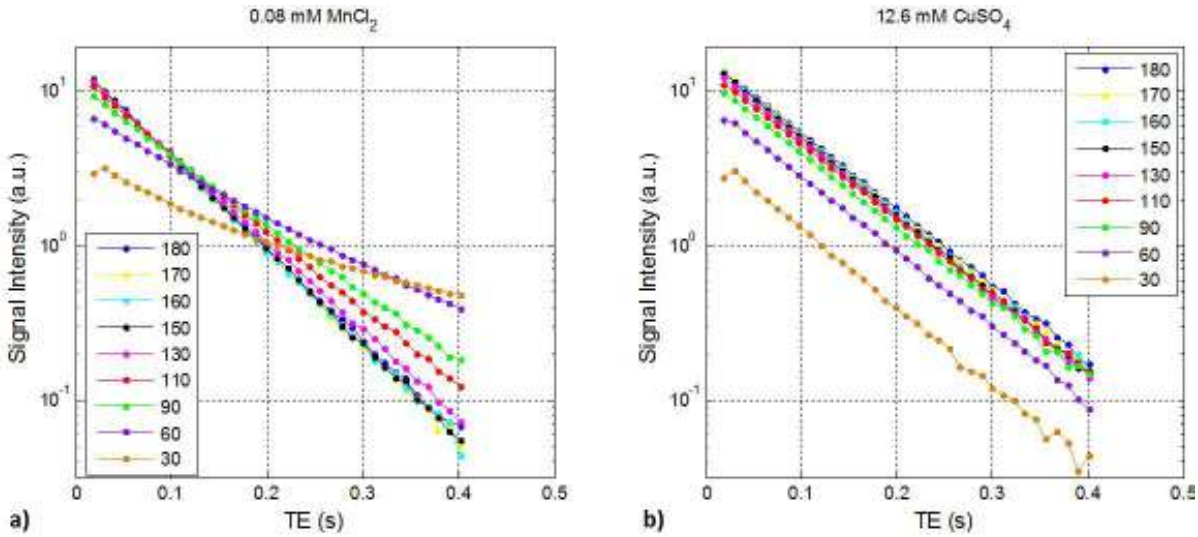

Fig. 6.3. T_2 decay curves (log scale) with varying flip angle (in degrees) for a) 0.08 mM $MnCl_2$ phantom and b) 12.6 mM $CuSO_4$ phantom.

ROI analysis of the image in Fig. 6.2a revealed T_2 decay with the corresponding T_2 values as seen in Table 6.1. The observed values from T_2-HASTE corresponded well with the values obtained from the conventional MESS acquisition, showing less than a 5% difference in most cases (except 0.34mM $MnCl_2$) across a broad range of T_2s.

Table 6.1. T_2 values extracted from T_2 spectra of doped phantoms.

[$CuSO_4$]	52.6 mM	25.9 mM	12.6 mM	5.9 mM
T_2-HASTE	23.0 ms	43.8 ms	89.1 ms	133.3 ms
MESS	22.1 ms	44.1 ms	89.0 ms	129.4 ms
[$MnCl_2$]	0.34 mM	0.17 mM	0.08 mM	0.04 mM
T_2-HASTE	20.6 ms	37.0 ms	71.6 ms	145.7 ms
MESS	18.5 ms	37.8 ms	69.2 ms	143.2 ms

Fig. 6.4 shows the resulting T_2 maps from the multi-slice T_2-HASTE acquisition (with linear TE_{eff} sampling) in the agar phantom as well as the T_2 map from the MESS acquisition.

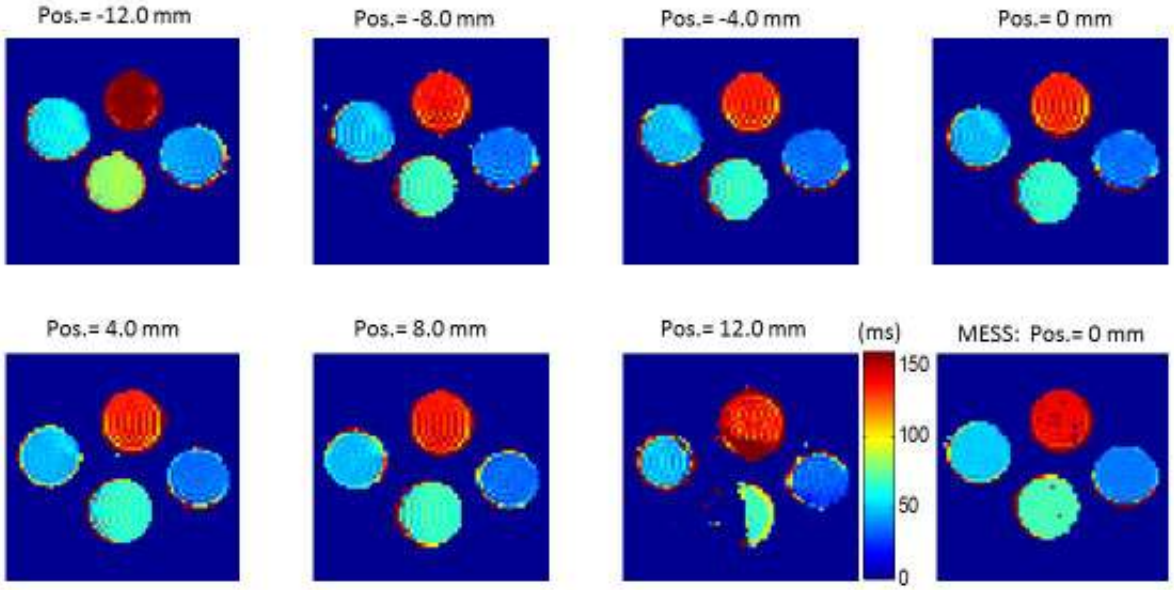

Fig. 6.4. Multi-slice T_2 maps calculated from T_2-HASTE acquisition in agar gel phantom. Slices were separated by a 2mm gap. The T_2 map for the MESS data is shown for comparison.

The observed T_2s varied by less than 7% (compared to $T_{2,MESS}$) across slices 2 through 6, indicating insensitivity to B_1 variation within this imaging volume (range=18mm). These results appear to be consistent with the previously described T_2 variation with flip angle.

Voxels with highly elevated T_2s occurred only at slices furthest from the center slice where the applied flip angle may be significantly different from 180°. It is noted that T_2 estimates from slices 2 through 6 were found to underestimate those values from the MESS acquisition, however, the estimates in slice 1 and 7 did overestimate $T_{2,MESS}$ as would be expected based on the variation in Fig. 6.3. The T_2 estimates for the multi-slice acquisition in the agar phantom can be seen in Table 6.2.

Table 6.2. ROI estimates from agar phantom T_2 maps.

	[Agar] (%w/v)			
Slice (Pos)	**4%**	**3%**	**2%**	**1%**
1 (-12.0mm)	42.5	57.5	87.5	172.5
2 (-8.0mm)	36.9	48.3	68.3	137.2
3 (-4.0 mm)	36.2	48.6	67.0	135.2
4 (0 mm)	36.1	48.4	66.8	134.3
5 (4.0 mm)	36.0	48.2	66.9	134.9
6 (8.0 mm)	35.2	49.4	67.8	137.5
7 (12.0 mm)	34.6	64.3	N/A	138.2
MESS (0 mm)	37.7	50.9	70.8	140.3

T_2 values (ms) extracted from ROIs on T_2 map.

Fig. 6.5 shows the decay curves and resulting T_2 spectra from ROIs in the agar gel phantom for a single-slice T_2-HASTE acquisition with non-linear TE_{eff} sampling. The difference in T_2 between the linear and non-linear TE_{eff} sampling strategies was found to be less than 1%. These data suggest that T_2 can be accurately measured by T_2-HASTE with 22 log-spaced TE_{eff} as used in this study.

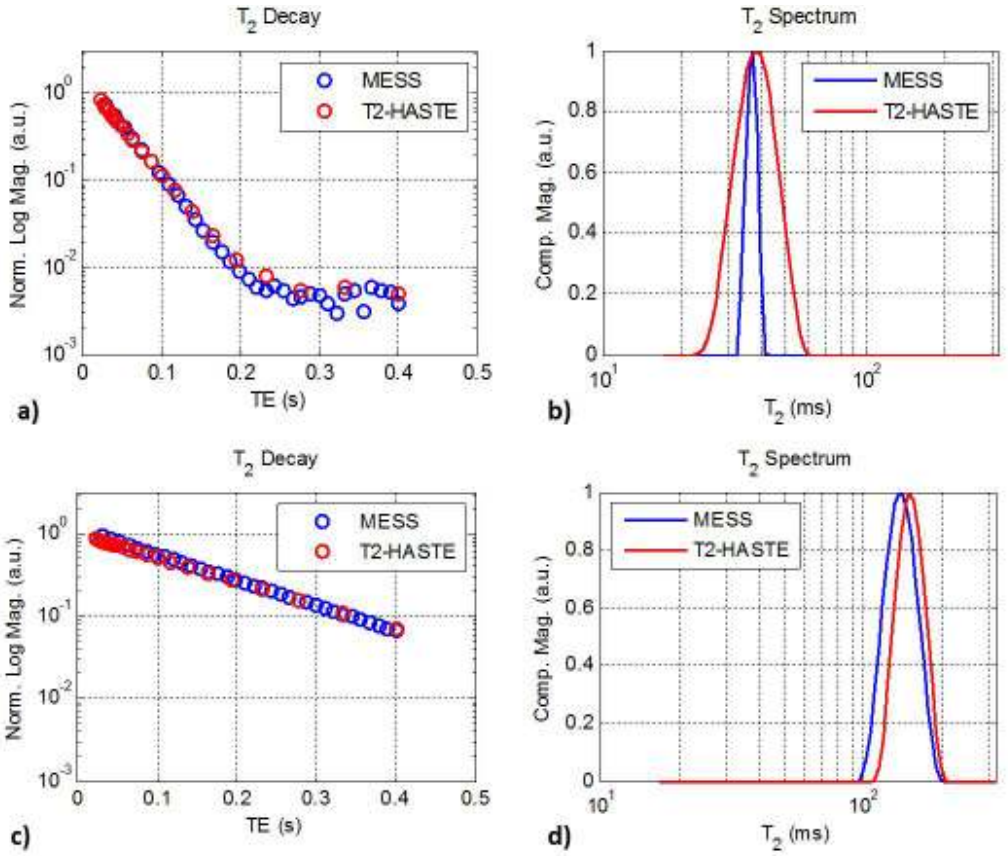

Fig. 6.5. Example T_2 decay curves and associated T_2 spectra for T_2-HASTE acquisition with non-linear TE_{eff} sampling in (a, b) 4% agar and (c, d) 1% agar.

Fig. 6.6 shows multi-slice images from the T_2-HASTE acquisition in an animal model of muscle edema. The edematous region can be seen in the left hindlimb as areas of increased signal intensity. Fig. 6.7 shows example T_2 decay curves and corresponding T_2 spectra from an ROI in normal and edematous muscle. Regularization in the T_2 spectra was manually adjusted with $\mu \approx 0.3$ such that both spectra only displayed two signal components. The data in Fig. 6.7a-d were acquired with linear TE_{eff} sampling and both the normal muscle and edematous muscle T_2-HASTE decay curves correlated well with those from the MESS acquisition.

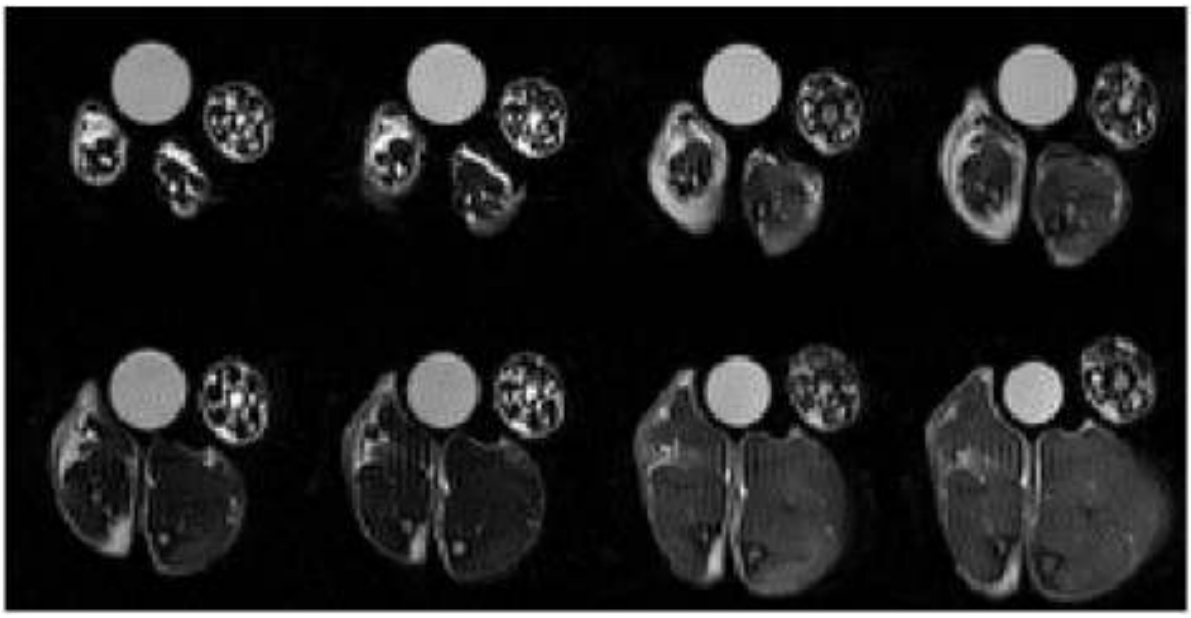

Fig. 6.6. Multi-slice images from T_2-HASTE acquisition in rat muscle edema model. Edema is present in the left hindlimb. Also included are a $MnCl_2$ water phantom and the animal's tail.

Fig. 6.7e and Fig. 6.7f show the non-linear TE_{eff} sampled data from the same ROIs as in Fig. 6.7c and Fig. 6.7d. The resulting T_2 values and volume fractions (in parentheses) for both linear and non-linear sampling strategies can be seen in Table 6.3.

Table 6.3. Estimates of T_2 and volume fractions from muscle model.

	Normal	$Edema_A$	$Edema_B$
MESS	26.5 ms	28.4 ms (0.64)	108.4 ms (0.36)
T_2-HASTE (L)	27.1 ms	25.4 ms (0.60)	107.5 ms (0.40)
T_2-HASTE (NL)	27.2 ms	23.8 ms (0.57)	96.0 ms (0.43)

L- linear TE_{eff} sampling; NL- non-linear TE_{eff} sampling

The T_2-HASTE estimates were shown to be within 3% of the corresponding MESS measure for normal muscle, while the compartmental measures using T_2-HASTE with linear sampling were within ~10% of the MESS measures in edematous muscle.

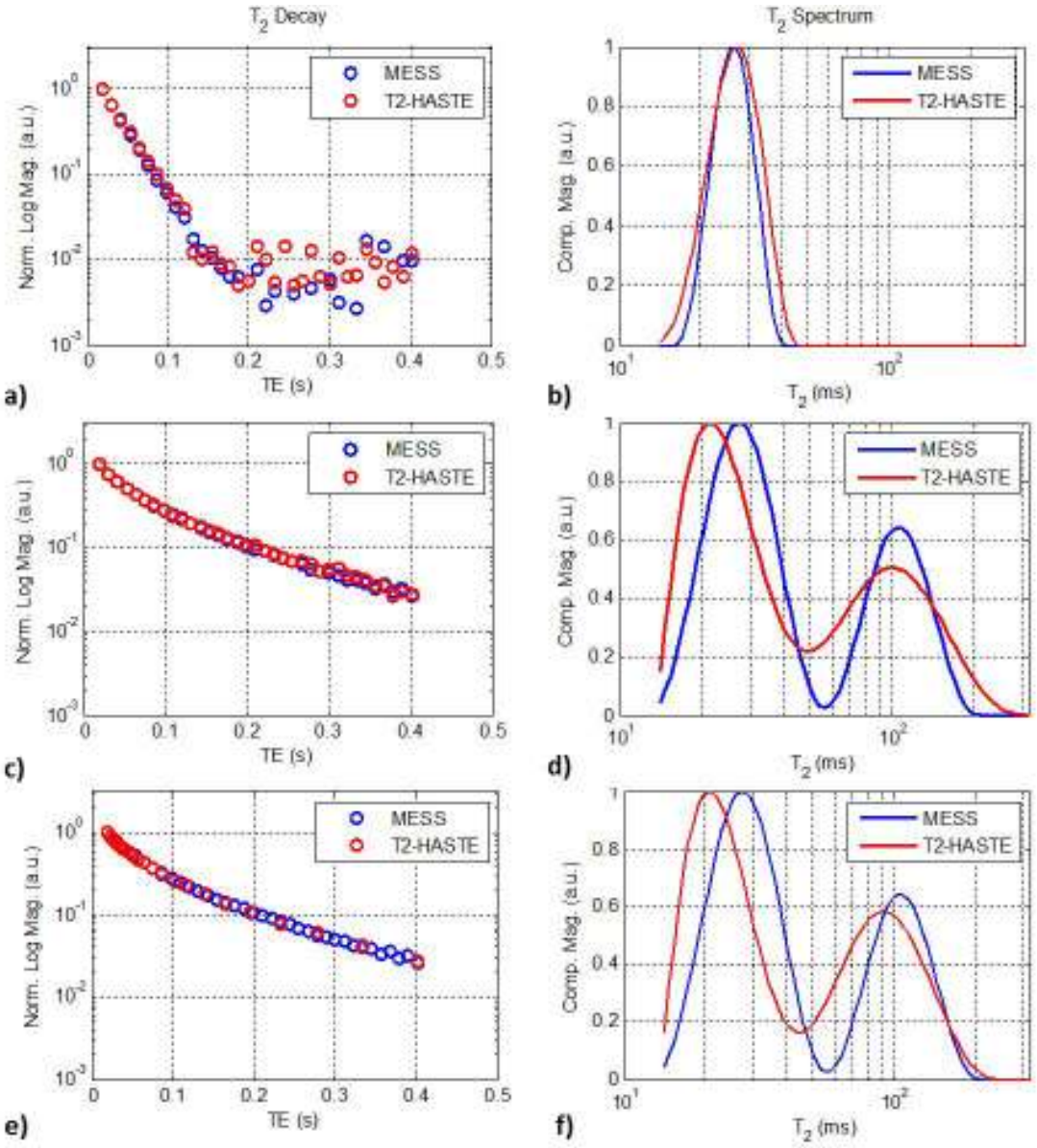

Fig. 6.7. Example T_2 decay curves and associated T_2 spectra for T_2-HASTE acquisition with linear TE_{eff} sampling (L) in (a, b) normal muscle and (c, d) edematous muscle, and non-linear TE_{eff} sampling in (e,f) edematous muscle.

The data in Fig. 6.7e, 6.7f, and Table 6.3 also reveal that a sparse sampling of the T_2 decay curve at later TE_{eff} and a significant reduction in scan time still provides reliable measures of multiexponential T_2 and compartmental volume fractions. A difference of less than ~10% was observed when comparing the compartmental characteristics recorded using

non-linear TE_{eff} sampling and those obtained using linear sampling. The results of the CRLB analysis (Table 6.4) provide a measure of parameter uncertainty, when scan time reduction is sacrificed in favor of collecting more echoes. With $\sigma_{T2\text{-}HASTE}$=1/270 and σ_{MESS}=1/350, the value of $s(\theta_k)$ for each fitted parameter from T_2-HASTE was within 5% of the value from the MESS protocol, with the exception of T_{2a}.

Table 6.4. CRLB ($s(\theta_k)$) of fitted parameters from bi-exponential model.

Parameter	f_a	T_{2a} (s)	f_b	T_{2b} (s)
MESS	0.0128	0.0009	0.0155	0.0023
T_2-HASTE	0.0127	0.0011	0.0161	0.0024

6. Discussion

Conventional MSE imaging studies typically employ a CPMG style acquisition for T_2 characterization (30,31). These types of pulse sequences often implement non slice-selective refocusing pulses and are prone to long scan times as well as contamination due to unwanted signal from non spin-echo pathways. The current study presents an alternative method for accelerated acquisition of MSE data acquisition with the addition of multi-slice coverage using a partial Fourier single-shot spin-echo method.

The T_2-HASTE method was evaluated on its ability to produce accurate estimates of T_2 in the presence of B_1 variations effecting refocusing. As part of the pulse sequence design, the refocusing slice profile was increased compared to the excitation slice profile to mitigate B_1 variation across slice profiles, as previously suggested (37-39). In phantom and *in vivo* experiments, the refocusing pulse width was restricted to being relatively short to create the desired slice profile condition. For clinical applications, however, the length of the

refocusing pulse (and excitation pulse) may be increased to accommodate RF power limitations. In a single slice, estimates of T_2 in the $MnCl_2$ phantoms were found to still be accurate (within 3% of $T_{2,MESS}$) when the prescribed flip angle was ~20% less than the ideal 180° refocusing pulse. The observed difference in flip angle effects on the decay curves between $MnCl_2$ and $CuSO_4$ (Fig. 6.2) is important as imperfect refocusing in samples with longer T_1s relative to T_2 can result in stimulated echoes and signal contamination, resulting in inaccurate estimation of T_2. This, however, was shown to not be the case in the current study as the estimates in Table 6.1 were found to correlate well with the $T_{2,MESS}$ estimates. In general, the relative insensitivity to B_1 variation is of importance when performing multi-slice MSE measurements. As with the previously described results, the T_2 estimates in Table 6.2 appear to be relatively unaffected by spatial variation in B_1 across multiple slices.

T_2-HASTE provides certain advantages over conventional MSE imaging, however, the single-shot nature of the sequence does result in some limitations. Because a complete image is collected in a single TR, the resulting image may present with reduced spatial resolution in the phase-encoding direction due to signal decay during data acquisition. This appears to be particularly true in samples with short T_2 components (T_2 < 25ms). This shortcoming is displayed in Fig. 6.2. The blurring effects may be mitigated by reducing the minimum ESP or, possibly, by applying a correction technique that compensates for T_2 decay during echo collection (148,149). Though the previous issue makes tissues such as white matter and nerve less likely candidates for MET_2 characterization with the present method, muscle tissue provides a practical example for the utility of T_2-HASTE, as observed T_2s are upwards of 30 ms at clinical field strengths (150). In addition, muscle inflammation has been previously shown to increase T_2 (see Chapter 5) while producing MET_2 decay (92).

Along with sequence validation in phantoms, T_2-HASTE was evaluated in an *in vivo* rat model of muscle edema, known to exhibit MET_2. Measurements obtained in normal and edematous muscle corresponded well with previous T_2 measures using traditional MSE imaging and a similar λ-carrageenan injection protocol (15). The T_2 of normal muscle was observed to be monoexponential, as has been previously recorded in rat (15). The edematous muscle displayed characteristic bi-exponential T_2 decay with compartmental volume fractions and T_2s ($f_b \approx 0.40$, $T_{2b} \approx 100$ms) associated with similar concentrations of λ-carrageenan (14,15). As described in previous studies, the multiexponential nature of muscle can be attributed to short- and long-lived signal components corresponding to intra- and extracellular tissue compartments (9). The ability to characterize MET_2 with T_2-HASTE may be of clinical relevance, as normal human skeletal muscle has been found to exhibit at least two T_2 components (9,12,13) and the tissue compartments and associated T_2's have been shown to change with muscle inflammation and injury (15,92).

Beyond MET_2 characterization, T_2-HASTE provides a method for fast T_2 mapping, as demonstrated in this study. The nature of measuring monoexponential T_2 for the purpose of creating a T_2 map may allow for the collection of fewer echoes and would serve to further decrease scan time with the use of T_2-HASTE. Recent applications of fast T_2 mapping methods have focused on motion sensitive measures in the heart and liver with breath-hold imaging (151,152). These methods and others (153) produce T_2 maps in shorter scan times than traditional CPMG measurements (often with additional techniques such as parallel imaging), but have not demonstrated dual utility for accurate MET_2 characterization. Additional methods for fast T_2 mapping in various applications have been investigated, with

many of these studies employing more complex (154,155) or non-conventional spin-echo type measurements for T_2 characterization (156,157).

Ultimately, the primary advantage of T_2-HASTE as observed in this study is the reduction in scan time. With the present protocol, MESS measurements were acquired in a scan time of ~ 8 minutes 30 seconds. The T_2-HASTE measurements, however, were made in almost half the scan time, ~ 4 minutes 40 seconds, with multi-slice coverage. Multi-slice multi-echo data was acquired with TE_{eff} modulated by a variable number of preparation refocusing pulses following excitation. Methods employing a so called T_2 prep period for MSE imaging, as implemented here and in other studies (142,143), can benefit from non-linear echo sampling (158). It has been shown, however, that this type of acquisition can produce errors when implemented in traditional MSE experiments (159). Specifically, a loss of magnetization due to imperfect refocusing can introduce non-monoexponential decay when using non-linearly spaced echo times. T_2-HASTE employs linearly spaced refocusing pulses in the preparation period to create individual images with TE_{eff} that can be non-linearly spaced to sample the T_2 decay curve. In the T_2-HASTE experiments, a logarithmic TE_{eff} spacing was used to further reduce acquisition time to 2 minutes 55 seconds. As an example, employing the non-linear approach with a single acquisition and reduced TR (i.e. TR = 2s, NEX = 1, number of TE_{eff} = 20) results in a full multi-slice multi-echo data set acquired in less than 45 seconds.

The decrease in scan time afforded by non-linear echo sampling may also be exchanged for a more densely sampled T_2 decay curve. With ESP = 3.75ms the T_2-HASTE method provides more than twice as many samples in the first 100ms of the T_2 decay curve when compared to the MESS method. The advantage of this trade-off is further demonstrated

in the CRLB analysis. The values of $s(\theta_k)$ for the compartmental volume fractions were nearly identical for the two methods, though the CRLB for T_{2a} was larger for the T_2-HASTE measurements. This is due in part to the longer minimum TE_{eff} used with T_2-HASTE. To remedy this, ESP_{min} could be decreased slightly at the expense of a larger bandwidth.

In addition to current methods focused on accelerating T_2 measurements via pulse sequence design, T_2-HASTE included, recent studies aimed at improving the accuracy of both monoexponential and multiexponential T_2 measures have turned their focus towards post-processing. Lebel *et al*. and Praslowski *et al*. (144,145) implemented the extended phase graph (EPG) algorithm (160) to correct for signal from unwanted coherence pathways sometimes present in MSE data. Though these methods are not specifically aimed at reducing scan time, they do provide a means for improving T_2 characterization in multi-slice and 3D MSE experiments.

Though no one approach is perfect, this study describes a novel method for acquiring multi-slice multi-echo data in a shorter acquisition time than traditional MSE measurements. A rigorous evaluation of the method's sensitivity to B_1 inhomogeneities revealed accurate T_2 estimation over a fairly wide range of refocusing flip angles. Based on the *in vivo* application of this method, T_2-HASTE may be a viable method for quantitative analysis of clinically relevant muscle-related diseases (2,161).

7. Conclusion

This study presents a new method for making quantitative measures of both mono- and multiexponential T_2 with a focus on reducing scan time and incorporating multi-slice data. The so-called T_2-HASTE method is based on a commonly used partial Fourier single-shot

spin-echo acquisition with minor modifications. The T_2-HASTE sequence was validated against traditional single-slice MSE measurements in both doped water and agar gel phantoms. The method was also evaluated in an *in vivo* muscle injury model exhibiting MET_2. Non-linear echo sampling with T_2-HASTE was evaluated experimentally as well via CRLB calculations. Overall, T_2-HASTE provides a means for fast T_2 quantification and may serve as a clinically translatable method for T_2 mapping and compartmental relaxometry.

CHAPTER 7

DISCUSSION AND FUTURE WORK

The studies presented in this dissertation serve to elucidate some of the difficulties and oversights in making accurate compartmental relaxation-based MR measurements. Contrast enhanced measurements using T_1 and T_2 relaxometry were compared to compartmental measures using an *in vivo* SPECT imaging protocol in both a tumor and muscle injury model. In addition, a new method was presented to aid in clinical translation of these types of compartmental measurements, particularly those dealing with transverse relaxation. Both the contrast enhanced MRI measurements and the SPECT measures focused on the validity of *in vivo* estimates of extracellular volume fractions in the presence of tissue water dynamic effects.

As tissue microstructure changes with injury and disease so to do the observed tissue volume fractions. A variety of MRI studies have been performed to help characterize and interpret compartmental tissue characteristics using a wide range of quantitative methods. It is important to note, however, that many of these measurements are based on observed NMR relaxation properties of the tissue and are not necessarily a direct measure (or even representative measure) of the tissue compartments themselves. In addition, complex tissue water dynamics such as transcytolemmal water exchange serve to alter apparent compartmental relaxation rates which may, in turn, lead to observed tissue compartment sizes that are significantly different from their intrinsic values.

The quantitative SPECT methods implemented in these studies were developed as a means for making measures of tissue compartment size unbiased by compartmental water

exchange. To our knowledge these are the first *in vivo* quantitative SPECT studies for the purpose of measuring compartmental volume fractions. These novel methods were validated with radiotracer phantom studies and established *ex vivo* gamma counting techniques. It is possible, however, that further comparison with elegant autoradiography (AR) techniques may bolster the validity of these new techniques. Future *in vivo* studies implementing these quantitative SPECT methods may be best served by including AR (or histological) data in addition to the quantitative imaging data.

As SPECT detector technology improves (162) and energy and spatial resolution are refined, the ability to acquire quantitative data *in vivo*, as demonstrated in this work, will improve, resulting in the possibility of more frequent quantitative pre-clinical SPECT studies. Along similar lines, advances in both SPECT hardware and software may allow the exploitation of the dual-isotope approach presented in this study (163). A feature of this method, however not the focus of the current studies, was the ability to produce measures of tissue blood volume. This type of information may be useful in assessing tissue perfusion for the purpose of functional and/or cancer imaging studies. Furthermore, the implementation of targeted SPECT radiotracers may provide an additional use for the dual-isotope technique and the associated quantitative analysis.

In recent years, the need for further validation of quantitative imaging techniques such as DCE-MRI has become essential as these measurements move towards clinical use. Though the use of DCE-MRI as a research tool has dramatically increased over the past decade (20 fold increase in related publications from 2001-2011) there is still debate as to the best approach for data acquisition as well as the best method for pharmacokinetic modeling. The results of the multi-modal DCE-MRI/SPECT study re-emphasize the need for a more

careful approach to analyzing cancerous tissue, particularly solid tumors. Based on the heterogeneous nature of the pharmacokinetic parameter values from tumor, it appears a simple ROI analysis is not sufficient. In addition to a voxel-wise analysis, additional image-based segmentation of the tumor tissue into well-perfused, poorly perfused, or necrotic regions may need to be performed. Suitable pharmacokinetic models may then be considered for each particular region.

Concerning pharmacokinetic modeling, it has been shown in this work and in other studies that implementation of the Tofts model (with the VIF or RR) may not be appropriate for all tissue types. New models need to be investigated that accommodate different physiological factors such as CA diffusion and the possibility of insufficient perfusion. The accuracy of the acquired VIF should also be further investigated as it has been shown that inflow effects on the VIF may contribute to parameter error. In addition, more focus may need to be placed on the physical interpretation of the model parameters, particularly v_e. A problem arises when studies report non-physical values without justification (164), while others simply do not include v_e (165), possibly due to a lack of confidence in its use as a cancer biomarker. A trend in clinical studies seems to downplay the significance of the actual baseline values of the model parameters and instead places emphasis on the overall change in parameter estimates. It remains, however, that pharmacokinetic models based on tissue compartmentalization should provide reliable and meaningful estimates that are physiologically representative of the tissue of interest.

To address the issue of obtaining compartmental NMR measures unbiased by exchange, a contrast-enhanced T_2 method was developed and tested. This method provided a means for obtaining *in vivo* measures of water exchange in a reasonable acquisition time

when considering typical animal imaging experiments. Though the utility of the contrast-enhanced T_2 method is limited to tissues best described by two compartments, the common implementation of two-pool models in MRI data analysis, specifically in muscle, provides practical applications for this novel method. Implementation of the λ-carrageenan edema model in these studies served as a basis for future work with more involved models of muscle injury.

To further evaluate the contrast enhanced T_2 method, a more clinically relevant model of muscle damage could be investigated. To this end, an ischemia-reperfusion model may be implemented. This particular injury model, often achieved by ligating the femoral artery, presents with edema, myofiber damage, and necrosis early on with eventual fiber remodeling and regeneration in later stages (95). This model has been studied frequently with the use of various MR imaging techniques including diffusion imaging, T_2 relaxometry, and DCE-MRI (96,97,166,167). The contrast-enhanced T_2 method could be combined with diffusion imaging to longitudinally monitor changes in compartment size and cell permeability. Concurrently, a reference region based DCE-MRI protocol could be implemented during CA distribution to obtain perfusion measures for assessing angiogenesis.

A future objective for the novel contrast enhanced T_2 method is translation to human imaging, for the purpose of investigating muscle microstructure in inflammatory myopathies and disease. Successful adaptation of this method, however, is predicated on significantly reducing the length of the pre- and post-contrast T_2 measurements. To help achieve this goal, the T_2-HASTE method that was tested in this work could first be translated to the clinical scanners using readily available single-shot fast spin-echo methods. To acquire a contrast enhanced T_2-HASTE measurement at 3T, the required TR may be reduced to ~10s due to

shorter observed T_1s. The collection of 24 optimally placed, non-linearly spaced TE_{eff} with 4 signal averages would result in an acquisition time of ~16 minutes, to be carried out before and after a ~15 minute waiting period for CA equilibrium. The imaging session, approximately 45 minutes in length, would result in multi-slice multi-echo data capable of producing measures of compartmental volume fractions, T_2s, and, possibly, exchange rates. Overall, future studies based on the work presented here would focus on application of the novel T_2-based measurements to aid in forming a more comprehensive model of muscle injury and disease in both pre-clinical and human imaging.

CHAPTER 8

CONCLUSION

As the MR community continues to stress clinical relevance and translation of pre-clinical research, it is important to take a step back and look at both the accuracy and interpretation of the quantitative measurements being made. Many studies reported in the MR literature deal with T_1 and T_2 relaxation in some form or fashion, both with and without the use of contrast agents. Though these studies may not be exclusively concerned with compartmental measurements, the effect of both contrast agent and tissue water dynamics on the observed NMR parameter estimates can be significant and should be considered when performing data analysis. Part of this consideration may include comparison against a non-MRI estimate. Though validation of quantitative MR measures, specifically in DCE-MRI, has been carried out *ex vivo* via radiotracer techniques, there remains a need for more localized *in vivo* methods of MR parameter evaluation and validation. The development and application of novel quantitative SPECT methods, as reported in this work, help fill this void.

Beyond elucidating some of the confounding factors in obtaining accurate DCE-MRI measures in tumor, this work also contributes new methods and analysis techniques for obtaining intrinsic estimates of tissue parameters included in the two-pool model of relaxation. Estimates of exchange are often only reported, if at all, in *ex vivo* studies and in a handful of *in vivo* studies (including DCE-MRI) requiring more involved acquisition schemes and/or fitting routines. The work presented in this dissertation, however, provides a simple method for making estimates of these intrinsic parameters via a contrast enhanced T_2

protocol without the need for a VIF. Development of a method for fast multi-slice T_2 characterization, T_2-HASTE, provides a possible means for translation of the contrast enhanced T_2 method as well as an alternative strategy for fast T_2 mapping.

As a whole, this dissertation raises awareness of the effects of tissues water dynamics on T_1 and T_2 relaxometry with the development of new techniques aimed at making accurate compartmental NMR measurements, specifically, estimates of tissue volume fractions. A quantitative approach that incorporated novel SPECT imaging protocols was developed to help address the previously described issues via comparison to the MR parameter estimates. This work leaves the door open for further research into new pharmacokinetic models for the purpose of DCE-MRI data analysis, applications for *in vivo* exchange measurements, and quantitative SPECT studies with multi-isotope imaging.

REFERENCES

1. Kim HK, Laor T, Horn PS, Racadio JM, Wong B, Dardzinski BJ. T2 mapping in Duchenne muscular dystrophy: distribution of disease activity and correlation with clinical assessments. Radiology 2010;255(3):899-908.
2. Maillard SM, Jones R, Owens C, Pilkington C, Woo P, Wedderburn LR, Murray KJ. Quantitative assessment of MRI T-2 relaxation time of thigh muscles in juvenile dermatomyositis. Rheumatology 2004;43(5):603-608.
3. Gambarota G, Veltien A, van Laarhoven H, Philippens M, Jonker A, Mook OR, Frederiks WM, Heerschap A. Measurements of T1 and T2 relaxation times of colon cancer metastases in rat liver at 7 T. MAGMA 2004;17(3-6):281-287.
4. Oh J, Cha S, Aiken AH, Han ET, Crane JC, Stainsby JA, Wright GA, Dillon WP, Nelson SJ. Quantitative apparent diffusion coefficients and T2 relaxation times in characterizing contrast enhancing brain tumors and regions of peritumoral edema. J Magn Reson Imaging 2005;21(6):701-708.
5. Does MD, Gore JC. Compartmental study of T(1) and T(2) in rat brain and trigeminal nerve in vivo. Magn Reson Med 2002;47(2):274-283.
6. Gambarota G, Cairns BE, Berde CB, Mulkern RV. Osmotic effects on the T-2 relaxation decay of in vivo muscle. Magnetic Resonance in Medicine 2001;46(3):592-599.
7. MacKay A, Whittall K, Adler J, Li D, Paty D, Graeb D. In vivo visualization of myelin water in brain by magnetic resonance. Magn Reson Med 1994;31(6):673-677.
8. Dortch RD, Yankeelov TE, Yue Z, Quarles CC, Gore JC, Does MD. Evidence of multiexponential T(2) in rat glioblastoma. NMR Biomed 2009;22(6):609-618.
9. Cole WC, Leblanc AD, Jhingran SG. The Origin of Biexponential T2 Relaxation in Muscle Water. Magnetic Resonance in Medicine 1993;29(1):19-24.
10. Fung BM, Puon PS. Nuclear Magnetic-Resonance Transverse Relaxation in Muscle Water. Biophys J 1981;33(1):27-38.
11. Hazlewoo.Cf, Nichols BL, Chamberl.Nf. On State of Water in Skeletal Muscle. Federation Proceedings 1969;28(2):823-&.
12. Hazlewood CF, Chang DC, Nichols BL, Woessner DE. Nuclear magnetic resonance transverse relaxation times of water protons in skeletal muscle. Biophys J 1974;14(8):583-606.
13. Saab G, Thompson RT, Marsh GD. Multicomponent T-2 relaxation of in vivo skeletal muscle. Magnetic Resonance in Medicine 1999;42(1):150-157.
14. Ababneh Z, Beloeil H, Berde CB, Gambarota G, Maier SE, Mulkern RV. Biexponential parameterization of diffusion and T-2 relaxation decay curves in a rat muscle edema model: Decay curve components and water compartments. Magnetic Resonance in Medicine 2005;54(3):524-531.
15. Fan RH, Does MD. Compartmental relaxation and diffusion tensor imaging measurements in vivo in lambda-carrageenan-induced edema in rat skeletal muscle. NMR Biomed 2008;21(6):566-573.
16. Skinner JT, Does MD. Compartmental relaxation measurements in a graded muscle edema model. Proc 17th Mtg ISMRM 2009;Honolulu, HI, USA:Abstract.

17. Landis CS, Li X, Telang FW, Molina PE, Palyka I, Vetek G, Springer CS, Jr. Equilibrium transcytolemmal water-exchange kinetics in skeletal muscle in vivo. Magn Reson Med 1999;42(3):467-478.
18. Dortch RD, Horch RA, Does MD. Development, simulation, and validation of NMR relaxation-based exchange measurements. J Chem Phys 2009;131(16):164502.
19. Mulkern RV, Bleier AR, Adzamli IK, Spencer RGS, Sandor T, Jolesz FA. 2-Site Exchange Revisited - a New Method for Extracting Exchange Parameters in Biological-Systems. Biophys J 1989;55(2):221-232.
20. Sourbron SP, Buckley DL. Tracer kinetic modelling in MRI: estimating perfusion and capillary permeability. Phys Med Biol 2012;57(2):R1-33.
21. Tofts PS. Modeling tracer kinetics in dynamic Gd-DTPA MR imaging. J Magn Reson Imaging 1997;7(1):91-101.
22. Tofts PS, Brix G, Buckley DL, Evelhoch JL, Henderson E, Knopp MV, Larsson HB, Lee TY, Mayr NA, Parker GJ, Port RE, Taylor J, Weisskoff RM. Estimating kinetic parameters from dynamic contrast-enhanced T(1)-weighted MRI of a diffusable tracer: standardized quantities and symbols. J Magn Reson Imaging 1999;10(3):223-232.
23. Yankeelov TE, Rooney WD, Li X, Springer CS, Jr. Variation of the relaxographic "shutter-speed" for transcytolemmal water exchange affects the CR bolus-tracking curve shape. Magn Reson Med 2003;50(6):1151-1169.
24. Pellerin M, Yankeelov TE, Lepage M. Incorporating contrast agent diffusion into the analysis of DCE-MRI data. Magnetic Resonance in Medicine 2007;58(6):1124-1134.
25. van Everdingen KJ, van der Grond J, Kappelle LJ, Ramos LM, Mali WP. Diffusion-weighted magnetic resonance imaging in acute stroke. Stroke 1998;29(9):1783-1790.
26. Kono K, Inoue Y, Nakayama K, Shakudo M, Morino M, Ohata K, Wakasa K, Yamada R. The role of diffusion-weighted imaging in patients with brain tumors. AJNR Am J Neuroradiol 2001;22(6):1081-1088.
27. Haacke EM. Magnetic resonance imaging : physical principles and sequence design. New York: Wiley; 1999. xxvii, 914 p. p.
28. Bloch F. Nuclear Induction. Phys Rev 1946;70:460.
29. Hahn EL. Spin Echoes. Phys Rev 1950;80:580.
30. Carr H, Purcell E. Effects of diffusion on free precession in nuclear magnetic resonance experiments. Phys Rev 1954;94:630-638.
31. Meiboom S, Gill D. Modified spin-echo method for measuring nuclear relaxation times. Rev Sci instrum 1958;29:688-691.
32. Majumdar S, Orphanoudakis SC, Gmitro A, O'Donnell M, Gore JC. Errors in the measurements of T2 using multiple-echo MRI techniques. II. Effects of static field inhomogeneity. Magn Reson Med 1986;3(4):562-574.
33. Crawley AP, Henkelman RM. Errors in T2 estimation using multislice multiple-echo imaging. Magn Reson Med 1987;4(1):34-47.
34. Poon CS, Henkelman RM. Practical T2 quantitation for clinical applications. J Magn Reson Imaging 1992;2(5):541-553.
35. Majumdar S, Orphanoudakis SC, Gmitro A, O'Donnell M, Gore JC. Errors in the measurements of T2 using multiple-echo MRI techniques. I. Effects of radiofrequency pulse imperfections. Magn Reson Med 1986;3(3):397-417.

36. Levitt MH, Freeman R. Compensation for Pulse Imperfections in Nmr Spin-Echo Experiments. Journal of Magnetic Resonance 1981;43(1):65-80.
37. Majumdar S, Gore JC. Effects of selective pulses on the measurement of T2 and apparent diffusion in multiecho MRI. Magn Reson Med 1987;4(2):120-128.
38. Fautz HP, Buchert M, Husstedt H, Laubenberger J, Hennig J. TSE-sequences with spin-echo contrast. Magnetic Resonance in Medicine 2000;43(4):577-582.
39. Pell GS, Briellmann RS, Waites AB, Abbott DF, Lewis DP, Jackson GD. Optimized clinical T2 relaxometry with a standard CPMG sequence. Journal of Magnetic Resonance Imaging 2006;23(2):248-252.
40. Li W, Griswold M, Yu X. Rapid T(1) Mapping of Mouse Myocardium With Saturation Recovery Look-Locker Method. Magnetic Resonance in Medicine 2010;64(5):1296-1303.
41. Mai VM, Knight-Scott J, Berr SS. Improved visualization of the human lung in H-1 MRI using multiple inversion recovery for simultaneous suppression of signal contributions from fat and muscle. Magnetic Resonance in Medicine 1999;41(5):866-870.
42. Wang HZ, Riederer SJ, Lee JN. Optimizing the Precision in T1 Relaxation Estimation Using Limited Flip Angles. Magnetic Resonance in Medicine 1987;5(5):399-416.
43. Cheng HLM, Wright GA. Rapid high-resolution T-1 mapping by variable flip angles: Accurate and precise measurements in the presence of radiofrequency field inhomogeneity. Magnetic Resonance in Medicine 2006;55(3):566-574.
44. Stanisz GJ, Kecojevic A, Bronskill MJ, Henkelman RM. Characterizing white matter with magnetization transfer and T-2. Magnetic Resonance in Medicine 1999;42(6):1128-1136.
45. Zimmerman JR, Brittin WE. Nuclear Magnetic Resonance Studies in Multiple Phase Systems: Lifetime of a Water Molecule in an Adsorbing Phase on Silica Gel. The Journal of Physical Chemistry 1957;61(10):1328-1333.
46. Skinner MG, Kolind SH, MacKay AL. The effect of varying echo spacing within a multiecho acquisition: better characterization of long T-2 components. Magn Reson Imaging 2007;25(6):840-847.
47. Whittall KP, Mackay AL. Quantitative Interpretation of Nmr Relaxation Data. Journal of Magnetic Resonance 1989;84(1):134-152.
48. McConnell HM. Reaction rates by nuclear magnetic resonance. J Chem Phys 1959;28(3):430.
49. Woessner DE. Nuclear trasnfer effects in nuclear magnetic resonance pulse experiments. J Chem Phys 1961;35:41.
50. Andrasko J. Water Diffusion Permeability of Human Erythrocytes Studies by a Pulsed Gradient Nmr Technique. Biochimica Et Biophysica Acta 1976;428(2):304-311.
51. Conlon T, Outhred R. Water Diffusion Permeability of Erythrocytes Using an Nmr Technique. Biochimica Et Biophysica Acta 1972;288(2):354-&.
52. Fabry ME, Eisenstadt M. Water Exchange between Red-Cells and Plasma - Measurement by Nuclear Magnetic-Relaxation. Biophys J 1975;15(11):1101-1110.

53. Herbst MD, Goldstein JH. Cell Water Transport Measurement by Nmr - a 3-Compartment Model Which Includes Cell-Aggregation. Journal of Magnetic Resonance 1984;60(2):299-306.
54. Donahue KM, Burstein D, Manning WJ, Gray ML. Studies of Gd-Dtpa Relaxivity and Proton-Exchange Rates in Tissue. Magnetic Resonance in Medicine 1994;32(1):66-76.
55. Mauss Y, Grucker D, Fornasiero D, Chambron J. Nmr Compartmentalization of Free-Water in the Perfused Rat-Heart. Magnetic Resonance in Medicine 1985;2(3):187-194.
56. Sobol WT, Jackels SC, Cothran RL, Hinson WH. Nmr Spin-Lattice Relaxation in Tissues with High-Concentration of Paramagnetic Contrast-Media - Evaluation of Water Exchange-Rates in Intact Rat Muscle. Med Phys 1991;18(2):243-250.
57. Washburn KE, Callaghan PT. Tracking pore to pore exchange using relaxation exchange spectroscopy. Physical Review Letters 2006;97(17):175502.
58. Monteilhet L, Korb JP, Mitchell J, McDonald PJ. Observation of exchange of micropore water in cement pastes by two-dimensional T(2)-T(2) nuclear magnetic resonance relaxometry. Phys Rev E Stat Nonlin Soft Matter Phys 2006;74(6 Pt 1):061404.
59. Lee JH, Labadie C, Springer CS, Harbison GS. Two-dimensional inverse Laplace transform NMR: altered relaxation times allow detection of exchange correlation. J Am Chem Soc 1993;115(17):7761.
60. Donahue KM, Weisskoff RM, Parmelee DJ, Callahan RJ, Wilkinson RA, Mandeville JB, Rosen BR. Dynamic Gd-Dtpa Enhanced Mri Measurement of Tissue Cell-Volume Fraction. Magnetic Resonance in Medicine 1995;34(3):423-432.
61. Donahue KM, Weisskoff RM, Chesler DA, Kwong KK, Bogdanov AA, Mandeville JB, Rosen BR. Improving MR quantification of regional blood volume with intravascular T-1 contrast agents: Accuracy, precision, and water exchange. Magnetic Resonance in Medicine 1996;36(6):858-867.
62. Egeland TA, Simonsen TG, Gaustad JV, Gulliksrud K, Ellingsen C, Rofstad EK. Dynamic contrast-enhanced magnetic resonance imaging of tumors: preclinical validation of parametric images. Radiat Res 2009;172(3):339-347.
63. Ludemann L, Grieger W, Wurm R, Wust P, Zimmer C. Quantitative measurement of leakage volume and permeability in gliomas, meningiomas and brain metastases with dynamic contrast-enhanced MRI. Magn Reson Imaging 2005;23(8):833-841.
64. Parker DL, Goodrich KC, Alexander AL, Buswell HR, Blatter DD, Tsuruda JS. Optimized visualization of vessels in contrast enhanced intracranial MR angiography. Magnetic Resonance in Medicine 1998;40(6):873-882.
65. Kety SS. The theory and applications of the exchange of inert gas at the lungs and tissues. Pharmacol Rev 1951;3(1):1-41.
66. Andersen C, Taagehoj JF, Muhler A, Rehling M. Approximation of arterial input curve data in MRI estimation of cerebral blood-tumor-barrier leakage: comparison between Gd-DTPA and 99mTc-DTPA input curves. Magn Reson Imaging 1996;14(3):235-241.
67. Port RE, Knopp MV, Brix G. Dynamic contrast-enhanced MRI using Gd-DTPA: Interindividual variability of the arterial input function and consequences for the

assessment of kinetics in tumors. Magnetic Resonance in Medicine 2001;45(6):1030-1038.
68. Sourbron SP, Buckley DL. On the scope and interpretation of the Tofts models for DCE-MRI. Magn Reson Med 2011;66(3):735-745.
69. Cheng HL. Investigation and optimization of parameter accuracy in dynamic contrast-enhanced MRI. J Magn Reson Imaging 2008;28(3):736-743.
70. Henderson E, Rutt BK, Lee TY. Temporal sampling requirements for the tracer kinetics modeling of breast disease. Magn Reson Imaging 1998;16(9):1057-1073.
71. Zaidi H. Quantitative analysis in nuclear medicine imaging. New York: Springer; 2006. xi, 583 p. p.
72. Mannting F, Morganmannting MG. GATED SPECT WITH TECHNETIUM-99M-SESTAMIBI FOR ASSESSMENT OF MYOCARDIAL PERFUSION ABNORMALITIES. Journal of Nuclear Medicine 1993;34(4):601-608.
73. Barber PA, Davis SM, Infeld B, Baird AE, Donnan GA, Jolley D, Lichtenstein M. Spontaneous reperfusion after ischemic stroke is associated with improved outcome. Stroke 1998;29(12):2522-2528.
74. Nakatani T, Hayama T, Uchida J, Nakamura K, Takemoto Y, Sugimura K. Diagnostic localization of extra-adrenal pheochromocytoma: Comparison of I-123-MIBG imaging and I-131-MIBG imaging. Oncology Reports 2002;9(6):1225-1227.
75. Kwok CG, Lull RJ, Yen CK, Lim AD. FEASIBILITY OF MECKEL SCAN AFTER RBC GASTROINTESTINAL-BLEEDING STUDY USING IN-VITRO LABELING TECHNIQUE. Clin Nucl Med 1995;20(11):959-961.
76. El Fakhri G, Moore SC, Maksud P, Aurengo A, Kijewski MF. Absolute activity quantitation in simultaneous 123I/99mTc brain SPECT. J Nucl Med 2001;42(2):300-308.
77. Zhu X, Park MA, Gerbaudo VH, Moore SC. Quantitative simultaneous In-111/Tc-99m planar imaging in a long-bone infection phantom. Phys Med Biol 2007;52(24):7353-7365.
78. Berman DS, Kiat H, Friedman JD, Wang FP, Vantrain K, Matzer L, Maddahi J, Germano G. SEPARATE ACQUISITION REST THALLIUM-201/STRESS TC-99M SESTAMIBI DUAL-ISOTOPE MYOCARDIAL PERFUSION SINGLE-PHOTON EMISSION COMPUTED-TOMOGRAPHY - A CLINICAL VALIDATION-STUDY. Journal of the American College of Cardiology 1993;22(5):1455-1464.
79. El Fakhri G, Habert MO, Maksud P, Kas A, Malek Z, Kijewski MF, Lacomblez L. Quantitative simultaneous Tc-99m-ECD/I-123-FP-CIT SPECT in Parkinson's disease and multiple system atrophy. European Journal of Nuclear Medicine and Molecular Imaging 2006;33(1):87-92.
80. Franc BL, Acton PD, Mari C, Hasegawa BH. Small-animal SPECT and SPECT/CT: important tools for preclinical investigation. J Nucl Med 2008;49(10):1651-1663.
81. Hwang AB, Franc BL, Gullberg GT, Hasegawa BH. Assessment of the sources of error affecting the quantitative accuracy of SPECT imaging in small animals. Phys Med Biol 2008;53(9):2233-2252.
82. Donahue KM, Weisskoff RM, Parmelee DJ, Callahan RJ, Wilkinson RA, Mandeville JB, Rosen BR. Dynamic Gd-DTPA enhanced MRI measurement of tissue cell volume fraction. Magn Reson Med 1995;34(3):423-432.

83. Knight RA, Nagaraja TN, Ewing JR, Nagesh V, Whitton PA, Bershad E, Fagan SC, Fenstermacher JD. Quantitation and localization of blood-to-brain influx by magnetic resonance imaging and quantitative autoradiography in a model of transient focal ischemia. Magn Reson Med 2005;54(4):813-821.
84. Nagaraja TN, Ewing JR, Karki K, Jacobs PE, Divine GW, Fenstermacher JD, Patlak CS, Knight RA. MRI and quantitative autoradiographic studies following bolus injections of unlabeled and (14)C-labeled gadolinium-diethylenetriaminepentaacetic acid in a rat model of stroke yield similar distribution volumes and blood-to-brain influx rate constants. NMR Biomed 2010.
85. Meikle SR, Kench P, Kassiou M, Banati RB. Small animal SPECT and its place in the matrix of molecular imaging technologies. Phys Med Biol 2005;50(22):R45-61.
86. Peters AM, Jamar F. The importance of endothelium and interstitial fluid in nuclear medicine. Eur J Nucl Med 1998;25(7):801-815.
87. Horch RA, Nyman JS, Gochberg DF, Dortch RD, Does MD. Characterization of (1)H NMR Signal in Human Cortical Bone for Magnetic Resonance Imaging. Magnetic Resonance in Medicine 2010;64(3):680-687.
88. de Lussanet QG, van Golde JCG, Beets-Tan RGH, Post MJ, Huijberts MS, Schaper NC, Kessels AGH, van Engelshoven JMA, Backes WH. Dynamic contrast-enhanced MRI of muscle perfusion combined with MR angiography of collateral artery growth in a femoral artery ligation model. NMR Biomed 2007;20(8):717-725.
89. Civan MM, Achlama AM, Shporer M. Relationship between Transverse and Longitudinal Nuclear Magnetic-Resonance Relaxation Rates of Muscle Water. Biophys J 1978;21(2):127-136.
90. Damon BM, Gregory CD, Hall KL, Stark HJ, Gulani V, Dawson MJ. Intracellular acidification and volume increases explain R-2 decreases in exercising muscle. Magnetic Resonance in Medicine 2002;47(1):14-23.
91. Morvan D, LeroyWillig A. Simultaneous measurements of diffusion and transverse relaxation in exercising skeletal muscle. Magn Reson Imaging 1995;13(7):943-948.
92. PloutzSnyder LL, Nyren S, Cooper TG, Potchen EJ, Meyer RA. Different effects of exercise and edema on T-2 relaxation in skeletal muscle. Magnetic Resonance in Medicine 1997;37(5):676-682.
93. Gissel H, Despa F, Collins J, Mustafi D, Rojahn K, Karczmar G, Lee R. Magnetic resonance imaging of changes in muscle tissues after membrane trauma. Cell Injury: Mechanisms, Responses, and Repair 2005;1066:272-285.
94. Stekelenburg A, Oomens CWJ, Strijkers GJ, Nicolay K, Bader DL. Compression-induced deep tissue injury examined with magnetic resonance imaging and histology. Journal of Applied Physiology 2006;100(6):1946-1954.
95. Tang GL, Chang DS, Sarkar R, Wang R, Messina LM. The effect of gradual or acute arterial occlusion on skeletal muscle blood flow, artcriogenesis, and inflammation in rat hindlimb ischemia. Journal of Vascular Surgery 2005;41(2):312-320.
96. Heemskerk AM, Strijkers GJ, Drost MR, van Bochove GS, Nicolay K. Skeletal muscle degeneration and regeneration after femoral artery ligation in mice: Monitoring with diffusion MR imaging. Radiology 2007;243(2):413-421.
97. Luo YP, Mohning KM, Hradil VP, Wessale JL, Segreti JA, Nuss ME, Wegner CD, Burke SE, Cox BF. Evaluation of tissue perfusion in a rat model of hind-limb muscle

ischemia using dynamic contrast-enhanced magnetic resonance imaging. Journal of Magnetic Resonance Imaging 2002;16(3):277-283.
98. Di Rosa M, Giroud JP, Willoughby DA. Studies on the mediators of the acute inflammatory response induced in rats in different sites by carrageenan and turpentine. J Pathol 1971;104(1):15-29.
99. Mense S. Nociception from Skeletal-Muscle in Relation to Clinical Muscle Pain. Pain 1993;54(3):241-289.
100. Guay J, Bateman K, Gordon R, Mancini J, Riendeau D. Carrageenan-induced paw edema in rat elicits a predominant prostaglandin E-2 (PGE(2)) response in the central nervous system associated with the induction of microsomal PGE(2) synthase-1. Journal of Biological Chemistry 2004;279(23):24866-24872.
101. Lazzarini R, Paulino CA, Malucelli BE, PalemoNeto J. Effects of high doses of diazepam on carrageenin-induced paw edema in rats. Brazilian Journal of Medical and Biological Research 1996;29(11):1525-1529.
102. Saab G, Thompson RT, Marsh GD, Picot PA, Moran GR. Two-dimensional time correlation relaxometry of skeletal muscle in vivo at 3 tesla. Magnetic Resonance in Medicine 2001;46(6):1093-1098.
103. Bernstein MA, King KF, Zhou XJ. Handbook of MRI pulse sequences. Amsterdam ; Boston: Academic Press; 2004. Ch 13 p.
104. Patel MR, Klufas RA, Alberico RA, Edelman RR. Half-fourier acquisition single-shot turbo spin-echo (HASTE) MR: comparison with fast spin-echo MR in diseases of the brain. AJNR Am J Neuroradiol 1997;18(9):1635-1640.
105. Harrer JU, Parker GJ, Haroon HA, Buckley DL, Embelton K, Roberts C, Baleriaux D, Jackson A. Comparative study of methods for determining vascular permeability and blood volume in human gliomas. J Magn Reson Imaging 2004;20(5):748-757.
106. Landis CS, Li X, Telang FW, Coderre JA, Micca PL, Rooney WD, Latour LL, Vetek G, Palyka I, Springer CS, Jr. Determination of the MRI contrast agent concentration time course in vivo following bolus injection: effect of equilibrium transcytolemmal water exchange. Magn Reson Med 2000;44(4):563-574.
107. Pickup S, Zhou R, Glickson J. MRI estimation of the arterial input function in mice. Acad Radiol 2003;10(9):963-968.
108. Zhou R, Pickup S, Yankeelov TE, Springer CS, Jr., Glickson JD. Simultaneous measurement of arterial input function and tumor pharmacokinetics in mice by dynamic contrast enhanced imaging: effects of transcytolemmal water exchange. Magn Reson Med 2004;52(2):248-257.
109. Yankeelov TE, Cron GO, Addison CL, Wallace JC, Wilkins RC, Pappas BA, Santyr GE, Gore JC. Comparison of a reference region model with direct measurement of an AIF in the analysis of DCE-MRI data. Magnetic Resonance in Medicine 2007;57(2):353-361.
110. Yankeelov TE, Luci JJ, Lepage M, Li R, Debusk L, Lin PC, Price RR, Gore JC. Quantitative pharmacokinetic analysis of DCE-MRI data without an arterial input function: a reference region model. Magn Reson Imaging 2005;23(4):519-529.
111. Rodriguez E, Roig A, Molins E, Arus C, Quintero MR, Cabanas ME, Cerdan S, Lopez-Larrubia P, Sanfeliu C. In vitro characterization of an Fe(8) cluster as potential MRI contrast agent. NMR Biomed 2005;18(5):300-307.

112. Donahue KM, Burstein D, Manning WJ, Gray ML. Studies of Gd-DTPA relaxivity and proton exchange rates in tissue. Magn Reson Med 1994;32(1):66-76.
113. Dobre MC, Ugurbil K, Marjanska M. Determination of blood longitudinal relaxation time (T1) at high magnetic field strengths. Magn Reson Imaging 2007;25(5):733-735.
114. Karathanasis E, Park J, Agarwal A, Patel V, Zhao F, Annapragada AV, Hu X, Bellamkonda RV. MRI mediated, non-invasive tracking of intratumoral distribution of nanocarriers in rat glioma. Nanotechnology 2008;19(31):315101.
115. Tsekos NV, Zhang F, Merkle H, Nagayama M, Iadecola C, Kim SG. Quantitative measurements of cerebral blood flow in rats using the FAIR technique: correlation with previous iodoantipyrine autoradiographic studies. Magn Reson Med 1998;39(4):564-573.
116. Galons JP, Trouard T, Gmitro AF, Lien YH. Hemodialysis increases apparent diffusion coefficient of brain water in nephrectomized rats measured by isotropic diffusion-weighted magnetic resonance imaging. J Clin Invest 1996;98(3):750-755.
117. Gregory TJ, Wallis CJ, Printz MP. Regional changes in rat brain angiotensinogen following bilateral nephrectomy. Hypertension 1982;4(6):827-838.
118. Nagaraja TN, Karki K, Ewing JR, Divine GW, Fenstermacher JD, Patlak CS, Knight RA. The MRI-Measured Arterial Input Function Resulting From a Bolus Injection of Gd-DTPA in a Rat Model of Stroke Slightly Underestimates That of Gd-[(14)C]DTPA and Marginally Overestimates the Blood-to-Brain Influx Rate Constant Determined by Patlak Plots. Magnetic Resonance in Medicine 2010;63(6):1502-1509.
119. Li X, Rooney WD, Varallyay CG, Gahramanov S, Muldoon LL, Goodman JA, Tagge IJ, Selzer AH, Pike MM, Neuwelt EA, Springer CS. Dynamic-contrast-enhanced-MRI with extravasating contrast reagent: Rat cerebral glioma blood volume determination. Journal of Magnetic Resonance 2010;206(2):190-199.
120. McIntyre DJ, Ludwig C, Pasan A, Griffiths JR. A method for interleaved acquisition of a vascular input function for dynamic contrast-enhanced MRI in experimental rat tumours. NMR Biomed 2004;17(3):132-143.
121. Pickup S, Chawla S, Poptani H. Quantitative estimation of dynamic contrast enhanced MRI parameters in rat brain gliomas using a dual surface coil system. Acad Radiol 2009;16(3):341-350.
122. Garpebring A, Wirestam R, Ostlund N, Karlsson M. Effects of inflow and radiofrequency spoiling on the arterial input function in dynamic contrast-enhanced MRI: a combined phantom and simulation study. Magn Reson Med 2011;65(6):1670-1679.
123. Roberts C, Little R, Watson Y, Zhao S, Buckley DL, Parker GJ. The effect of blood inflow and B(1)-field inhomogeneity on measurement of the arterial input function in axial 3D spoiled gradient echo dynamic contrast-enhanced MRI. Magn Reson Med 2011;65(1):108-119.
124. Kreis D, Schulz D, Stein M, Preuss M, Nestler U. Assessment of parameters influencing the blood flow velocities in cerebral arteries of the rat using ultrasonographic examination. Neurol Res 2011;33(4):389-395.
125. Fan X, Haney CR, Mustafi D, Yang C, Zamora M, Markiewicz EJ, Karczmar GS. Use of a reference tissue and blood vessel to measure the arterial input function in DCEMRI. Magn Reson Med 2010;64(6):1821-1826.

126. Ragan DK, Bankson JA. Suppression of vascular enhancement artifacts through the use of a multiband, selectively spoiled radiofrequency excitation pulse. J Magn Reson Imaging 2011;33(5):1256-1261.
127. Bled E, Hassen WB, Pourtau L, Mellet P, Lanz T, Schuler D, Voisin P, Franconi JM, Thiaudiere E, Miraux S. Real-time 3D MRI of contrast agents in whole living mice. Contrast Media Mol Imaging 2011;6(4):275-281.
128. Vautier J, Heilmann M, Walczak C, Mispelter J, Volk A. 2D and 3D radial multi-gradient-echo DCE MRI in murine tumor models with dynamic R*2-corrected R1 mapping. Magn Reson Med 2010;64(1):313-318.
129. Wilmes LJ, Pallavicini MG, Fleming LM, Gibbs J, Wang D, Li KL, Partridge SC, Henry RG, Shalinsky DR, Hu-Lowe D, Park JW, McShane TM, Lu Y, Brasch RC, Hylton NM. AG-013736, a novel inhibitor of VEGF receptor tyrosine kinases, inhibits breast cancer growth and decreases vascular permeability as detected by dynamic contrast-enhanced magnetic resonance imaging. Magn Reson Imaging 2007;25(3):319-327.
130. Heisen M, Fan X, Buurman J, van Riel NA, Karczmar GS, ter Haar Romeny BM. The influence of temporal resolution in determining pharmacokinetic parameters from DCE-MRI data. Magn Reson Med 2010;63(3):811-816.
131. Barnes SL, Gore JC, Yankeelov TE. Modeling the effect of diffusion on the assessment of Ktrans and ve in DCE-MRI. Proc 19th Mtg ISMRM 2011;Montreal, QU, CA:Abstract.
132. Mills SJ, Soh C, Rose CJ, Cheung S, Zhao S, Parker GJM, Jackson A. Candidate Biomarkers of Extravascular Extracellular Space: A Direct Comparison of Apparent Diffusion Coefficient and Dynamic Contrast-Enhanced MR Imaging-Derived Measurement of the Volume of the Extravascular Extracellular Space in Glioblastoma Multiforme. American Journal of Neuroradiology 2010;31(3):549-553.
133. Arlinghaus LR, Li X, Rahman AR, Welch EB, Xu L, Gore JC, Yankeelov TE. On the relationship between the apparent diffusion coefficient and extravascular extracellular volume fraction in human breast cancer. Magn Reson Imaging 2011;29(5):630-638.
134. Loveless ME, Lawson D, Collins M, Reimer C, Huszar D, Halliday J, Waterton JC, Gore JC, Yankeelov TE. Correlation of quantitative tissue characterisitics from DCE-MRI, DW-MRI, and histology in murine tumors. Proc 19th Mtg ISMRM 2011;Montreal, QU, CA:Abstract.
135. Wedam SB, Low JA, Yang SX, Chow CK, Choyke P, Danforth D, Hewitt SM, Berman A, Steinberg SM, Liewehr DJ, Plehn J, Doshi A, Thomasson D, McCarthy N, Koeppen H, Sherman M, Zujewski J, Camphausen K, Chen H, Swain SM. Antiangiogenic and antitumor effects of bevacizumab in patients with inflammatory and locally advanced breast cancer. Journal of Clinical Oncology 2006;24(5):769-777.
136. Yankeelov TE, Lepage M, Chakravarthy A, Broome EE, Niermann KJ, Kelley MC, Meszoely I, Mayer IA, Herman CR, McManus K, Price RR, Gore JC. Integration of quantitative DCE-MRI and ADC mapping to monitor treatment response in human breast cancer: initial results. Magn Reson Imaging 2007;25(1):1-13.
137. Li X, Welch EB, Chakravarthy AB, Xu L, Arlinghaus LR, Farley J, Mayer IA, Kelley MC, Meszoely IM, Means-Powell J, Abramson VG, Grau AM, Gore JC, Yankeelov

TE. Statistical comparison of dynamic contrast-enhanced MRI pharmacokinetic models in human breast cancer. Magn Reson Med 2011.
138. Yankeelov TE, Rooney WD, Huang W, Dyke JP, Li X, Tudorica A, Lee JH, Koutcher JA, Springer CS, Jr. Evidence for shutter-speed variation in CR bolus-tracking studies of human pathology. NMR Biomed 2005;18(3):173-185.
139. Buckley DL, Kershaw LE, Stanisz GJ. Cellular-interstitial water exchange and its effect on the determination of contrast agent concentration in vivo: dynamic contrast-enhanced MRI of human internal obturator muscle. Magn Reson Med 2008;60(5):1011-1019.
140. Straub V, Donahue KM, Allamand V, Davisson RL, Kim YR, Campbell KP. Contrast agent-enhanced magnetic resonance imaging of skeletal muscle damage in animal models of muscular dystrophy. Magn Reson Med 2000;44(4):655-659.
141. Maier CF, Tan SG, Hariharan H, Potter HG. T2 quantitation of articular cartilage at 1.5 T. J Magn Reson Imaging 2003;17(3):358-364.
142. Foltz WD, Al-Kwifi O, Sussman MS, Stainsby JA, Wright GA. Optimized spiral imaging for measurement of myocardial T2 relaxation. Magn Reson Med 2003;49(6):1089-1097.
143. Oh J, Han ET, Pelletier D, Nelson SJ. Measurement of in vivo multi-component T2 relaxation times for brain tissue using multi-slice T2 prep at 1.5 and 3 T. Magn Reson Imaging 2006;24(1):33-43.
144. Lebel RM, Wilman AH. Transverse relaxometry with stimulated echo compensation. Magn Reson Med 2010;64(4):1005-1014.
145. Prasloski T, Mädler B, Xiang Q-S, MacKay A, Jones C. Applications of stimulated echo correction to multicomponent T2 analysis. Magnetic Resonance in Medicine 2011:n/a-n/a.
146. Dula AN, Gochberg DF, Does MD. Optimal echo spacing for multi-echo imaging measurements of Bi-exponential T(2) relaxation. Journal of Magnetic Resonance 2009;196(2):149-156.
147. de Bazelaire CM, Duhamel GD, Rofsky NM, Alsop DC. MR imaging relaxation times of abdominal and pelvic tissues measured in vivo at 3.0 T: preliminary results. Radiology 2004;230(3):652-659.
148. Zhang L, Kholmovski EG, Guo J, Choi SE, Morrell GR, Parker DL. HASTE sequence with parallel acquisition and T2 decay compensation: application to carotid artery imaging. Magn Reson Imaging 2009;27(1):13-22.
149. Zhou X, Liang ZP, Cofer GP, Beaulieu CF, Suddarth SA, Johnson GA. Reduction of ringing and blurring artifacts in fast spin-echo imaging. J Magn Reson Imaging 1993;3(5):803-807.
150. Gold GE, Han E, Stainsby J, Wright G, Brittain J, Beaulieu C. Musculoskeletal MRI at 3.0T: Relaxation times and image contrast. American Journal of Roentgenology 2004;183(2):343-351.
151. Feng L, Otazo R, Jung H, Jensen JH, Ye JC, Sodickson DK, Kim D. Accelerated cardiac T2 mapping using breath-hold multiecho fast spin-echo pulse sequence with k-t FOCUSS. Magn Reson Med 2011;65(6):1661-1669.
152. Kim D, Jensen JH, Wu EX, Sheth SS, Brittenham GM. Breathhold multiecho fast spin-echo pulse sequence for accurate R2 measurement in the heart and liver. Magn Reson Med 2009;62(2):300-306.

153. Senegas J, Liu W, Dahnke H, Song H, Jordan EK, Frank JA. Fast T(2) relaxometry with an accelerated multi-echo spin-echo sequence. NMR Biomed 2010;23(8):958-967.
154. Liu W, Turkbey B, Senegas J, Remmele S, Xu S, Kruecker J, Bernardo M, Wood BJ, Pinto PA, Choyke PL. Accelerated T2 mapping for characterization of prostate cancer. Magn Reson Med 2011;65(5):1400-1406.
155. Sumpf TJ, Uecker M, Boretius S, Frahm J. Model-Based Nonlinear Inverse Reconstruction for T2 Mapping Using Highly Undersampled Spin-Echo MRI. Journal of Magnetic Resonance Imaging 2011;34(2):420-428.
156. Bieri O, Scheffler K, Welsch GH, Trattnig S, Mamisch TC, Ganter C. Quantitative mapping of T2 using partial spoiling. Magn Reson Med 2011;66(2):410-418.
157. Deoni SCL, Rutt BK, Peters TM. Rapid combined T-1 and T-2 mapping using gradient recalled acquisition in the steady state. Magnetic Resonance in Medicine 2003;49(3):515-526.
158. Shrager RI, Weiss GH, Spencer RG. Optimal time spacings for T2 measurements: monoexponential and biexponential systems. NMR Biomed 1998;11(6):297-305.
159. Does MD, Gore JC. Complications of nonlinear echo time spacing for measurement of T (2). NMR Biomed 2000;13(1):1-7.
160. Hennig J. Multiecho Imaging Sequences with Low Refocusing Flip Angles. Journal of Magnetic Resonance 1988;78(3):397-407.
161. Lovitt S, Moore SL, Marden FA. The use of MRI in the evaluation of myopathy. Clinical Neurophysiology 2006;117(3):486-495.
162. Peterson TE, Furenlid LR. SPECT detectors: the Anger Camera and beyond. Phys Med Biol 2011;56(17):R145-182.
163. Johnson LC, Campbell DL, Hull EL, Peterson TE. Characterization of a high-purity germanium detector for small-animal SPECT. Phys Med Biol 2011;56(18):5877-5888.
164. Jensen LR, Garzon B, Heldahl MG, Bathen TF, Lundgren S, Gribbestad IS. Diffusion-weighted and dynamic contrast-enhanced MRI in evaluation of early treatment effects during neoadjuvant chemotherapy in breast cancer patients. J Magn Reson Imaging 2011;34(5):1099-1109.
165. Alic L, van Vliet M, van Dijke CF, Eggermont AM, Veenland JF, Niessen WJ. Heterogeneity in DCE-MRI parametric maps: a biomarker for treatment response? Phys Med Biol 2011;56(6):1601-1616.
166. de Lussanet QG, van Golde JC, Beets-Tan RG, Post MJ, Huijberts MS, Schaper NC, Kessels AG, van Engelshoven JM, Backes WH. Dynamic contrast-enhanced MRI of muscle perfusion combined with MR angiography of collateral artery growth in a femoral artery ligation model. NMR Biomed 2007;20(8):717-725.
167. Loerakker S, Oomens CW, Manders E, Schakel T, Bader DL, Baaijens FP, Nicolay K, Strijkers GJ. Ischemia-reperfusion injury in rat skeletal muscle assessed with T2-weighted and dynamic contrast-enhanced MRI. Magn Reson Med 2011;66(2):528-537.